University of Southampton

Faculty of Engineering and Physical Sciences

Zepler Institute for Photonics and Nanoelectronics

Hollow core fibre based Fabry-Perot interferometers with high finesse

DOI [enter DOI] hyperlink, optional}

by

Meng Ding

ORCID ID: 0000-0003-3654-8660

Thesis for the degree of Doctor of Philosophy

March, 2022

University of Southampton

Abstract

Faculty of Physical Sciences and Engineering

Zepler Institute for Photonics and Nanoelectronics

Doctor of Philosophy

Hollow core fibre based Fabry-Perot interferometers with high finesse

by

Meng Ding

A typical Fabry-Perot interferometer (FP) is formed by enclosing an optical path with two highly reflective mirrors, forcing light to travel many times in between these two mirrors. This gives rise to many resonant peaks in the transmission spectrum, making the FP element useful in many applications such as sensing and stabilised lasers. In many of these applications, the performance improves when the transmission peaks spectral width is reduced. To achieve this, FP needs to have long optical length or highly-reflective mirrors.

Currently, there are two main FPs implementations. The first one is based on free-space light propagation in which the distance between the mirrors (and thus the FP optical lengths) are usually limited to less than 50 cm. To achieve narrow transmission spectral peak width, this requires extremely high mirrors reflectivity and associated finesse (>10^5), which makes such FPs highly sensitive to alignment. An alternative FP implementation uses single-mode optical fibre (SMF-FPs). SMF-FPs can have long lengths (e.g., 100's of meters) and can be very compact and lightweight. Although the finesse of SMF-FPs does not reach that achievable in free-space FPs (due to the fibre transmission loss), their long length enables achieving narrow transmission peaks with similar to that achieved in the high-finesse free-space FPs. Unfortunately, SMF-FPs have several drawbacks that make free-space FPs the preferred approach for many applications, despite free-space FPs larger size and the alignment challenges. The two primary drawbacks are the large sensitivity to temperature variations and unwanted nonlinear effects like stimulated Brillion scattering. The nonlinear effect can be relatively prominent in FPs, where the intra-cavity power is strongly enhanced by the resonant effect. Both of these parasitic effects are mainly due to the interaction of light with the silica glass material in SMFs. For example, the thermal sensitivity of optical length is dominated (95%) by thermally-induced changes in the refractive index of silica glass (thermo-optic effect) with the thermally-induced fibre length (thermal expansion effect) change providing the other 5%.

As light in hollow core fibres (HCFs) travels in air, the unwanted light-glass interaction observed in SMFs is strongly supressed, making HCFs ideal medium for FPs. However, up to date, high finesse HCF based FPs (HCF-FPs) were studied in the literature only with very short HCFs lengths (several cm), limiting their use for many applications. Besides this, all reports have dealt with open (un-sealed) HCFs with no discussion on their long-term applications, which is expected to be limited due to HCF degradation when opened to atmosphere. Finally, the performance limitation of HCF-FPs, e.g., what is the maximum achievable finesse, have not been studied yet.

In this Thesis, I focus on long length and high finesse HCF-FPs and their applications. Firstly, we developed a new method based on an incoherent source and RF spectrum analysis to characterise long-length FPs. The method characterises the beating signal of the incoherent optical comb obtained by transmitting incoherent light through the tested FP. It enabled us to monitor finesse and free spectral range during alignment of HCF-FPs, including measurement of long-length FPs. Secondly, we built HCF-FPs with free-space coupling. We characterized several HCF-FPs of different length to explore experimentally finesse limits. The results showed that the coupling loss between the forward and backward propagating light in HCFs reflected off the mirror can be as low as 0.0028 dB. In turn this enables a finesse of up to 5 000. Experimentally, we I achieved a finesse in excess of 2 500 (limited by the available mirrors), which is a value 20 times larger than reported before for HCF-FP. Thirdly, we fabricated two all-fibred HCF-FPs in collaboration with our colleagues in the Czech Technical University in Prague. The two components had length of 5 m and 23 m, respectively, and finesse in excess of 120 over the entire C band. This represented the first demonstration of all-fibred long (>1 m) HCF-FPs with such a high finesse. We have tested the 23 m HCF-FP almost 3 years later after it was fabricated, with no observable degradation in its performance. This shows the first HCF-FP that can be used in long term applications. Subsequently, we demonstrated two applications based on the fabricated HCF-FPs. The first one uses the HCF-FP to characterise HCF attenuation. The other uses the all-fibred HCF-FP for microwave photonics filtering. Finally, we further improve already-low HCF's thermal stability by proposing and demonstrating a new method. It is based on coiling the HCF on a temperature insensitive spool. In our proof-of-principle demonstration, we achieved HCF thermal sensitivity reduction 3 times, achieving thermal sensitivity as low as 0.13 ppm/^{o}C. This up to date demonstrates the most thermally stable fibre FP at room temperature.

Table of Contents

Table of Tables

Table of Figures

Research Thesis: Declaration of Authorship

Print name:

Title of thesis:

I declare that this thesis and the work presented in it are my own and has been generated by me as the result of my own original research.

I confirm that:

1. This work was done wholly or mainly while in candidature for a research degree at this University;
2. Where any part of this thesis has previously been submitted for a degree or any other qualification at this University or any other institution, this has been clearly stated;
3. Where I have consulted the published work of others, this is always clearly attributed;
4. Where I have quoted from the work of others, the source is always given. With the exception of such quotations, this thesis is entirely my own work;
5. I have acknowledged all main sources of help;
6. Where the thesis is based on work done by myself jointly with others, I have made clear exactly what was done by others and what I have contributed myself;
7. Parts of this work have been published as: [see List of Publications]

Signature: .... Date: ....

Acknowledgements

I am immensely grateful to my main supervisor, Prof. Radan Slavík who taught me and guided me along every step of the way. His knowledge, patience and insight have been a valuable source of inspiration. I have learned a lot, not only on research but also the attitude to the life from him. He has changed me a lot and I could not have thought of a better mentor than Radan.

I am also profoundly indebted to Prof. David Richardson for the overall supervision and guidance he gave and for the valuable feedback provided whenever needed. He was a great strength to me during the time of the PhD.

I would like to thank all my friends at the Optoelectronics Research Centre for all the good times that we had.

I thank all the members of the Optoelectronics Research Centre including academic, research, technical and administrative staff who helped me in numerous ways.

I wish to thank my parents for always supporting me and believing in me.

At last, I would like to give my deepest gratitude to my grandparents, especially my grandmother, who raised me, taught me how to behave and gave me the deepest and selfless love.

Definitions and Abbreviations

AC..Angle-cleaved

AR..Anti-reflection

ARF......................................Antiresonant fibres

ASE......................................Amplified spontaneous emission

BL...Bending loss

BUF......................................Built-up factor

CL...Confinement loss

CRDS....................................Cavity ringdown spectroscopy

CTE......................................Coefficient of thermal expansion

CTF.......................................Conjoined-tube hollow core fibre

DNANF.................................Double-nested antiresonant nodeless fibre

DGD.....................................Differential group delay

EDFA....................................Erbium-doped fibre amplifier

ETL.......................................Equivalent travelling length

F...Finesse

FFP.......................................Fibre Fabry-Perot interferometer

FI..Fibre laser

FP...Fabry-Perot interferometer

FSR.......................................Free spectral range

FWHM.................................Full width at half maximum

FOG.....................................Fibre optic gyroscope

GRIN....................................Graded index fibre

HCF......................................Hollow core fibre

HCF-FP.................................Hollow core fibre based Fabry-Perot interferometer

HOFGLAS.............................Hollow-core optical fibre gas laser

HOM....................................Higher order mode

IL .... Insertion loss

IR.. Infrared region

LIGO .... Laser Interferometer Gravitational-Wave Observatory

LMA.................................... Large mode area

MA .... Mode adapter

MAL.................................... Material absorption loss

MFD .... Mode field diameter

MMF .... Multi-mode fibre

MPF.................................... Microwave photonics filter

MPI..................................... Multi-path interference

MZM .... Mach-Zehnder modulator

NANF................................... Nested antiresonant nodeless hollow-core fibre

NTS...................................... Normalised temperature sensitivity

OEO.................................... Optoelectronics oscillator

OPM................................... Optical power meter

OSA .... Optical spectrum analyser

PBG .... Photonic bandgap

PBGF................................... Photonic bandgap fibre

PBS .... Polarisation beam splitter

PC .... Polarization controller

PD....................................... Photodetector

PI .... Proportional-integral controller

PMF.................................... Polarisation maintaining fibre

PPER................................... Polarisation extinction ratio

PSOF................................... Phase stable optical fibre

PTS .... Photothermal spectroscopy

PZS .... Piezo-stretcher

RBW .... Radio bandwidth

RIA .... Radiation induced attenuation

RL... Return loss

SBS....................................... Stimulated Brillouin scattering

SEM .... Scanning electron microscope

SMF .... Single mode fibre

SSL .... Surface scattering loss

SMF-FP .... Single mode fibre based Fabry-Perot interferometer

SRS....................................... Stimulated Raman scattering

TBPF .... Tunable bandpass photonics optical

TCD .... Thermal coefficient of delay

TDLAS .... Tunable diode laser absorption spectroscopy

TEC .... Thermally-expanded core

TS.. Temperature sensitivity

WMS.................................... Wavelength modulation spectroscopy

VBW .... Video bandwidth

VNA .... Vector network analyser

Chapter 1 Introduction

1.1 Motivation

In the last years of the 19th century, two young French physicists, Alfred Perot and Charles Fabry, [1], proposed a new structure of an interferometer, which is named by their names, Fabry-Perot interferometers (FPs). A typical FP is formed by enclosing an optical path with two highly reflective mirrors, so light can travel between the two mirrors forth and back many times. This gives the interferometer many unique properties such as high wavelength selectivity, high extinction ratio, and the ability to enhance light intensity inside the resonant cavity, making it a widely-used device in many applications such as lasers [2], metrology [3–5] and sensing [6,7].

A typical transmission spectrum of an FP is shown in Figure 1.1. There are several parameters to characterize an FP, which I will discuss in more details in the chapter 3. The first one is peak width, which is the full width at half maximum (FWHM) of the transmission peaks. The second one is the free spectral range (FSR), which is the spacing between neighbouring transmission peaks and which is inversely proportional to n_gL of an FP, where n_g is the group index of the light travelling in the FP and L is the length. The finesse (F) is then defined as the ratio of FSR and peak width.

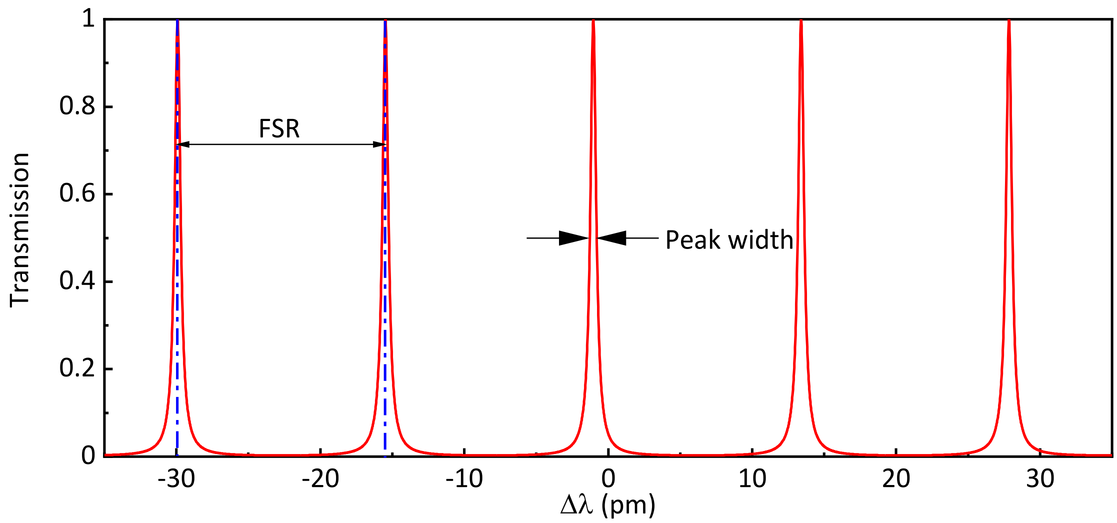

Figure 1.1 Typical transmission spectrum of an Fabry-Perot interferometer.

Many applications would benefit from high finesse or finesse-length product as this leads to a narrow peak. For example, in cavity ring-down spectroscopy, the sensitivity is proportional to the finesse[8]. In cavity-enhanced photothermal FP gas cell sensors, high finesse improves the photothermal phase modulation as well as the sensitivity of phase detection [9,10]. When FPs are used as filters, the extinction ratio improves with finesse [11]. When used as a frequency reference for laser locking [4] or a frequency discrimination element for strain sensing [6], the frequency discrimination capacity improves with finesse-length product.

There are mainly two kinds of FPs now, i.e., free-space and single mode fibre (SMF) based FPs. In free-space FPs (made, e.g., by drilling a hole in a low-expansion glass rod and then attaching high reflectivity mirrors at both ends [4]), L is usually limited by practical constraints to less than 50 cm, limiting the achievable FSR. Thus, if a narrow peak width is desired, ultra-high finesse (sometimes $>10^5$) is needed, making such FPs highly sensitive to alignment. Thus, an alternative implementation using single-mode fibre FPs (SMF-FPs) has been widely investigated. SMF-FPs can have long lengths (e.g., 100's of meters) and can be very compact and lightweight. Although the finesse of SMF-FPs [7,12] does not reach that achievable in free-space FPs (due to the fibre transmission loss), their small FSR enables narrow transmission peaks similar to those of short, high-finesse free-space FPs. Compared to their free-space counterparts, SMF-FPs are often small, light, and easy to operation. Unfortunately, SMF-FPs have several drawbacks that make free-space FPs the preferred approach for many applications, despite free-space FPs larger size and the alignment challenges. The two primary drawbacks are the large sensitivity to temperature variations [7] and unwanted nonlinear effects like stimulated Brillion scattering (SBS) [13], especially in high finesse FPs where the intra-cavity power is strongly enhanced by the resonant effect. Both of these parasitic effects are mainly due to the interaction of light with the silica glass material in SMFs. For example, the thermal sensitivity of the FSR (determined by the temperature dependence of n_gL of the SMF) is dominated (95%) by thermally-induced changes in the refractive index of silica glass (thermo-optic effect) with the thermally-induced fibre length (thermal expansion effect) change providing the other 5% [10].

Hollow core fibres (HCFs), as an air (or vacuum) guided fibre, seems to be a perfect alternative to the SMF. As in an HCF, the glass-light interaction is very weak, all shortcomings of SMFs discussed above should be addressed. Firstly, the thermo-optic effect is practically eliminated, making HCF 20 times less thermally sensitive than SMF of equal L [14]. When considering equal optical length nL, this advantage is reduced (as $n\sim1$ in HCF compared to $n\sim1.45$ in SMF) to about 14 times [15]. Nonlinearities are also substantially weaker in HCF as compared to SMF, enabling several orders of magnitude higher powers to be launched into HCF-FPs as compared to SMF-FPs [1]. And the hollow core of HCFs can also serve as a gas cell, together with the resonant effect inside the FP, making HCF-FP a good platform for gas photonics, e.g., gas nonlinearity study [16] or gas sensing [9,10]. Finally, standard SMF loss and dispersion outside of the communication wavelength band can also pose limitations. Recent improvements in the fabrication of HCFs [17–21] have resulted in losses as low as 0.174 dB/km in the C-band [21]. At both shorter and longer wavelengths, the latest generation of HCFs outperform solid glass fibres in terms of loss whilst having chromatic dispersion of only a few ps/nm/km over several hundred nm's of optical bandwidth[20,22]. Most of these results were achieved with the Nested Antiresonant Nodeless Fibre (NANF) geometry [23]. Such low-loss values would enable high finesse HCF-FPs for multitude of applications at any wavelength of choice within

Several recent works have reported high-finesse HCF-FPs. The cavity mirrors were formed using photonic crystal slabs [24] or high-reflectivity dielectric coatings[9,10]. However, all these reports dealt with cm-long fibre lengths limiting their use for applications requiring narrow transmission peaks. Generally, they used 7-cell photonic bandgap HCF designs, which offer good coupling into SMF, but whose high loss (>10 dB/km) does not allow the construction of high-finesse long-length HCF-FPs (e.g., for 20-m long FP made with 10-dB/km fibre, the fibre-loss-limited maximum achievable finesse is 68 as we show later). Furthermore, the reported HCF-FPs were not designed for long-term operation since their ends were not sealed, enabling air-born pollution like water vapor and dust to enter the hollow core, possibly causing long-term HCF-FP performance degradation[25].

1.2 Aims and novelty

The main goal of the presented research is the development of long-length and high-finesse thermally stable fibre FPs made of HCFs. To achieve this goal, my contributions include,

- A technique based on RF spectrum analyser to characterise a FP when building it and after making it, which is described in 0.
- We explore finesse limits in HCF-FPs both theoretically and experimentally, which is described in 0.
- The technique to build all fibred HCF-FPs used in long-term applications, as described in Chapter 6.
- We demonstrate the developed HCF-FPs in two applications. The first one uses the developed HCF-FP to characterise HCF's loss. The second one uses it to make microwave photonics filter, exploring HCF's application in microwave photonics. These are described in Chapter 7.
- To improve HCF-FP's thermal stability further, we also develop a technique to reduce HCF's thermal sensitivity, described in Chapter 8.

1.3 Thesis structure

In order to clearly separate the work that I did from the state-of-the-art, all the chapters that discuss background and related literatures are at the beginning of the thesis, before presenting the experimental works and results. The background knowledges of Fabry-Perot interferometers and hollow core fibres are presented in chapters 2 and 3, respectively. The theoretical description and experimental demonstration of the technique to characterise FPs when building them and after making them are in chapter 4. The theoretical and experimental work done on finesse limitation exploration of HCF-FPs is presented in chapter 5. All-fibred HCF-FPs and their characterisation is shown in chapter 6. In chapter 7, I present two applications based on HCF-FP techniques. The developed technique to improve HCFs' thermal stability further is described in chapter 8.

- **Chapter 2-Background: Introduction of Fabry-Perot interferometers** Background knowledge of Fabry-Perot interferometers is introduced in this chapter. I first discuss the principle of FPs and then introduce some important parameters, e.g., free spectral range, finesse, insertion loss, extinction ratio, build-up factor, Q factor, and thermal sensitivity. Various structures of FPs are compared, highlighting the HCF-FP's advantages. In the last section, we then introduce some typical applications of FPs.
- **Chapter 3-Background: Introduction of hollow core fibres** A brief background review on history and type of HCFs is provided with the focus on hollow core antiresonant fibres (ARFs) due to their broadband transmission window and low loss. The properties of HCF, especially ARFs, are then introduced. All of these unique properties, i.e., low transmission loss, high higher order modes extinction ratio, low chromatics dispersion, low thermal sensitivity and weak nonlinear effects, make HCFs an ideal transmission media used in high-finesse FPs. As interconnection of single mode fibre and HCF is the key technique to make high-finesse HCF-FPs, I then discuss different interconnection techniques to splice SMF and HCF. In a brief overview, the recent works on HCFs have been provided shows the advantages and prospects of HCFs.
- **Chapter 4-Characterisation of long-length Fabry-Perot interferometers** The method used to characterise our hollow core fibre based Fabry-Perot interferometers is presented in details.
- **0-Finesse limits in HCF-FP** I present in this chapter our work to explore performance limitation of HCF-FP. I analyse in theory how HCF-mirror distance, mirror tilt, fibre cleave angle and fibre loss influence on the finesse. I then built Fabry-Perot interferometers in which hollow core fibre and mirrors can be aligned actively with different lengths. By combining the theory and experiment, we conclude that a finesse over 5000 can be achievable with HCF-FP.
- **Chapter 6-All fibred hollow core fibre based Fabry-Perot interferometers** Two fabricated all-fibred hollow core fibre based Fabry-Perot interferometers are presented in this chapter. They have a length of 5 m and 23 m, respectively. The finesse is measured over 120 over the C-band. The thermal sensitivity of the HCF-FP was measured together with a single mode fibre based Fabry-Perot interferometer (SMF-FP), showing that the HCF-FP has about 15 times better

thermal stability than that of SMF-FP. Additionally, the hermeticity is tested almost 3 years later after the Fabry-Perot interferometers were made. To the best of our knowledge, this is the first high-finesse hollow core fibre based Fabry-Perot interferometers that can be used in long-term applications.

- **Chapter 7-Applications of Fabry-Perot interferometers** Two applications based on hollow core fibre based Fabry-Perot technology are presented here. The first one is to use HCF-FP to measure hollow core fibre loss. Due to the repeatable high finesse I achieved, I could measure hollow core fibre loss with a very good accuracy. The second one is to make a microwave photonics filter (MPF) based on the all-fibred HCF-FP. Due to the low thermal sensitivity of hollow core fibre, the HCF-FP based MPF has less requirement of temperature control than that of SMF based MPF.
- **Chapter 8-Further improvement of Hollow core fibre based Fabry-Perot thermal stability** The method of reducing the thermal sensitivity of HCF-FP by coiling the hollow core fibre to a temperature insensitive spool in presented here. I achieved the lowest thermal sensitivity of any fibre based Fabry-Perot interferometers at room temperature.
- **Chapter 9-Conclusions and future works** The main findings of the work presented in the thesis is discussed and avenues for future investigations are suggested.

Chapter 2 Background: Introduction of Fabry-Perot Interferometers

In this chapter, the basic principle and important parameters of Fabry-Perot interferometer are introduced. Various types of Fabry-Perot interferometers are compared to show advantages of hollow core fibre based Fabry-Perot interferometers. In the last part of this chapter, applications of Fabry-Perot interferometers are discussed.

2.1 Principle of Fabry-Perot interferometers

The basic structure of an FP with a length L is shown in Figure 2.1. Due to the two reflectors, light can travel forth and back many times before it leaves the interferometer. The output of an FP is given by the multi-interference of the light circulating in the resonator.

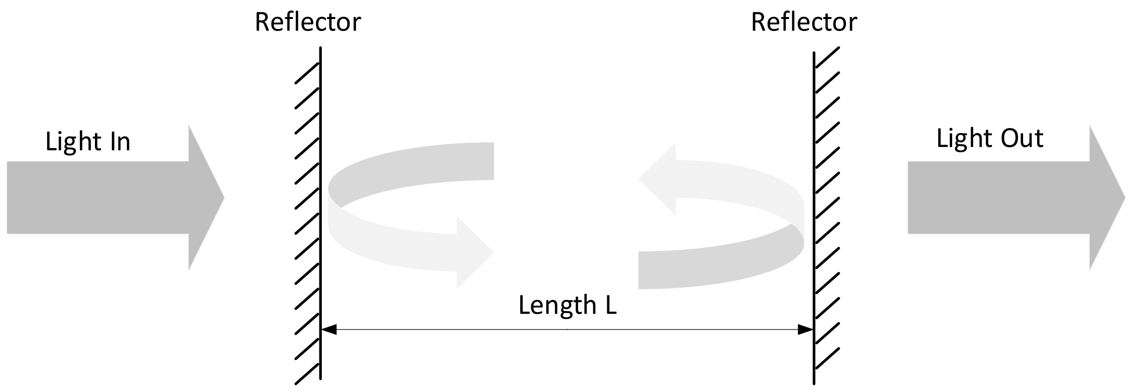

Figure 2.1 Basic structure for analysing the Fabry-Perot interferometer.

2.1.1 Multi-beam interference in a lossy media

Let us consider an FP where both the reflectors and transmission media are lossy, shown in Figure 2.2. Considering complex amplitude of the incident wave as A_0, the partial outputs A_i after ith round-trip inside the cavity can be written as

$$A_1 = t^2 A_0 e^{-i\delta/2} e^{-\alpha_l L/2}, A_2 = t^2 r^2 A_0 e^{-i\delta} e^{-\alpha_l L} e^{-i\delta/2} e^{-\alpha_l L/2}, A_3 = t^2 r^4 A_0 e^{-i2\delta} e^{-2\alpha_l L} e^{-i\delta/2} e^{-\alpha_l L/2}, \ldots \quad (2.1)$$

Here, the subscript of A_i (i=1,2,3,$\cdots$) means that the light is reflected in the cavity by 2*(i-1) times. α_l is the transmission media's loss, i.e., in a fibre FP (FFP), it corresponds to the fibre transmission loss. $\delta = 4\pi nL/\lambda$ is the round-trip phase change inside the FP. Here, the phase shift of reflection at reflectors are neglected as a reflector produce a π phase shift at normal incidence and in total the two reflectors produce 2π phase shift which will not influence the resonant condition much. n indicates the refractive index of the transmission media (while in an FFP it is the effective index) and L is the cavity length of the FP. r and t denote the coefficients of reflectivity and transmission, respectively of the reflector. Here, I suppose that the two reflectors are identical. When considering reflector absorption loss α_m, there should be

$$r^2 + t^2 = 1 - \alpha_m . \tag{2.2}$$

We further define reflectivity and transmission as

$$R = r^2 \quad and \quad T = t^2 , \tag{2.3}$$

which characterize reflected and transmitted optical power. The total transmitted complex amplitude is obtained via coherent summation of all the partial outputs A_i and can be written as

$$A_t = \frac{Te^{-i\delta/2}e^{-\alpha_l L/2}}{1 - Re^{-i\delta}e^{-\alpha_l L}} A_0 . \tag{2.4}$$

The transmitted optical power is then $A_t \times A_t^*$, so we get the transmission of an FP as

$$T_{FP} = \frac{T^2 G}{(1-RG)^2 + 4RG\sin^2\left(\delta/2\right)} . \tag{2.5}$$

$G = e^{-\alpha_l L}$ is the light power loss in the cavity in a single pass. Based on this equation, a lossy FP's transmission characteristic with various mirror reflectivities was calculated, as shown in Figure 2.3.

Figure 2.2 multi-beam interference in lossy media

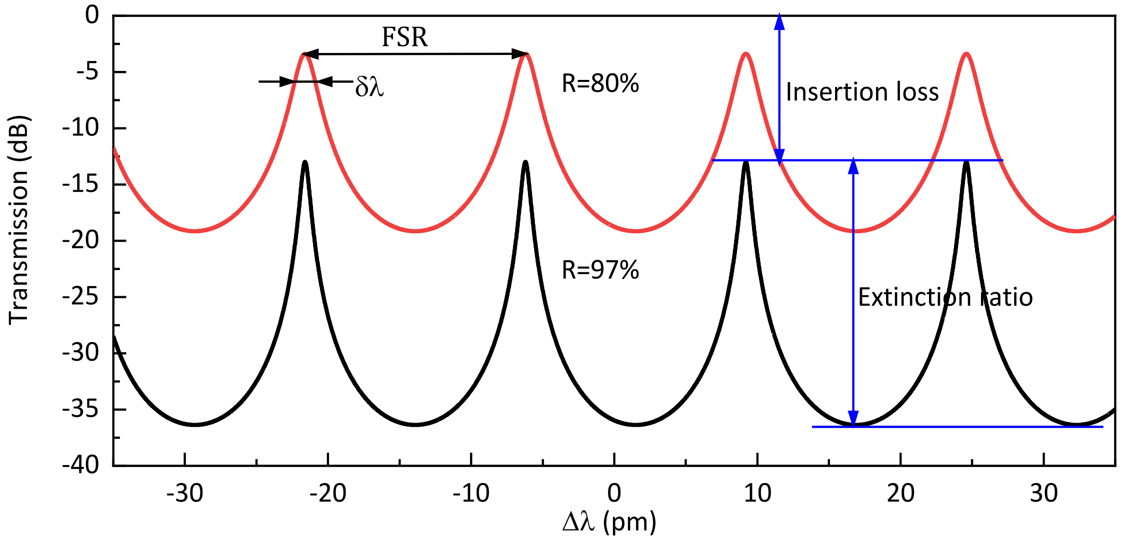

Figure 2.3 Calculated transmission characteristics of a lossy FP calculated using equation (2.5). FSR: free spectral range. FP length L= 8 cm, G=90% and mirror loss is not considered in the calculation.

2.2 FP parameters

Here, we define parameters commonly used to describe performance of FPs, namely, free spectral range (FSR), finesse (F), insertion loss (IL), extinction ratio (ER), Q value, build-up factor (BUF) and temperature sensitivity.

2.2.1 Free spectral range

As we see in Figure 2.3, there are several separated transmission peaks, which correspond to resonance condition, $\delta=2m\pi$, where m is an integer number. The optical frequency separation between these transmission peaks is defined as free spectral range (FSR), which is given by

$$FSR = \frac{c}{2n_g L}, \tag{2.6}$$

where n_g is the group index of transmitted mode in the FP and L is the cavity length.

2.2.2 Finesse

In Figure 2.3, we further see that the transmission peak spectral width depends on the reflectivity. We define $\delta\nu$ as full width at half maximum (FWHM) of the transmitted peaks described in optical frequency unit.

$$\delta \nu = c \frac{\delta \lambda}{\lambda^2} \tag{2.7}$$

Here, $\delta\lambda$ is FWHM of the transmitted peaks described in wavelength unit as shown in Figure 2.3. The finesse F is then defined as the ratio between FSR and $\delta\nu$, i.e.,

$$F = \frac{FSR}{\delta \nu}. \tag{2.8}$$

Straightforward derivation leads to finesse

$$\begin{aligned} F &= \frac{\pi\sqrt{RG}}{1-RG} \\ &\approx \frac{\pi}{1-RG} \end{aligned}. \tag{2.9}$$

The approximation is valid when RG is close to the unity. The finesse increases with reflectivity, and when the reflectivity approaches to the unity, the finesse changes dramatically with reflectivity. We also calculate how the achievable finesse changes as a function with transmission media loss α_l. In the calculation, we set R=1 and the FP length L=10 m. As we can see here, to realize an FP with long length and high finesse, the transmission media loss is a key parameter.

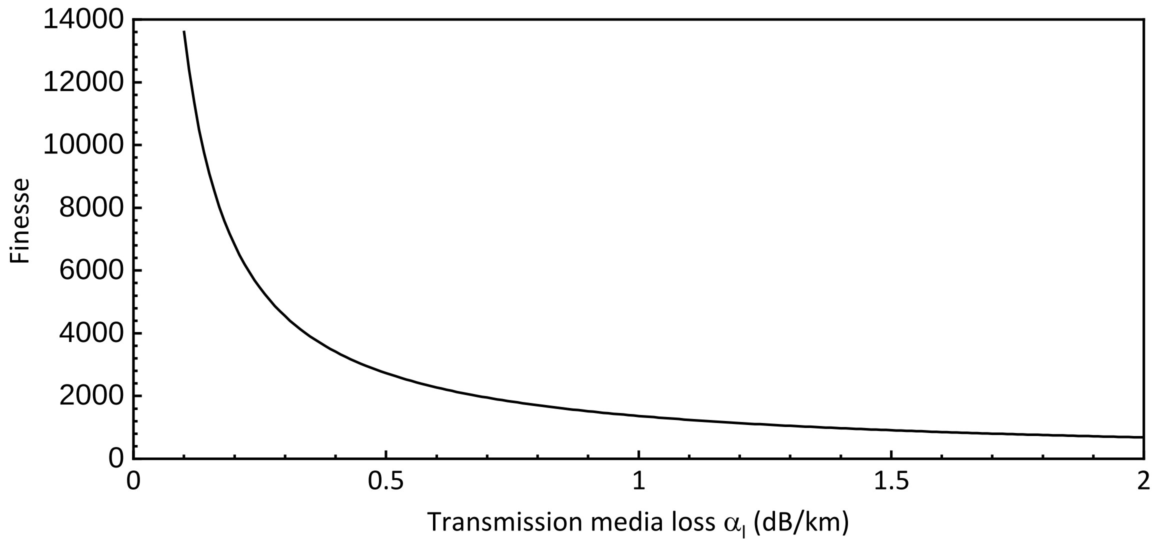

Figure 2.4 Finesse as a function with transmission media loss α_l

2.2.3 Insertion loss

Due to the above-discussed losses, the transmission at resonance $T_{resonance}$ is smaller than unity, as shown in Figure 2.3. It is typically expressed in dB as insertion loss (IL). The IL is defined as the transmission loss of an FP at resonance condition. By letting $\delta=2\pi$ in equation (2.5), we can get that

$$T_{\mathrm{resonance}} = \frac{T^2 G}{(1 - RG)^2}, \tag{2.10}$$

so that

$$IL = -10 \cdot \log_{10}(T_{resonance}) = -10 \cdot \log_{10}\left(\frac{T^2 G}{(1 - RG)^2}\right). \tag{2.11}$$

IL depends not only on the losses (i.e., transmission media loss and reflectors absorption loss), but also on the reflectivity of the reflectors. With the same G, IL increases with R.

After definition of these parameters, we can rewrite a FP's transmission (2.5) as

$$T_{FP} = \frac{T_{resonance}}{1 + (\frac{2F}{\pi})\sin^2\left(\frac{\pi\nu}{FSR}\right)}, \tag{2.12}$$

where $\nu = c/\lambda$ denotes the optical frequency.

2.2.4 Extinction ratio

Another important parameter, especially when an FP is used as a filter, is the extinction ratio (ER), which is typically described in dB as the ratio between maximum and minimum transmission, as shown in Figure 2.3. ER can be calculated straightforward from (2.12),

$$ER = 20 \cdot \log_{10}\left(\frac{1 + RG}{1 - RG}\right). \tag{2.13}$$

ER increases dramatically when RG approaches the unity. For example, when RG=90%, ER =25.58 while when RG=99.9%, ER=66.02.

2.2.5 Q value

Q factor, is also a used parameter for FPs, which is related to the peak width $\delta\nu$, namely,

$$Q = \frac{\nu}{\delta\nu} \tag{2.14}$$

where $\delta\nu$ is peak width $\delta\lambda$ described in frequency unit. Here, Q factor is defined as the ratio of the central frequency to its FWHM linewidth and we can effectively compare performance differences between different FPs. By substituting equation (2.6) and equation (2.8) into the above equation, we can get Q factor with a relationship as length and finesse as

$$Q = \frac{2n_g L}{\lambda} \cdot F \ . \tag{2.15}$$

Thus, Q factor is proportional to the finesse-length product.

2.2.6 Build-up factor

Earlier, we described how FP output field is obtained via coherent superposition of the light following i=1,2… roundtrips. Similar approach can be used to obtain optical field inside the FP cavity. Let us analyse the resonance case to get an insight into this. Due to the mechanism of FPs, light is interference inside the cavity. Let us consider the resonance case. Let $I_0= A_0^2$ be the intensity of the incident beam, and $I_t=|A_t|^2$ be the intensity of the transmitted beam. Inside the FP, the optical field can be written as the sum of the right-travelling wave with an Intensity I_1 (travelling along the $+x$ direction) and a left-travelling wave with an intensity I_2 (travelling along the $-x$ direction). Then the intensities at resonance are related by

$$\begin{aligned} I_t &= T_{resonance} I_0 \\ I_t &= T I_1 \\ I_2 &= RGI_1 \end{aligned} \ . \tag{2.16}$$

Then we can get the intracavity intensities as

$$\begin{aligned} I_1 &= \frac{TG}{(1-RG)^2} I_0 \\ I_2 &= \frac{T \cdot R \cdot G^2}{(1-RG)^2} I_0 \end{aligned} \tag{2.17}$$

The right-travelling wave interferences with the left-travelling wave, forming a standing wave inside the cavity, Figure 2.5. The intensity pattern in the cavity for $G \approx 1$ can be written as,

$$I(x) = I_1 + I_2 + 2\sqrt{I_1 I_2} \cos\left(2kx + \delta_0\right) . \tag{2.18}$$

Here, k is the wavenumber in the cavity, δ_0 is a constant phase due to possible phase shifts upon reflection from the cavity mirrors.

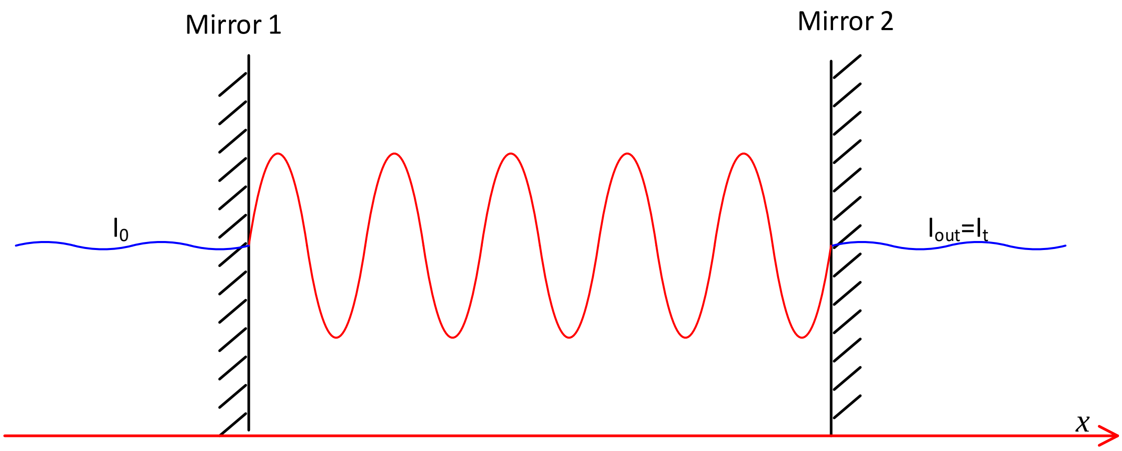

Figure 2.5 Optical intensity distribution inside the cavity at resonance.

The average intensity inside the cavity is then given by,

$$\begin{aligned} I_{ave} &= \frac{TG}{1-RG}\cdot\frac{1+RG}{1-RG}I_0 \\ &\approx \frac{1+R}{1-R}I_0 \end{aligned} \tag{2.19}$$

The approximation is obtained when there is negligible loss inside the cavity and in the mirrors. As we can see here, the average intensity inside the cavity can build up by several orders of magnitude when the reflectivity is close to unity, i.e., for an FP with high finesse. Here, we refer to the build-up times as built-up factor (BUF). Taking an example of a lossless cavity with mirror's reflectivity of R=0.9995, the IBF is 4000. The intensity build-up effect provides a method to enhance light-matter interaction, and we will show later that the intensity build-up effect at resonance can be used in different applications. Note, when other two losses are comparable to the transmission loss, e.g., when α_m=0.0004 and G=0.9999, they already reduce the IBF to 2200, which is a considerable reduction.

Besides the intracavity intensity, the dispersion is also enhanced by BUF at resonance. We define φ as the one-pass phase shift inside the cavity (i.e., $\varphi=\delta/2$). The interferometer transmission coefficient can be written, according to equation (2.4), as

$$t_e = \frac{T\sqrt{G}e^{-i\varphi}}{1-RGe^{-2i\varphi}} = |t_e|e^{-i\psi} \tag{2.20}$$

where ψ is the phase shift of the transmission beam. It can be shown that

$$\psi = \arctan\left[\left(\frac{1+RG}{1-RG}\right)\tan(\varphi)\right]. \tag{2.21}$$

Physically, the frequency derivative of the phase shift is the time delay (or group delay). If we write

$$\tau_e = \frac{d\psi}{d\omega} \quad \text{and} \quad \tau = \frac{d\phi}{d\omega} \tag{2.22}$$

where $\tau = \frac{nL}{c}$ is the single-pass time delay inside the interferometer and τ_e is the travelling time through the interferometer, then we obtain

$$\tau_e = \frac{d\psi}{d\varphi}\tau \tag{2.23}$$

Thus $\frac{d\psi}{d\varphi}$ may be viewed as an enhancement factor of the travelling time due to the Fabry-Perot effect.

The phase change and $\frac{d\psi}{d\varphi}$ inside a FP with different mirror reflectivity based on equation (2.21) and (2.23) are calculated, as shown in Figure 2.6. As a comparison, we also show the transmission spectrum of the FP. As we see here, the phase change of an FP in a free spectral range is π. At resonance, phase changes dramatically around the resonance and the time delay is enhanced significantly. The enhancement factor at resonance can be easily obtained from equation (2.23),

$$\frac{d\psi}{d\varphi} = \frac{1+RG}{1-RG}, \text{ when } \varphi=\pi,\ 2\pi, \cdots. \tag{2.24}$$

which is the same as BUF. Sometimes, we also use equivalent travelling length (ETL) to characterise a FP, which is defined as the ratio of time delay at resonance and speed of light in the transmission media,

$$ETL = \frac{1+RG}{1-RG} \cdot L \tag{2.25}$$

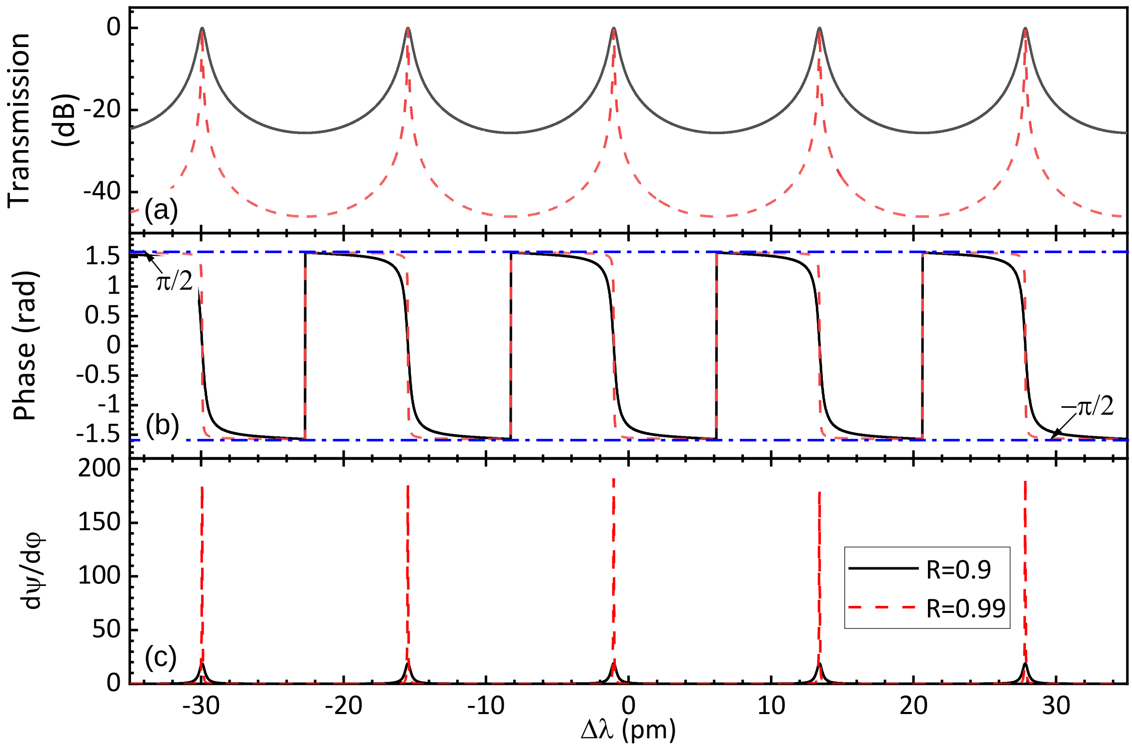

Figure 2.6 Calculated phase change (a) and delay time enhancement (b) inside the FP with different mirror reflectivity.

2.2.7 Thermal sensitivity of an FP

The resonant wavelength is given by the condition where $\delta=2m\pi$, thus we can get resonant wavelengths of an FP as

$$\lambda_m = \frac{2nL}{m}, \text{ m=1,2,3,}\cdots \tag{2.26}$$

When temperature changes, both refractive index n and cavity length L change, leading to a thermal drift of resonant wavelength. We define the temperature sensitivity (TS) of an FP as the wavelength drift per unit temperature,

$$TS = \frac{d\lambda_m}{dT} = \frac{2nL}{m}\left(\frac{1}{n}\frac{dn}{dT} + \frac{1}{L}\frac{dL}{dT}\right). \tag{2.27}$$

Sometimes, we also describe the resonant thermal drift by using optical frequency unit. We also use normalised temperature sensitivity (NTS), which is defined as temperature sensitivity normalised to operational wavelength,

$$NTS = \frac{1}{\lambda_m}\frac{d\lambda_m}{dT} = \frac{1}{n}\frac{dn}{dT} + \frac{1}{L}\frac{dL}{dT}. \tag{2.28}$$

Thus, NTS of an FP depends on the two effects, the refractive index of the transmission media's thermal response and cavity length's thermal response. FPs made of different material have different NTS, which we will discuss in details in the following section.

2.3 Structure of various Fabry-Perot interferometers

2.3.1 Free-space Fabry-Perot interferometers

The most classic FPs are free-space FPs, in which light propagates in air or vacuum. The most common structure of used free-space FPs are shown as in Figure 2.8 (a, b). Two mirrors are spaced either by a spacer or some optomechanical components. One or two concave mirrors are used to fulfil the stability criterion

$$-1 \le \left(1-\frac{L}{C_1}\right)\left(1-\frac{L}{C_2}\right) \le 1 \,[26] \qquad (2.29)$$

where C_1, C_2 are the radii of curvature of two mirrors respectively. To improve the thermal stability of free-space FPs, spacers made of material with low coefficient of thermal expansion (CTE) are typically used between mirrors. These low CTE material usually have a zero CTE at a specific temperature. As shown in Figure 2.7, the zero CTE temperature points of Zerodur from Scott [27] and ULE glass from Corning [4] are around room temperature and the zero CTE temperature point is at cryonic temperature [28]. When a free-space FP is long, the FP is difficult to align and very sensitive to environment fluctuation. The longest FP is the one used in Laser Interferometer Gravitational-Wave Observatory (LIGO) whose length is 4 km long [29] and to reach sufficient stability it is put into a seismically isolated environment with complex servo control system. Apart from this example, the free-space FP with the highest Q value of 1.7×10^{11} is formed by two optically contacted fused silica mirrors spaced by a 40 cm ULE-glass, which is shown in Figure 2.8 (c). The high Q value stems from a high cavity finesse of 282 000 and a relatively long cavity length [4].

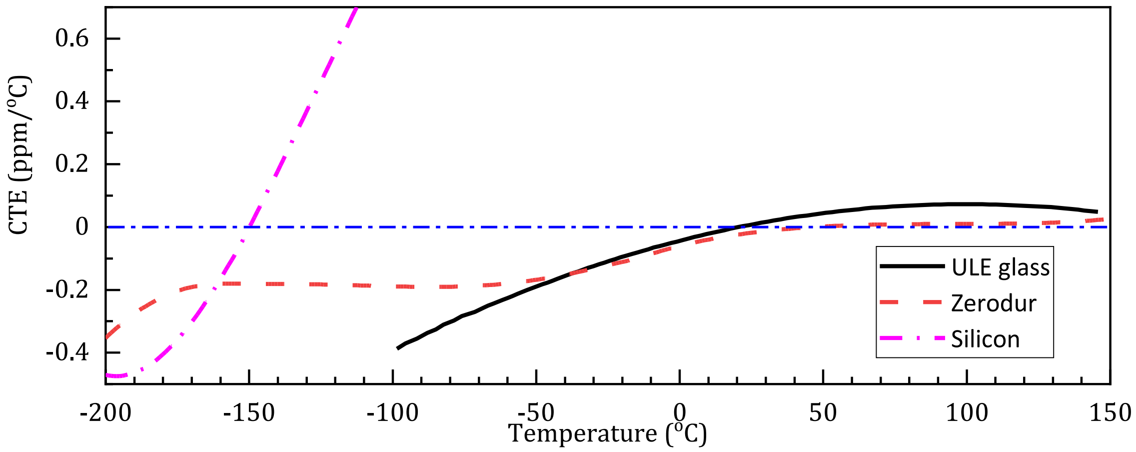

Figure 2.7 Examples of coefficients of thermal expansion (CTE) of some glasses at different temperatures. Data of Zerodur and Silicon glass are from the material library of COMSOL and data of ULE glass is from Corning's website [30].

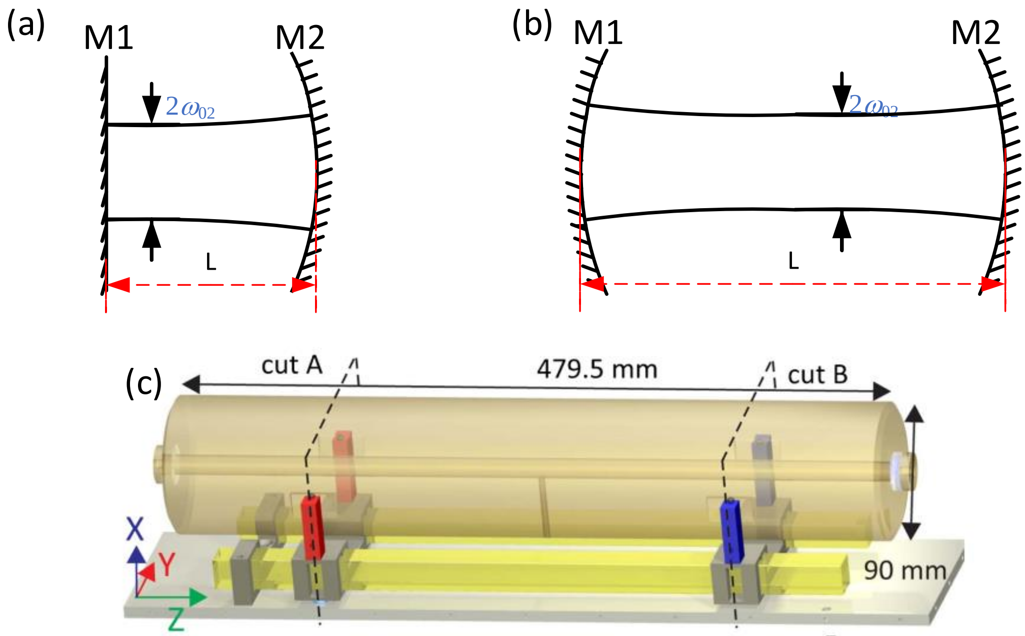

Figure 2.8 The schematic of two free-space Fabry-Perot interferometers with (a) one flat mirror (M) and one concave mirror; and (b) two concave mirrors. (c) An example of a free-space FP whose spacer is ULE-glass [4].

2.3.2 Single mode fibre based Fabry-Perot interferometers

Two commonly used single mode fibre (SMF) based FPs structures are shown in Figure 2.9. For the first one, the mirror is directly coated on the SMF ends, which is pre-polished. For the other one, the mirror is coated on the other two SMF ends, and then they are glued to an SMF at its both ends. The first one eliminates the requirement of adjustment but the achievable finesse is also limited by limited fibre end face flatness.

Compared to the free-space FPs, SMF based FPs are compact, easy to operate and easy to achieve long length. Thus, when the optical fibre's loss was reduced to an acceptable level in the 1980s, SMF based FPs were already studied in details [31–33]. Today, SMF based FPs are already mature commercial products. Finesse in excess of 2000 has been demonstrated with lengths of 10 m, enabling an EFL up to 13 km, and a Q factor of 3.7×10^{10} [34].

The mirror of SMF based FPs can also be made by with fibre Bragg gratings (FBGs), forming the so-called FBG-FP [35]. For this kind of FPPs, the achieved finesse is below 300 as the reflectivity of FBG is usually below 99% [7].

The thermal sensitivity of SMF based FPs depends on the SMF's property. For the traditional silica SMF-FP, its thermal sensitivity is 1.6 GHz/^{o}C [34] while normalised thermal sensitivity is 8.3 ppm/^{o}C.

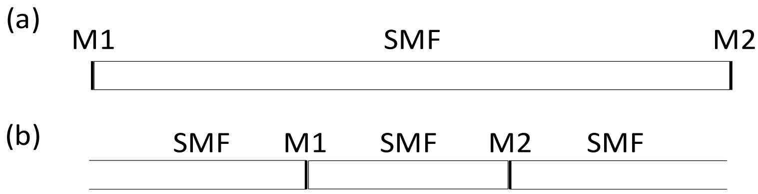

Figure 2.9 The schematic of SMF based FPs. (a) The mirror is directly coated at the SMF ends; (b) The mirror is coated on other two SMF ends and then a piece of SMF is inserted between the two coated SMF as the FP transmission.

2.3.3 Miniaturized fibre Fabry-Perot interferometers

In recent years, newly developed laser ablation techniques made it possible to fabricate high-quality mirrors directly on the facets of optical fibres, leading to the advent a new kind fibre-based FP, i.e., microcavity [36–39] formed in between two optical fibres end-facets as shown in Figure 2.10 (a). The concave dielectric mirror coatings are deposited on the fibre tips with small radius of curvature. Such FP cavity has small cavity volume and high finesse at the same time., of interest in cavity-enhanced experiments and applications. Main challenge is mode matching between the cavity mode and the fibre fundamental mode. As shown in Figure 2.10 (b), the cavity mode depends on the curvature of mirrors, mirror distance and the angle between the two mirrors. The coupling efficiency from the fundamental mode of SMF to the cavity mode can be calculated by the mode overlap between the fundamental mode of SMF and the cavity mode at the fibre end surface. The longer the cavity length is, the lower is the coupling efficiency. Mode matching efficiency of up to 90% has been achieved by using a concatenation of graded-index (GRIN) and multimode (MM)/core-less fibres spliced together [40]. The achieved finesse in this kind of FP is up to 100 000 [41] and the longest cavity length is limited to 600 μm [42].

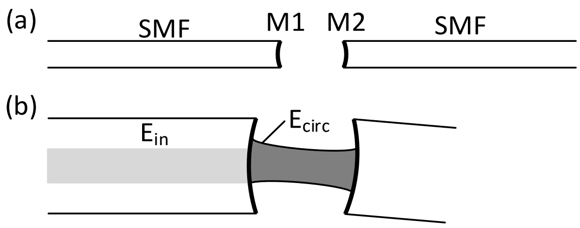

Figure 2.10 (a)The schematic of microcavity fibre FP and (b) geometry of its mode matching problem.

2.3.4 HCF Fabry-Perot interferometers

There have been several reports on HCF-FPs with high finesse. In 2018, Flannery reported a fibre-integrated FP formed by attaching a pair of dielectric metasurfaces mirrors at the end of HCFs [24], as shown in Figure 2.11(a). The achieved finesse was 11 due to the limited obtained reflectivity of the metasurface mirrors. In 2019, Tan reported an HCF-FP in which HCF is sandwitched between the mirrored SMFs [9], as shown in Figure 2.11(b). The SMFs and HCF are inserted in a mechanical splicer and fixed by glue. In 2021, the same group achieved a finesse of 700 with a 10-cm-long HCF[43]. Although the temperature thermal sensitivity of an HCF-FP with high finesse has not been reported, we can estimate it by an HCF's thermal sensitivity. For an HCF, it has been reported the thermal sensitivity at room temperature is 0.6 ppm/°C [14,15] . Thus, we believe that for an HCF-FP, its normalised temperature can also be as low as 0.6 ppm/°C.

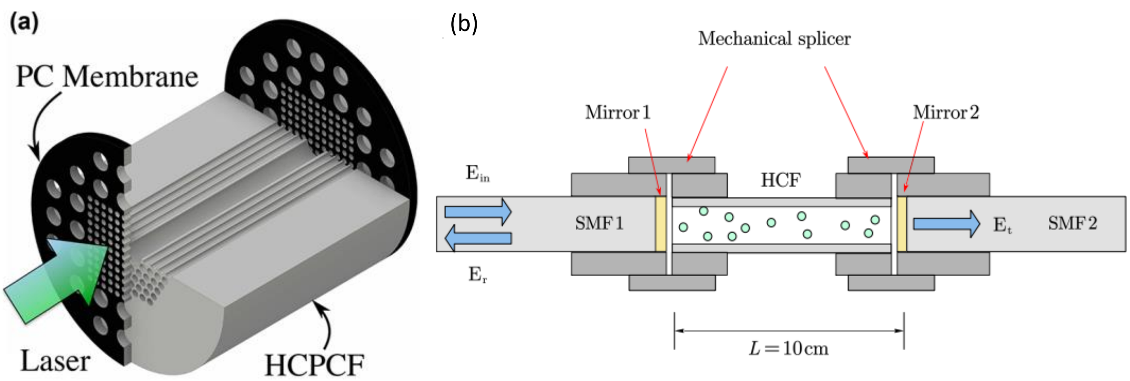

Figure 2.11 Reports on HCF-FPs. (a) HCF-FP made by attaching a pair of dielectric metasurfaces mirror at the ends of HCFs, picture adopted from [25]; (b) HCF-FP made by sandwiching an HCF between the mirrored ends of two SMFs, picture adopted from [43].

2.3.5 Comparison

The four mentioned types of FPs are summarised in the Table 2.1.

Table 2.1 Summarise of various HCF-FP structures

	Finesse	Length	NTS	Advantages	Disadvantages
Free-space FP	282 000 [4]	Typically, <50 cm	Close to zero	Low temperature sensitivity, low nonlinear effects	Bulky, difficult to align
SMF-FP	2000 [34]	Up to 10 m [34]	8.3 ppm/°C [34]	Easy to operate, compact	High temperature sensitivity, high nonlinear effects
Miniaturized FFP	100 000 [41]	< 700 μm [42]	Not reported		
HCF-FP	700 [43]	~ 10 cm [43]	0.6 ppm/°C [14]	Low temperature sensitivity, low nonlinear effects, Easy to operate, compact	

Free-space FPs have advantages like guiding light in air or vacuum and low temperature sensitivity when spaced with temperature-insensitive material [4], but they are bulky and difficult to align, especially to achieve high finesse. In contrary, SMF-FPs are compact and easy to operate, but their drawbacks make free-space FPs the preferred approach for many applications. The two primary drawbacks are the large sensitivity to temperature variations and unwanted nonlinear effects like stimulated Brillion scattering (SBS), especially in high finesse FPs where the intra-cavity power is strongly enhanced by the resonant effect. Both of these parasitic effects are mainly due to the interaction of light with the silica glass material in SMFs. For example, the thermal sensitivity of the FSR is dominated (95%) by thermally-induced changes in the n_g of silica glass (thermo-optic effect) with the thermally-induced fibre length (thermal expansion effect) change providing the remaining 5%. HCFs, as a kind of air/vacuum guided fibres, might solve above problems at the same time.

2.4 Applications of Fabry-Perot interferometers

2.4.1 Ultrastable laser

Ultrastable lasers that provide high-spectral purity are key components in a variety of advanced research directions, such as optical atomic clocks, gravitational wave detectors, photonic microwave synthesizers and communications. The most used method to achieve an ultrastable laser is to lock it to an ultrastable frequency reference, e.g., an FP made of a temperature-insensitive material, Figure 2.12. Such FPs are usually formed by attaching two concave mirrors to a spacer which is Zerodur from Schott [27], ULE glass [44] at room temperature or silicon working at a cryonic temperature where its thermal expansion coefficient is zero [28]. Both narrow-linewidth and long-term frequency stability can be achieved with this method. For example, a fractional frequency instability of 1×10^{-16} at short timescales and a laser linewidth < 40 mHz at 1.5 μm was achieved by locking a laser to a silicon spaced FP with a finesse of 240 000 and a length of 21 cm [45]. The FP they used has a narrow peak width about 3 kHz, by using HCF-FP, this can be achieved by using a 10 m HCF-FP and a finesse of 5 000.

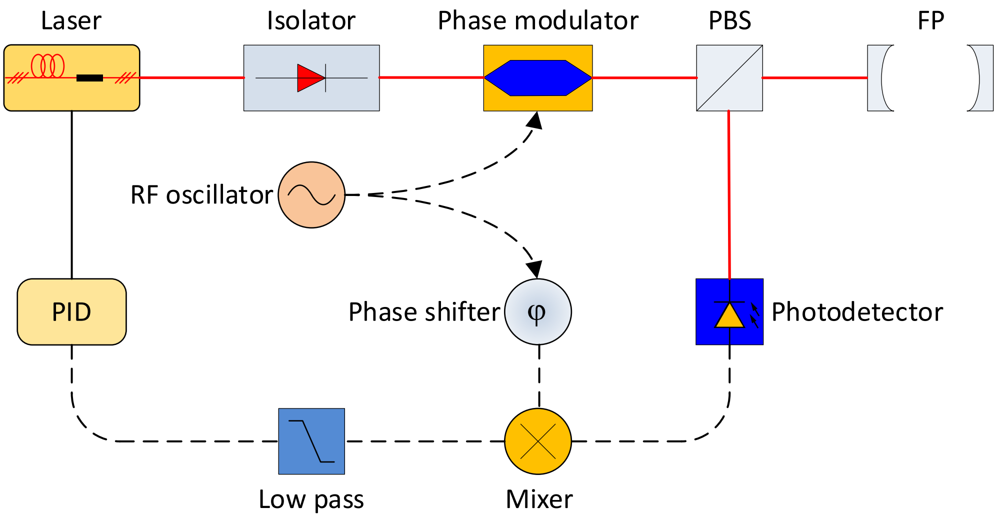

Figure 2.12 The schematics of laser frequency-locked to a stable FP. PBS: Polarisation beam splitter.

2.4.2 Sensing

FPs have broadband applications in the sensing field. Since the effective travelling distance at resonance of a high-finesse FP can be enhanced by many times, FPs with high finesse are usually used in ultra-precise sensing. The most famous one is perhaps LIGO, built to measure very weak gravitation waves. To achieve this, a strain detector must have a sensitivity below 10^{-21} ε $Hz^{-1/2}$. This is achieved by two 4 km-long FPs in two branches of a Michelson interferometer, as shown in Figure 2.13. The FPs here serve two functions: 1, It builds up the laser light within the interferometer, which increases LIGO's sensitivity (more photons make LIGO more sensitive); 2, It increases the distance travelled by each laser from 4km to 1200km thereby improving the sensitivity [29].

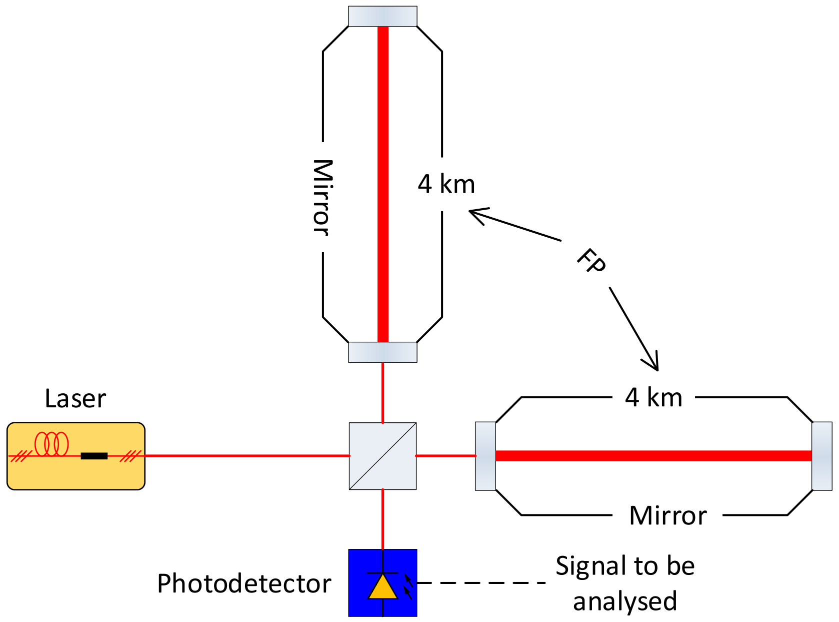

Figure 2.13 The schematics of Michelson interferometer with FP used in both arms in LIGO.

High-finesse FPs, especially fibre based FPs, are also used as sensors to measure strain, acoustic vibration, temperature, etc. Most FP based sensors share similar working principles. When external disturbance (e.g., longitudinal strain or temperature variation) is applied, internal parameters such as cavity length and refractive index are subject to a change. This in turn triggers a wavelength (frequency) detuning of the spectral features associated with these parameters. As a high-finesse FP provide narrow peak width, it provides better capacity of wavelength (frequency) discrimination thus high resolution. When the interrogation laser is frequency stabilised, these sensors can achieve a sensor with a sensitivity down to thermodynamic noise level [6].

When filled with gases, FPs can serve as cavity-enhanced gas sensors. The most used technique is cavity ring down spectroscopy (CRDS) [3]. In this technique, a pulse with a pulse width shorter than the round-trip time inside the cavity is injected into the cavity, and light can be reflected back and forth many times depends on the finesse before it totally gets out of the cavity. By measuring the exponentially decaying trace, one can measure the decay time of a cavity. By comparing the decay time with and without gases present, the concentration of gases can be measured. As the effective absorption length is enhanced by many times, CRDS provides a very high sensitivity down to parts per trillion (ppt) level. An HCF-FP made from photonics bandgap fibre has been used to measure oxygen [8]. However, due to the poor cavity mirror alignment and the used HCF loss, finesse as low as four was achieved, leading to a limited sensitivity. An HCF-FP with higher finesse and longer length may improve the measurement sensitivity further. The pollutants of HCF may be an issue in HCF-FP in the future, however, this can be solved by proper package which blocks dust and water.

For example, in the international standard EN 60529, IP 66 is very effective to be against dust and water [46].

2.4.3 Microwave photonics

In optoelectronic oscillators (OEOs), the phase noise typically decreases quadratically with the time delay [47], which could be significantly enhanced with an FPs cavity. Further, as FPs show a wavelength (frequency) dependent transmission, they can also be used as microwave photonics filters (MPFs). These two features were combined in an experiment in which a 10.3 GHz OEO was demonstrated using a 1 000 finesse FP. Comparing with a standard OEO loop, a 2 times higher radio frequency (RF) stability and lower phase noise was achieved [48].

2.4.4 Other applications

An example is a laser locked to an FP, which has its intensity noise filtered, resulting in a relaxation oscillation free laser[13] . When an optical frequency comb is transmitted through a FP with FSR same as its repetition rate, its noise can be filtered out thus leading to a higher sensitivity in detection system [11]. When an optical comb is transmitted through a FP with FSR n^{th} its repetition rate, the comb's repetition rate can be increased to n times thus leading to a comb with higher repetition rate [49].

2.5 Summary

FPs are widely used in many applications. HCF-FPs, as an air/vacuum guided fibre, combine the advantages of free-space FPs and FFPs. That is to say, HCF-FPs are compact, easy to operate and they have low thermal sensitivity and it is not easy to trigger unwanted nonlinear effect in HCF-FPs, which make HCF-FPs are very promising devices in many applications. Although there are several reports on HCF-FPs, several key questions are to be addressed. Firstly, I aimed to answer the question of how high finesse can be achieved with HCF-FPs. Furthermore, the reported HCF-FPs had their ends not sealed, enabling air-born pollution like water vapor and dust to enter the hollow core, possibly causing long-term HCF-FP performance degradation. Stable operation requires studying this effect or to seal the ends within the HCF-FP cavity.

Chapter 3 Background: Introduction of Hollow Core Fibre

In the previous chapter, I have briefly discussed the possibility of using a hollow core fibre in a Fabry-Perot interferometer. Here, I will discuss the historical development of hollow core fibres, followed by discussion the transmission mechanisms of various hollow core fibres. Properties of hollow core fibres, e.g., loss, chromatic dispersion, thermal sensitivity, are then introduced in details. As HCF-SMF interconnection is the key to obtain an all-fibred sealed HCF-FP, I will discuss this in the following section. At last, I will introduce different applications of HCFs.

3.1 Historical perspective

Since the landmark paper published by Kao and Hockham in 1966 [50], optical fibres have been used in a variety of applications, e.g., optical communication, fibre lasers and optical fibre sensors. In a conventional single mode fibre (SMF), light travels inside silica glass based on the internal reflection. As a backbone of modern industrial civilisation, the SMFs have seen remarkable development in term of transmission loss since the first demonstration of a sub 20 dB/km optical fibre by Corning in 1970 [51]. Today, the dominant loss in SMFs is limited by Rayleigh scattering arising from frozen-in density fluctuations in the glass. The lowest reported attenuation now is 0.1419 dB/km [22] of a Ge-free SMF at 1560 nm where the Rayleigh scattering loss (~0.1 dB/km) is the dominant loss [53]. Further significant reduction of the Rayleigh scattering loss is unlikely since the gap in fictive temperature between fibre and bulk is now mostly closed[22], making it difficult to reduce the fibre loss further for the conventional SMFs. Meanwhile, as there is overlap between light and glass in SMFs, the conventional SMFs have some inevitable drawbacks, e.g., nonlinearity, dispersion, high power induced damage & limited transmission bandwidth. Due to these facts, and that “vacuum is the very best optical material”, optical fibre which enables light travels in air or vacuum has always attracted people’s interest [54].

Different to the conventional SMF where light travels based on the internal reflection, hollow core fibres (HCFs) require a different mechanism to guide light. The very early idea was to use a mirror-covered wall to encircle a hollow core. However, metallic mirrors have limited reflectivity, resulting in high propagation loss. The key conceptual advance came in 1991 when Russell at the University of Southampton suggested a periodic array of wavelength-scale holes along the length of an optical fibre can create a photonic-crystal effect. He then added subwavelength holes to fibre to create a photonic-crystal geometry, creating an artificial low-index cladding to confine light into a higher-index solid core[55], Figure 3.1. Although this was not an HCF, it suggested using microstructure inside a fibre to confine light. The first microstructure-enabled HCF was reported in 1999, when

Russell's group confined light by surrounding the central hole with a type of photonic crystal called a photonic band gap[56],Figure 3.1. Today, this kind of HCF is called the photonic bandgap fibre (PBGF) or hollow core photonic bandgap fibre. Fabrication of the first photonic band gap fibres required stacking hundreds of silica capillary tubes and thin rods to make a preform to be drawn into a fibre.

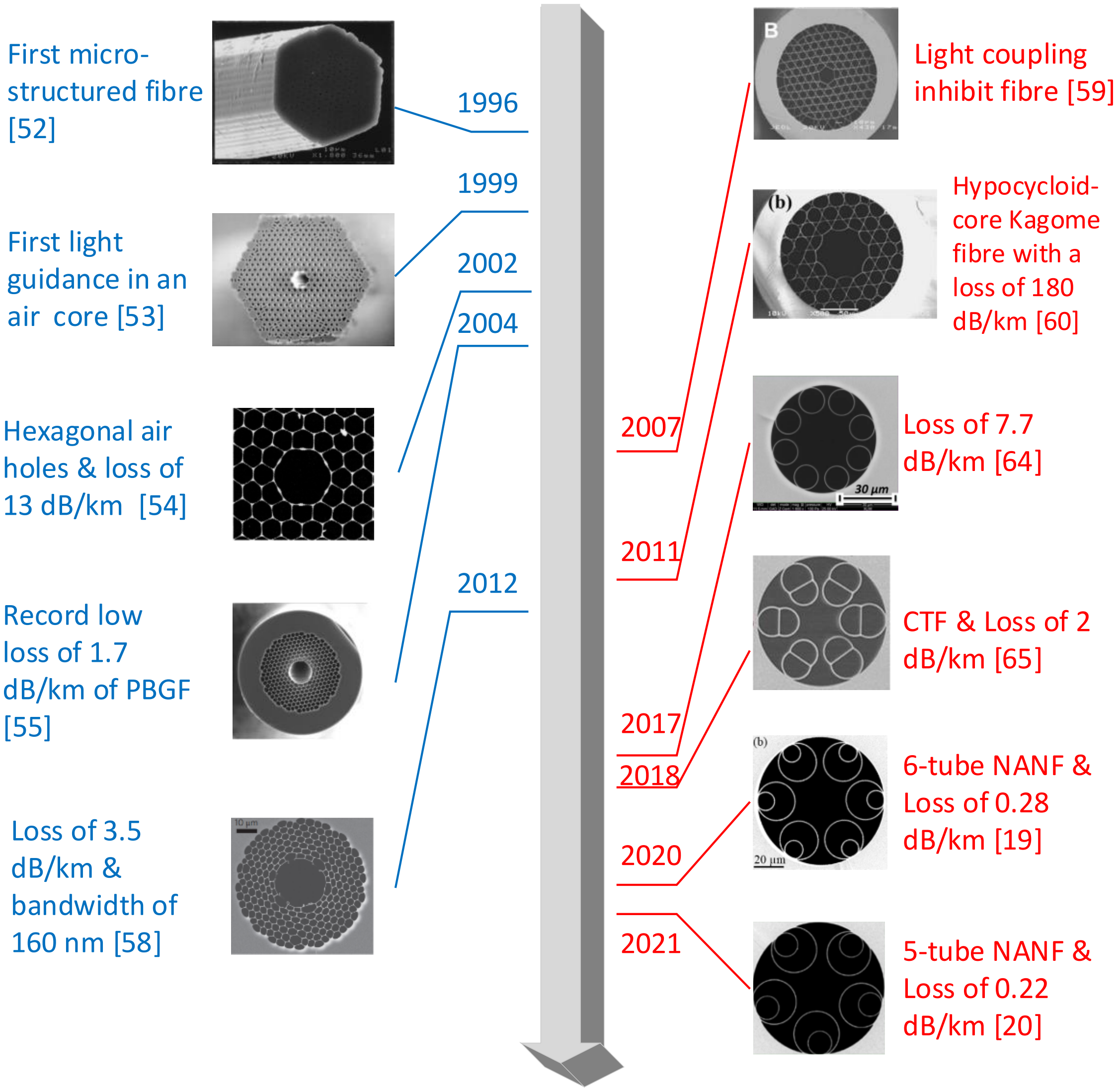

Figure 3.1 History of HCF development (Selected works).

Following the opening of the this development door, further research reduced fibre loss. Corning Inc. reported a loss of 13 dB/km in a seven-cell PBGF in 2002 [57] and a group at the University of Bath led by Russel subsequently reduced the fibre loss to 1.7 dB/km in a 19-cell PBGF in 2004 [58,59], Figure 3.1. The cladding of these two PBGFs was a hexagonal mesh of thin glass struts—mostly air—surrounding a nearly circular central hole. The record-low loss came at the cost of introducing resonances that narrowed the low-loss band to less than 20 nm, with loss peaks of 20 to 30 dB/km on each side. Further, numerical simulations found that PBGF may suffer from mode and polarization instabilities, which could threaten their usefulness for high-capacity data transmission

[60] . Usable bandwidth was increased by minimizing thickness of the glass struts in 2013, when Poletti's group in the University of Southampton reported a minimum loss of 3.5 dB/km and a 3-dB bandwidth of 160 nm [61], Figure 3.1.

However, in PBGFs, the electromagnetic field intensity on their surfaces is higher than around the rods, especially for the struts surrounding the core, where the modal intensity is higher. This causes significant scattering at the air-glass surfaces, which are intrinsically 'rough' due to frozen in thermodynamic fluctuations. As a result, surface scattering loss is the dominant loss in PBGFs and it is difficult to reduce it [24]. Then researchers turned their interest to antiresonant mechanism to guide light in the hollow core. In the 1990s, it was predicted that an antiresonant layer between a hollow core and the surrounding cladding could confine light by reflecting it back into the core [62]. Support for that idea came from experiments with a structure originally thought to guide light in a hollow core by creating photonic band gaps: hexagonal lattices of thin glass, called Kagome after a traditional Japanese pattern for woven bamboo [63]. In 2007, a group at Bath experimenting in guiding multi-octave frequency combs found that the light-guiding depended not on reflection back into the core, but on prevention of light coupling between core and cladding modes [64], Figure 3.1. Wang and others then at Bath subsequently tested a kagome fibre with ice-cream-cone-shaped hypocycloid curves facing into the hollow core [63], Figure 3.1. The team found that negatively curved surfaces facing the core created an antiresonance that damped down coupling of light from the hollow core into the cladding. This demonstration of antiresonance guiding in a hypocycloid kagome fibre was an important early step toward a new class of fibres called antiresonant fibres (ARFs). The next advance came in 2013 [65] and 2014 [66], when Belardi at Bath showed numerically that negative curvature improved light confinement inside the hollow core. He created the negative curvature by fabricating a single layer of hollow tubes that run along the inside of a hollow tube. Then in the early 2014, he developed the crucial new concept of the nested ring design, which added a second smaller hollow tube inside each tube in the negative-curvature layer, Figure 3.2(a). Doing that, as well as keeping the parallel tubes from touching, reduced light coupling from the core into the cladding, and thus reduced fibre attenuation. Following Belardi's work, still in the 2014, Poletti proposed a hollow-core fibre design shown in Figure 3.2 (b) that he called a nested antiresonant nodeless hollow-core fibre (NANF) [24]. His analysis indicated that the attenuation in NANF fibres due to leakage, surface scattering and bending could be lower than for conventional solid fibres. Removing the nodes where tubes touched could give the NANF fibre a low-loss antiresonant band an octave wide, and suppress high-order modes well enough to make the fibre effectively single mode. Experiments confirmed the promise of the design. In 2017, a team at the University of Limoges, France, reported transmission loss of 7.7 dB/km at 750 nm in a hollow-core fibre with a single nodeless ring of tubes[67], which is just 3-4 times of the Rayleigh scattering loss of SMFs at that band [23].

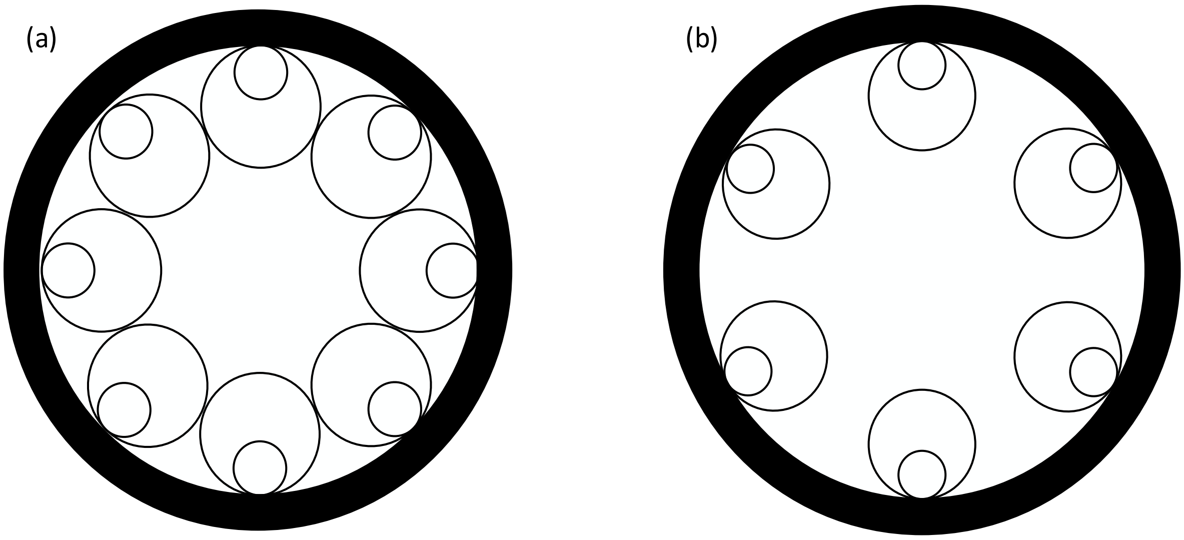

Figure 3.2 Antiresonant fibre geometries proposed by (a) Belardi [66] and (b) Poletti [24] in 2014. The latter one is the well-known NANF structure.

The breakthrough low loss results came at 2018, when Wang reported a minimum loss of 2 dB/km at 1512 nm with her conjoined-tube fibre (CTF) [68], Figure 3.1 and Optoelectronic Research Centre (ORC) in the University of Southampton reported minimum loss of only 1.3 dB/km at 1450 nm in the NANF fibre—the first hollow-core fibre to beat the 1.7 dB/km for a PBGF reported at 2004 [17]. Results then improved steadily in ORC. At 2019, they reported a minimum loss of 0.65 dB/km across the full erbium-fibre amplifier band—half the loss of the fibre they had reported just a year before, a performance reportedly attributable to improvements in tube handling, preform fabrication and pressurization, which improved uniformity along the fibre length as well as cross-sectional symmetry[18]. Simulations suggested that the loss included 0.31 dB/km of light leakage and 0.24 dB/km of micro bending, which might be eliminated—leaving a fundamental loss of only 0.1 dB/km from surface scattering, which is the only truly fundamental loss mechanism of the fibre. Continuing refinements in the design and fabrication of hollow-core NANF fibres more than halved attenuation, ORC then reported a Loss of 0.28 dB/km between 1510 and 1600 nm, Figure 3.1, and close to 0.3 dB/km between 1500 and 1640 nm for a 2.8-km fibre at 2020 [19]. At 2021, the record low loss was improved further to 0.22 dB/km, Figure 3.1, from 1625 nm to 1640 nm for a 2.2 km fibre. This progress was achieved by moving from the 6-tube NANF into a 5-tube NANF[20]. Just recently, a new record low loss was reported to be 0.174 dB/km at C band with a structure which adds an extra smaller hollow tube inside each second tube in NANF, which is called double nested antiresonant nodeless fibre (DNANF) [21]. Although the attenuation is still lower than the lowest value of Ge-free SMF, it already surpasses the attenuation of conventional germanium-doped SMF in the O and C bands.

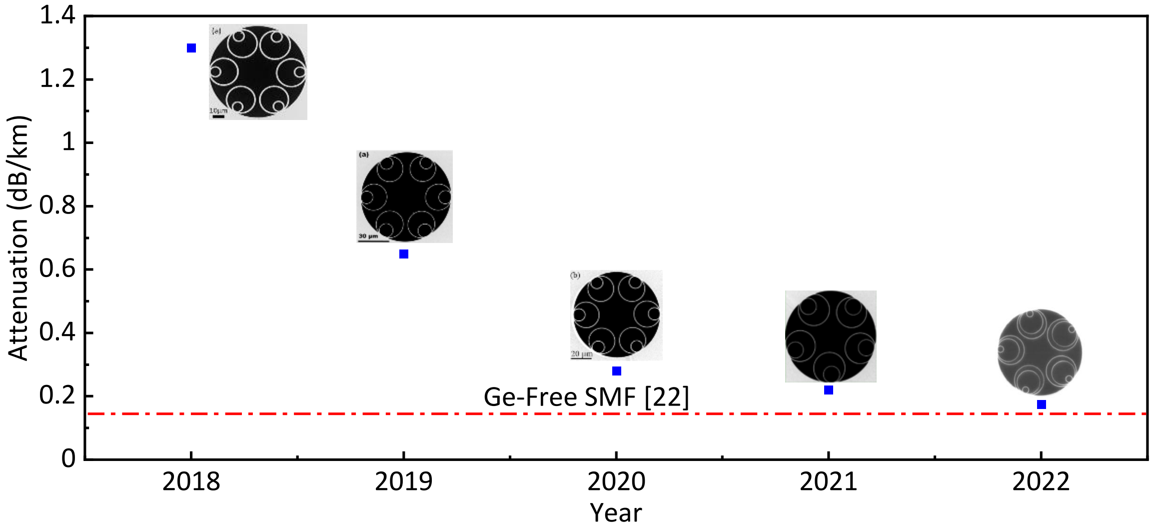

Figure 3.3 The reported attenuation reduction of NANF in ORC, University of Southampton

The NANF's loss reduction in ORC is summarised in Figure 3.3. Although there remains a small gap between the lowest loss of NANF and that of SMFs, NANF has witnessed breakthroughs over the last couple of years and further improvement can be expected in the near future.

3.2 Hollow core fibre guiding mechanism

3.2.1 Photonics bandgap fibres

To understand the confinement mechanism in PBGF, we first review the PBG guidance in 1D structure, Figure 3.4(a). The structure consists of two materials with different refractive index n_1 and n_2, which are arranged with a period Λ. In such a structure, light is reflected when constructive interference occurs, which is described by Bragg's law:

$$N\lambda = 2\Lambda \sin\theta \, . \tag{3.1}$$

Here, λ denotes the wavelength of light and θ the incident angle. Thus, light with a range of wavelength $\Delta\lambda$ around λ can be reflected for a range of angles $\Delta\theta$. The concept can be expanded to a 2D structure, Figure 3.4(b), and for the large enough angles that experience total reflection in the 1D structure, light cannot travel in any direction in the 2D structure, making it trapped in the central defect. This is how light is confined in a PBGF.

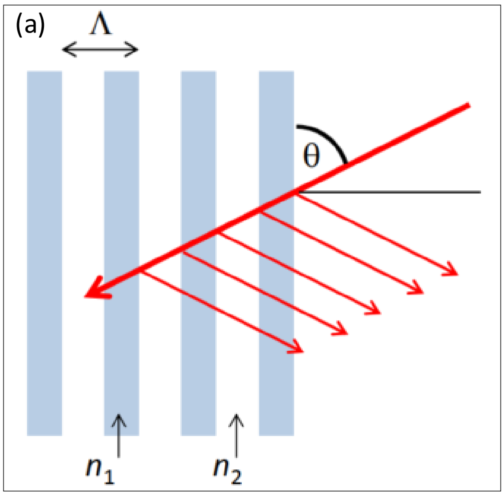

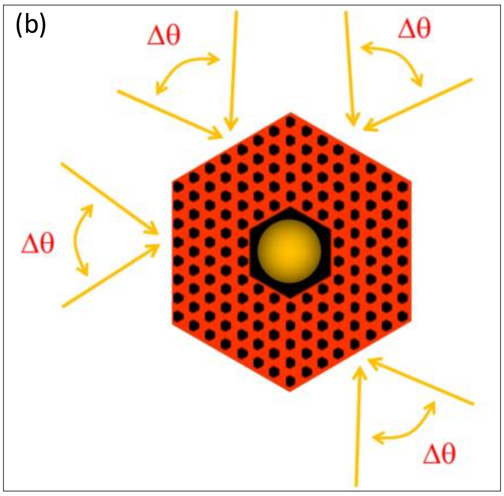

Figure 3.4 Explanation of PBG effect in (a) 1D structure and PBG guidance in (b) 2D structure.

3.2.2 Antiresonant fibres

Examples of antiresonant fibres can be found in Figure 3.1. The simplest model to explain the guidance in ARFs is a thin hollow core glass capillary, Figure 3.5 (a). The refractive index of glass is n_1 while it is n_0 for air, and the thickness of the glass is t. For light that travels inside such a hollow core, its effective index is very close to the refractive index of air, that is to say, the longitudinal propagation constant β equals to n_0k (k is the wavevector of light) in the hollow core so that in the glass sheet the transverse propagation constant $k_e = \sqrt{k^2 n_1^2 - \beta^2} \approx k\sqrt{n_1^2 - n_0^2}$ when the air mode is phase matched to glass modes in the struts. After traveling forth and back once in the glass sheet, the phase change of light will be $2k_e t$. Let us suppose that the phase of light is Φ_0 when it gets through the glass sheet directly while it is Φ_1 when light is reflected twice at the boundary of air-glass interface before it gets out of the glass sheet. The phase difference between Φ_0 and Φ_1 should be $2k_e t$. When the phase difference

$$2k_e t = 2kt\sqrt{n_1^2 - n_0^2} = 2m\pi, m \in N^+ , \tag{3.2}$$

the two waves getting through the glass sheet interference constructively. Such a situation is called resonance condition. When

$$2k_e t = 2kt\sqrt{n_1^2 - n_0^2} = (2m+1)\pi , \tag{3.3}$$

the two waves getting through the glass sheet interference destructively so that the reflection of the inner glass wall is strengthened. Such a situation is called antiresonance condition. In antiresonance condition, light can be confined in the hollow core. For the air or vacuum guided HCF, n_0 is very close to 1. We can get the antiresonance wavelength as

$$\lambda_m = \frac{2t}{m-0.5}\sqrt{n_1^2 - 1}\,. \tag{3.4}$$

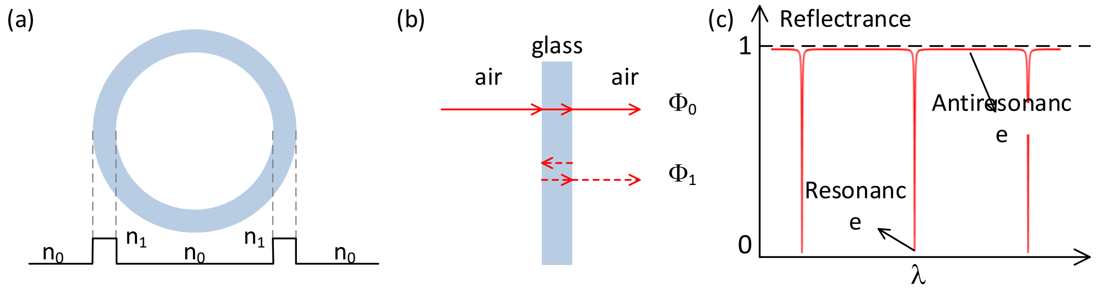

Figure 3.5 (a) The resonance condition in a thin glass sheet and (b) antiresonance guiding in hollow core fibre.

When the wavelength is close to the antiresonant wavelength, the reflection of the glass sheet will be increased with respect to a single air-glass interface leading to confinement of light in the hollow core. Especially when the reflectance of air-glass condition is high, the reflectance spectrum can be broad (see Figure 3.5(c)), which leads to a broad transmission band in ARFs. The high reflectance is achieved thanks to a large incidence at air-glass boundary, similar to the situation of grazing incidence. As each integral m in (3.4) represents an antiresonant condition, there are several transmission windows of ARFs. As the antiresonant wavelength is inversely proportional to m, the higher m is, the narrower the transmission window is.

The key conclusion is that the major difference between ARFs and PBGFs lies in their confinement structures. PBGFs have many layers of thin-walled holey lattices of glass in their inner cladding while ARFs have ARFs typically have only several tubes.

3.3 Fabrication of hollow core fibres

The most common fabrication method of HCFs is called stack-and-draw process[69,70]. To make a PBGF, in the first step, bundles of metre-long, ~mm diameter silica glass capillaries are manually stacked together with a required geometry based on the PBGF design and packed tightly inside a jacketing tube to make a primary preform (typical diameter in the range 20-30 mm), Figure 3.6 (a). The hollow core is formed by removing capillaries from the centre of the stack (e.g., to form a symmetric low-index core we can remove 3, 7, 19 or 37 capillaries, thus so-called 3-, 7-,19- and 37-cell PBGFs are drawn). In the second step, the primary preform is fused and scaled down to a “cane” (typically 1-3 mm diameter), Figure 3.6 (c). In the further step, the cane is placed inside a second jacketing tube and the assembly is drawn into the final fibre, Figure 3.6(d). In this case, pressure differentials are used to substantially increase the ratio between the hole diameter and inter-hold separation of the cladding holes, while scaling down to their overall size. The fabrication process of ARFs is similar as PBGF but with much lesser glass capillaries. Figure 3.7 shows the cross-sectiona of a 5-tube NANF preform and the fibre drew from it [69].

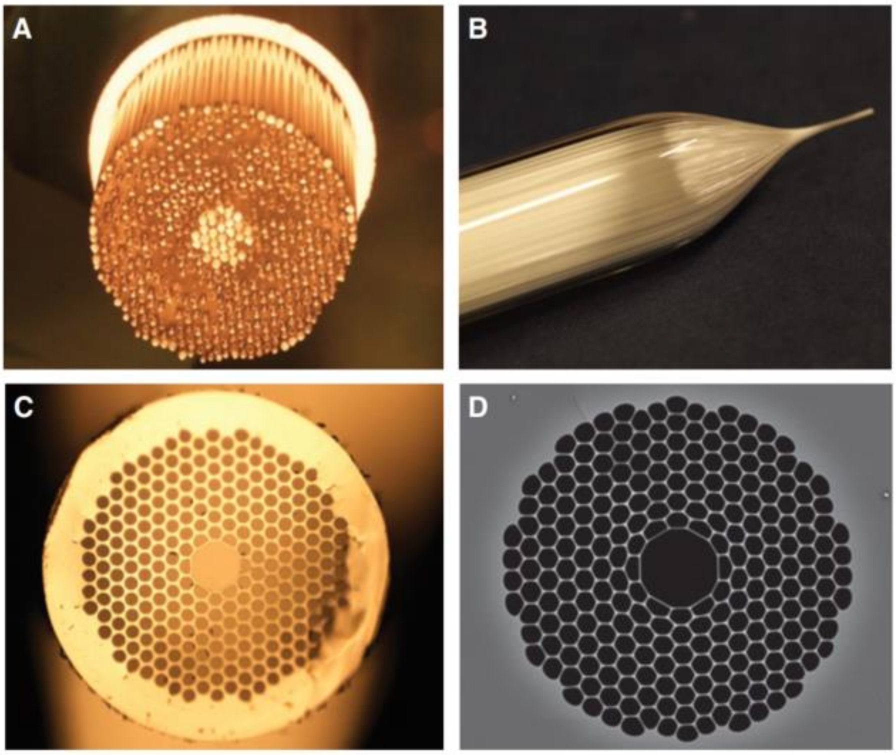

Figure 3.6 PBGF fabrication process flow using the “stack and draw” technique: (a) primary preform obtained by assembling a few hundreds of silica glass capillaries; (b) first stage draw of the primary preform into a ~millimetre sized “cane”; (c) optical image of the cross-section of an PBGF cane; (d) scanning electron microscope (SEM) image of the microstructured region of the final fibre .

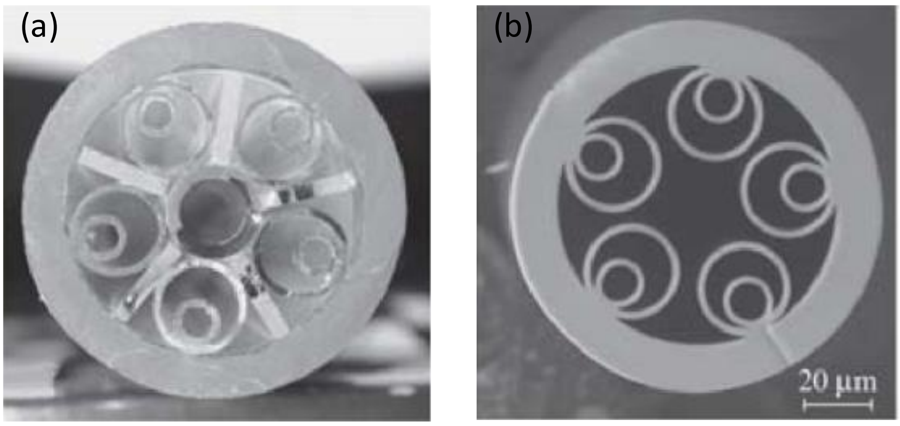

Figure 3.7 (a) Preform assembly with silica elements between double capillaries and (b) cross-sectional SEM image of the ARF drawn from the preform [69].

3.4 Properties of hollow core fibres

Most HCFs' unique properties compared to SMFs originate in the fact that light travels in HCF mostly through air or vacuum rather than silica glass. Some of these properties are common to all HCFs, e.g., latency close to that of light in vacuum, while other properties such as chromatic dispersion depends on the guiding mechanism (PBGF or ARF) or the fibre design. In this thesis, we mostly focus on ARFs and specifically to ARFs in the NANF geometry [24].

3.4.1 Attenuation

The attenuation of HCFs consists of confinement loss (CL), surface scattering loss (SSL), and bending loss (BL). For an ideal straight HCF which keeps its size and whose glass wall is smooth along the transmission direction, its transmission loss is given by the CL. The CL is the intrinsic loss from the leakage nature of the HCF, which sets the ultimate loss of an HCF. The simulations in different literatures give a CL ranging from 0.01 dB/km to 1 dB/km in [24,64,67] depending on the design structure. However, in a real HCF, surface wall of the silica glass tubes becomes rough in the thermally driven process during fibre fabrication. Due to the existence of this surface roughness, light is scattered from the fundamental mode to other modes that cannot be guided in an HCF [72], leading to SSL. Based on [72], SSL can be estimated by

$$SSL(dB/km) = \eta F_a \frac{\lambda^3}{\lambda_0^3} \tag{3.5}$$

Here, λ is the operating wavelength and Fa is a normalised parameter which can be calibrated at a selected wavelength λ_0. η is the fraction of the power of the fundamental mode of the silica glass boundary (or the fundamental mode field overlap with the silica glass), which can be calculated by

$$\eta = \frac{\int_{glass} \mathbf{e} \times \mathbf{h}^* \cdot \mathbf{z} dA}{\int_{A\infty} \mathbf{e} \times \mathbf{h}^* \cdot \mathbf{z} dA} \tag{3.6}$$

where **e**,**h** are the electric field and magnetic field distribution of mode and **z** is the unit vector parallel to the waveguide axis. In NANF [24], light confinement by the antiresonance mechanism results in typically very small η (about 0.016% in [17]) and therefore leading to a significantly smaller SSL as compared to PBGF, reaching below 0.1 dB/km based on the simulation in [24]. Besides, SSL scales with wavelength and it becomes larger at shorter wavelength. BL consists of two origins, i.e., microbending loss and macrobending loss. The microbending loss mechanism results from microscopic and randomly arranged lateral loads exerted on the fibre, e.g., when this is wound on a drum with a rough surface or within a cable[73]. The macrobending loss indicates the increasing loss of an HCF when it is subjected to bending. Typically, these losses rise very quickly once a certain critical bend radius is reached. Since HCFs have larger mode size than SMFs, they are typically having large macrobending loss than SMFs. When an HCF works at wavelengths where the host material becomes opaque and highly absorption [74], there is also another loss, i.e., material absorption loss (MAL).

Although NANFs' loss at communication band still remains a gap as compared to SSMF, Due to the lower density of gases inside the HCFs, it decreases the Rayleigh scattering coefficient and thus the related loss contribution by 2-3 orders of magnitude compared to the conventional SMFs [23]. This makes HCF's attenuation between 600-1100 nm has beat the Rayleigh scattering limit of silica glass at selected wavelengths, Figure 3.8.

At longer wavelength, e.g., mid-infrared region, silica absorption loss can be over 10^4 dB/m thus solid silica fibres are opaque. The significantly smaller modal overlap in HCFs can make silica HCFs transmissive there. A loss of 18 dB/km at 3.16 μm and 40 dB/km at 4 μm has been achieved with tubular ARFs. Simulations have shown that the six-tube NANF with optimised structure parameters can achieve a minimum loss of 24 dB/km at 4 μm while the silica's absorption loss is 863 dB/m [74]. However, beyond 5 μm NANF exhibit no advantages due to huge material absorption loss. A simulation also reveals that by combining the antiresonant and photonic bandgap guidance mechanisms and choosing proper glass with lower absorption loss than silica, a total loss of few dB/km level can be achieved through mid-infrared wavelengths (5 μm-10.6 μm) [51].

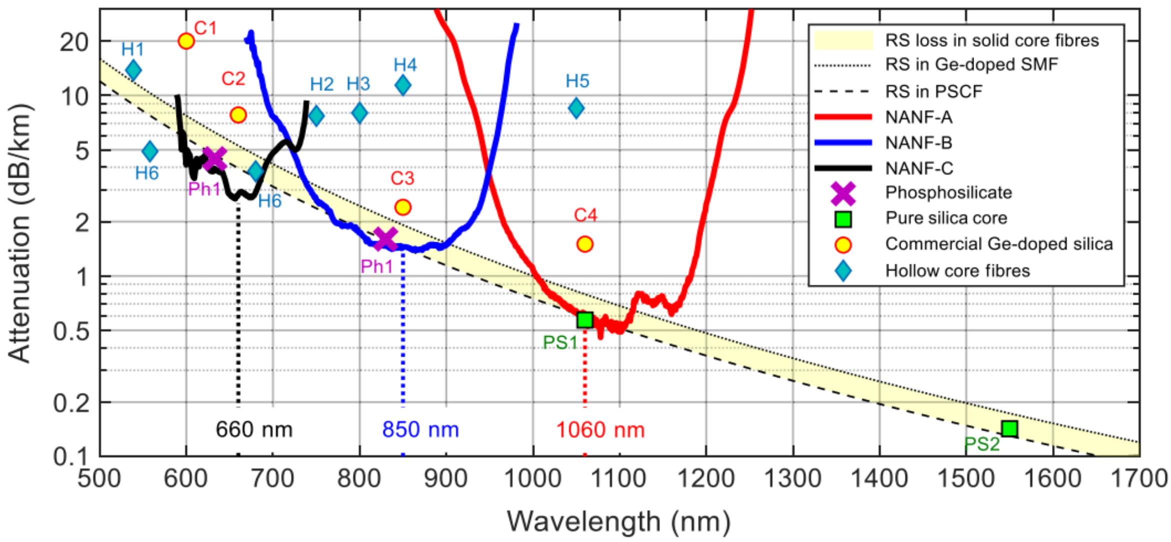

Figure 3.8 Attenuation of NANFs reported between 600-1300 nm in [23].

3.4.2 Higher order modes

The existence of the nested tubes inside the NANF structure shown in Figure 3.2(b) offers an opportunity to strip the higher order modes (HOMs). There are air-modes guided inside the antiresonant tubes, called cladding modes by Poletti [24]. Based on Poletti's simulation[24], the effective indices of these cladding modes can be strongly influenced by changing the distance between the two touching tubes of NANF and they always remain below the LP_{01} effective index and can cross the LP_{11} mode line. As a consequence, fibres with nested resonators of approximately parameters will have a very efficient resonant out-coupling of the LP_{11} mode which will considerably increase its loss. For a fixed R shown in Figure 3.9, Poletti calculated how z (or the inner tube size) influences on the fundamental mode (LP_{01}) and the first 5 core guided modes (LP_{01}, LP_{11}, LP_{21}, LP_{02}, LP_{31})'s refractive indices and loss, as shown in Figure 3.9. It shows that operation around z/R ~0.25 or 1.1 enables maximum suppression of the lowest loss HOM (LP_{11}), which can result in HOM extinction ratios in excess of 500. The drawn fibre of these NANFs in ORC have reported LP_{11} mode with a loss between 11-700 dB/km [17–19] with the 6-tube structure. The more promising result comes with the latest 5-tube NANF whose LP_{11} mode has a loss of 2800 dB/km while its LP_{01} has a loss only 0.22 dB/km [20] with proper choice of R and z thus leading to an effective mode-matching between LP_{01} mode and CMs.

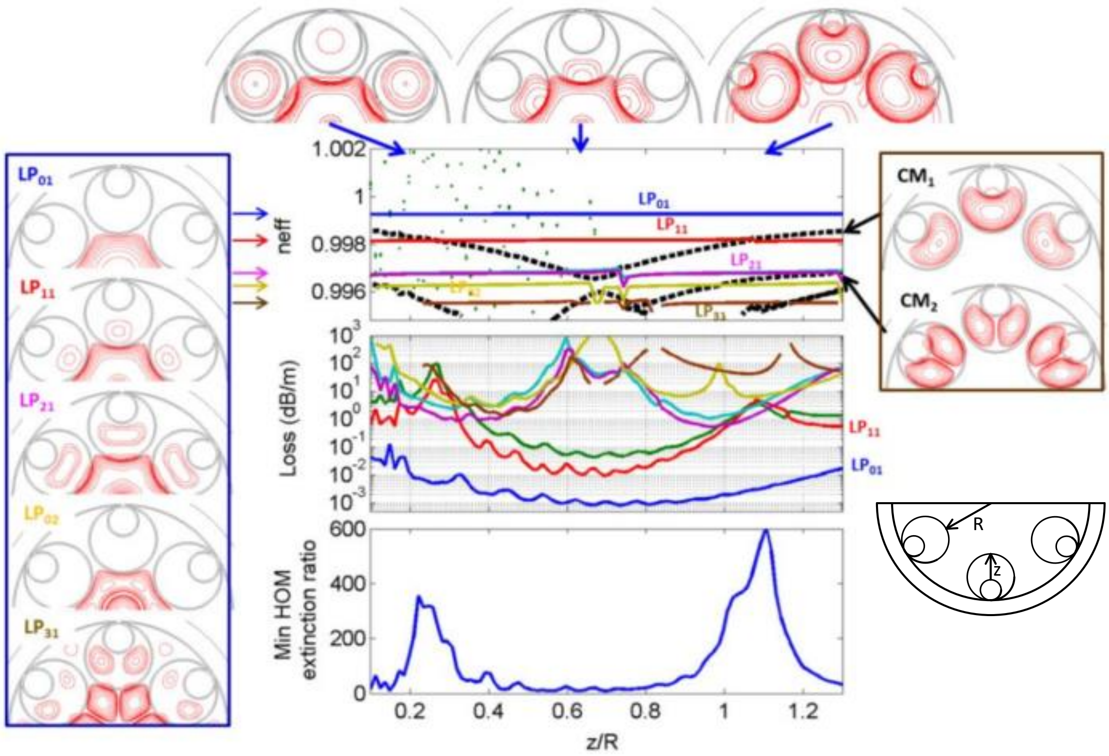

Figure 3.9 The effects of changing size of the inner nested tube in a NANF with a fixed R. When z is changed, the cladding modes shown on the right resonantly interact with different core modes (shown on the left).

3.4.3 Chromatic Dispersion

The chromatic dispersion coefficient in an optical fibre is given by

$$D(\lambda)=\frac{d\tau(\lambda)}{d\lambda}=\frac{d(1/v_g)}{d\lambda}=\frac{1}{c}\frac{d(n_g)}{d\lambda} \tag{3.7}$$

where $\tau(\lambda)$ indicates the delay time per unit length (km) while λ, wavelength, v_g the group velocity, n_g the group index. In an HCF, the overlap between the optical mode field and the glass is very small, so we neglect glass's material dispersion. In such a case, the group velocity can be approximated by[54]

$$\begin{aligned} n_g &= \frac{1}{cn_{eff}}\frac{\int_{A\infty} n^2(x,y)\mathbf{e}\times\mathbf{h}^*\cdot\mathbf{z}dA}{\int_{A\infty}\mathbf{e}\times\mathbf{h}^*\cdot\mathbf{z}dA} \\ &= \frac{1}{cn_{eff}}\left[\frac{\int_{core}\mathbf{e}\times\mathbf{h}^*\cdot\mathbf{z}dA}{\int_{A\infty}\mathbf{e}\times\mathbf{h}^*\cdot\mathbf{z}dA}+n_1^2\frac{\int_{glass}\mathbf{e}\times\mathbf{h}^*\cdot\mathbf{z}dA}{\int_{A\infty}\mathbf{e}\times\mathbf{h}^*\cdot\mathbf{z}dA}\right] \end{aligned} \tag{3.8}$$

n_{eff} is the effective index of the mode and n_1 is the refractive index of the glass as defined in section 3.2.2. By substituting equation (3.6) into Equation (3.8) we then get

$$n_g=\frac{1}{cn_{eff}}\left[1+\eta\left(n_1^2-1\right)\right] \tag{3.9}$$

Substituting the equation (3.9) to equation (3.7) we get

$$D(\lambda)=\frac{\left(n_1^2-1\right)}{cn_{eff}}\frac{d\eta}{d\lambda}-\frac{n_g}{cn_{eff}}\frac{dn_{eff}}{d\lambda} \tag{3.10}$$

The n_{eff}'s relationship with wavelength can be rewritten as

$$\frac{dn_{eff}}{d\lambda}=\frac{\left(n_{eff}-n_g\right)}{\lambda} \tag{3.11}$$

and we get

$$\begin{aligned} D(\lambda) &= \frac{\left(n_1^2-1\right)}{cn_{eff}}\frac{d\eta}{d\lambda}+\frac{n_g}{cn_{eff}}\frac{\left(n_g-n_{eff}\right)}{\lambda} \\ &\approx 3.8\times10^8\times\frac{d\eta}{d\lambda}+3.3\times10^6\times\frac{n_g-n_{eff}}{\lambda}\,(\text{ps/nm/km}) \end{aligned} \tag{3.12}$$

The approximation is got by approximate n_1 and n_{eff} to be 1.45 and 1, respectively. As you can see here, the dispersion of the HCF is related to how the fraction of total power inside the glass change with wavelength. Because the NANF guides light based on antiresonant mechanism, $\eta(\lambda)$ is very small (typically $\approx 10^{-4}$) and does not change significantly with wavelength. This results in a relatively small dispersion in NANF, typically 2-4 ps/km/nm[20], as shown in Figure 3.10.

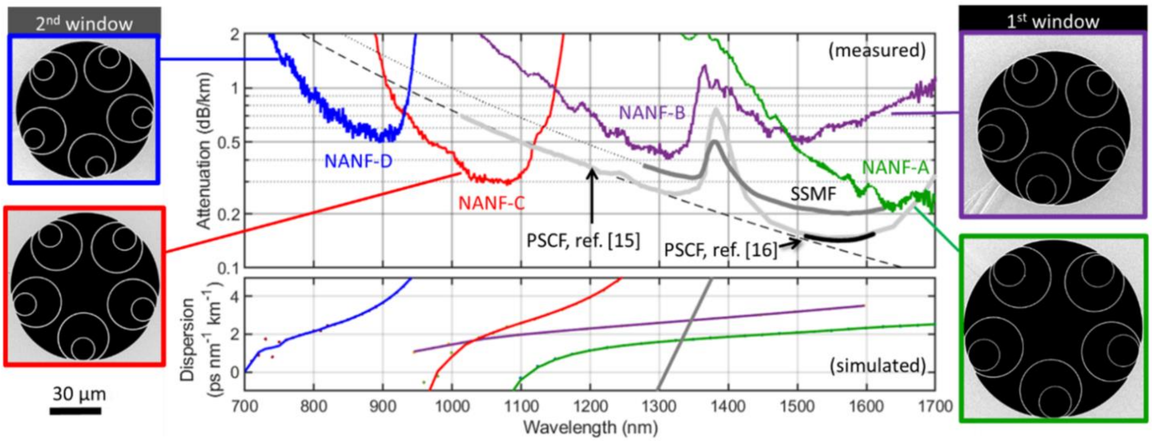

Figure 3.10 The simulated dispersion of the 5 tube NANFs as compared to their loss [20].

3.4.4 Thermal sensitivity

There are several different definitions regarding to the thermal sensitivity which are suitable for different applications. For some applications, especially those based on an interferometer system [55–58], the thermal sensitivity of accumulated optical phase of light through a fibre is crucial. The phase change of light traveling a length L through a mode effective index n_{eff} is

$$\phi = \frac{2\pi}{\lambda} n_{eff} L \tag{3.13}$$

Then the thermal sensitivity S_ϕ is defined as a change in the accumulated phase as a function of temperature in a unit-length optical fibre[59–61],

$$S_\phi = \frac{1}{L}\frac{d\phi}{dT} = \frac{2\pi}{\lambda L}\left(L\frac{dn_{eff}}{dT} + n_{eff}\frac{dL}{dT} \right). \tag{3.14}$$

The first term is due to the thermo-optic effect and the second term is due to effect of fibre elongation. The normalised thermal phase sensitivity (phase change normalized to phase) is sometimes used in literature too:

$$\begin{aligned} D_\phi &= \frac{1}{\phi}\frac{d\phi}{dT} = \frac{1}{n_{eff}}\frac{dn_{eff}}{dT} + \frac{1}{L}\frac{dL}{dT}. \\ &= S_n + S_L \end{aligned} \tag{3.15}$$

Here, S_n indicates the thermo-optic coefficient and S_L indicates the coefficient of thermal expansion (CTE).

In some other applications, e.g., in microwave photonics and time and frequency transfer [62], accurate time and propagation time delay are of interest. The time delay from propagating along a fibre of length L and group index n_g is

$$\tau_g = \frac{n_g L}{c}, \tag{3.16}$$

In these applications, the variation of optical delay with temperature per unit length of fibre is of interest, which is in literature called the thermal coefficient of delay (TCD) [14,60,63,64],

$$TCD = \frac{1}{L}\frac{d\tau_g}{dT} = \frac{1}{cL}\left(L\frac{dn_g}{dT} + n_g\frac{dL}{dT}\right). \tag{3.17}$$

Unlike in (3.14), the first term is due to the effect of the group index n_g (not effective index n_{eff}) change with temperature. However, as in [65], for operating wavelengths where dispersion is relatively small, we may approximate changes of n_g with the changes of the effective index n_{eff} . Normalising the time delay change to time delay, we get

$$\begin{aligned} D_\tau &= \frac{1}{\tau}\frac{d\tau}{dT} \approx \frac{1}{n_{eff}}\frac{dn_{eff}}{dT} + \frac{1}{L}\frac{dL}{dT}, \\ &= S_n + S_L \end{aligned} \tag{3.18}$$

which has the same expression as in(3.15). Then, the thermal phase change to TCD's relationship is

$$TCD = \frac{n_{eff}}{c} D_\phi . \tag{3.19}$$

Note, equations (3.18) and (3.19) are valid only when the chromatic dispersion is relatively small, so its effect could be neglected.

For fused silica, S_n=7.6 ppm/°C while S_L=0.55 ppm/°C [14]. In an HCF, the thermo-optic effect can be neglected because of very small overlap between glass and light, therefore the thermal sensitivity of a HCF should be about 15 times better than a bare SMF when measured by the normalised thermal phase sensitivity and 20 times better when measured by TCD and thermal phase sensitivity S_ϕ. Thermal sensitivity in HCF was firstly studied by Dangui in 2005 [58], which, achieved an improvement by a factor of 3-5x in the normalised phase thermal sensitivity of 7-cell PBGFs. The discrepancy with above-discussed, was attributed to the coating. For a coated HCF, its CTE can be calculated by [88]

$$D_\phi = S_L = \frac{\sum_{i=1}^{N} S_L^i E_i A_i}{\sum_{i=1}^{N} E_i A_i}, \tag{3.20}$$

where S_L^i denotes the CTE of different material, E_i Young's modulus, and A_i the cross-sectional area of the fibre layers. N denotes how many layers an HCF has. For a single-layered fibre, N is 2 (glass and coating) and for a dual-coated fibre, N is 3 (glass, primary coating and secondary coating). The CTE of an HCF is significantly influenced by coating's properties, e.g., Young's modulus, CTE and thickness. Dangui calculated the 7-cell PBGF he used with different coating material and thickness, and found that S_L in his case was 2.57 ppm/°C, which agrees well with his measurement. The lower thermal sensitivity can be achieved by using coating with smaller Young's modulus, CTE and thickness. In 2015, Slavik reported on experiments with a 19-cell PBGF, achieving 18x improvement in terms of the TCD and 13x in terms of normalised phase thermal sensitivity [14].

Since 2015, this topic was intensively studied by our research group, including strategies to further reduce already-small HCFs' thermal sensitivity or to eliminate it. In 2017, Fokoua proposed a method by using PBGF's dispersion redshift effect to reduce the group delay when temperature increased, which was set to compensate the HCF's thermal expansion effect. In this way, zero TCD was achieved at a wavelength with a dispersion of 80 ps/km/nm[63]. Although this method eliminates TCD, it cannot reduce the phase thermal sensitivity. Another method proposed used HCF with open ends. As air escapes the HCF when temperature increases, the thermo-optic coefficient of air inside the HCF becomes negative. This can compensate HCF's thermal expansion effect. Measurements confirmed zero thermal sensitivity for both phase and time delay change at 113 °C. Zhu studied HCF's thermal sensitivity at low temperature, as CTE of silica glass crosses zero around -80 °C and thus the HCF thermal sensitivity is expected to cross zero there. He confirmed this occurring close to -70°C, but this was achieved only for a bare (with coating removed) HCF [61]. As fibre coating becomes stiffer at low temperatures, the coated HCF zero sensitivity point is shifted to even lower temperatures[66]. It was suggested that a thinly-coated HCF could represent a compromise, achieving a fibre that has zero thermal sensitivity temperature reachable within liquid nitrogen temperature range that is (unlike uncoated HCF) not fragile. My colleagues have confirmed this experimentally using HCF with very thin (10 um) coating, but these results have not been published yet. Such thinly-coated HCF was also recently shown to slightly reduces the thermal phase sensitivity at room temperature (to about 0.4 ppm/°C), but also to eliminate the phase relaxation effect due to coating's viscoelastic property[89]. This makes thinly-coated HCF a promising candidate for all experiments in which thermal sensitivity is of importance.

3.4.5 Nonlinear effects

The fact that the overlap of light and glass material is very small in HCFs also leads to low nonlinear effect. The nonlinear refractive index n_2 of different components of air was measured about 8×10⁻

^{24} m^2/W [90], which is about three orders of magnitude lower than that of fused silica (2.47×10^{-20} m^2/W) [91]. The Brillouin scattering in ARFs were found to be at least three (five if evacuated) orders of magnitude weaker than those in SMFs [92]. Other nonlinear effects, like stimulated Raman scattering (SRS) and thermal lens effect, were also found orders of magnitude weaker than in SMF [2].

3.5 HCF to SMF interconnection

Many applications of HCFs require their interconnection to the SMF to be used in the current SMF system. A typical configuration of SMF-HCF-SMF interconnection is shown in Figure 3.11. The HCF is spliced to SMF at both ends.

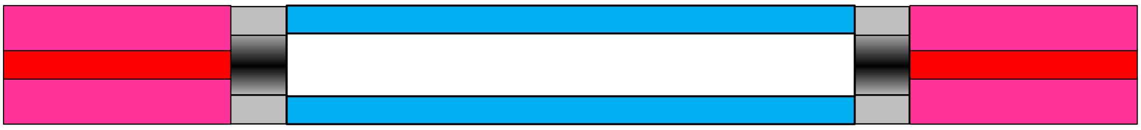

Figure 3.11 The typical configuration of SMF-HCF-SMF. MA: mode adapter.

There are several issues needing to be cared when splicing HCF to SMF. Mode field diameter (MFD) of the lowest-loss NANFs and ARFs [18–20] ranges from 20 to 30 μm, while SMF's MFD is typically 10 μm. For low-loss interconnection, this requires MFD adaption, which is typically achieved by a mode adapter (MA). Besides, the HCF-SMF connection has a glass-air interface at the connection point, which causes loss via Fresnel reflection of 3.5% and Fabry-Perot effect between the two splice points as shown in Figure 3.11. This can be solved by anti-reflection coating (AR) at the endface of MA or by angle cleaving the MA. Additionally, the exposed HCF is susceptible to mechanical damage or a humidity [26] so that sealed splice is expected. Thus, a good interconnection needs to require: 1. Low insertion loss (IL) which is defined as the transmission loss including both splice points as shown in Figure 3.11; 2. Low return loss (RL) which is defined as the ratio of returned optical power and input optical power at the splice point described in dB and 3. being permanent and hermetic. We will briefly talk about several splice technologies including fusion splicing and mechanical splicing and their application in interconnection of SMF-HCF here.

3.5.1 Fusion splicing

A common method to achieve a permanent interconnection of two optical fibres is fusion splicing. This is typically done by fusing or welding two fibre ends usually by an electric arc and then pressing them together to form a permanent, robust, repeatable and low-loss interconnection. For HCF, one main problem is that the delicate microstructure of HCF is easily collapsed if overheated [93,94].

The main modification to splice HCF is using an offset heating (by arc, filament or CO_2 laser) so that the solid core fibre is heated more than the HCF.

The first report about splicing the HCF to SMF occurred at 2005 in [94], where the collapse effect was also studied. In the same year, the fusion splice technology was used to make HCF based gas cells in [95], where the IL of the SMF-7-cell PBGF-SMF and a 7-cell PBGF was 3.6 dB. Then a detailed study was carried out at 2006 [96]. The paper reported the fusion splice of a SMF with a MFD of 10.4 μm to a 7-cell PBGF with a MFD of 7.5 μm and a 19-cell PBGF with a MFD of 13 μm respectively. Different transmission loss from SMF to HCF and from HCF to SMF was found. For the 7-cell PBGF, the transmission loss from SMF to PBGF was 1.5-2.0 dB while from PBGF to SMF it was 2.6-3.0 dB. In the case of 19-cell PBGF, the splice loss from SMF to PBGF varied from 0.3 dB to 0.5 dB whereas it was more than 2 dB in the opposite direction. This unbalanced result of SMF-HCF and HCF-SMF transmission loss is due to HOM excitation in the used HCFs. As the coupling into the fundamental mode is usually of interest [97], it is important to measure how much power is coupled into the fundamental mode only. Several possible methods can be used, including using long enough length of NANF (as HOM has higher attenuation than the fundamental mode), using techniques that decouple modes at the fibre output (such as S^2 [18]), or connecting SMF at both ends of the HCF and measuring connection loss with a broadband light source.

To suppress the unwanted excited HOMs inside the HCF and further improve the IL, matching the MFD at the input end of HCF is needed. In 2010, by choosing an SMF with similar MFD to a 7-cell PBGF, the splice loss for SMF-PBGF was reduced to 0.79 dB [98]. Matching MFD is especially important for ARFs, as the MFD of ARFs are typically over 20 μm. In 2021, by using a two-step reverse-tapering process, the researchers could expand the SMF's MFD to 21.4 μm, which is very close to the MFD of the ARF they used (24.4 μm), which makes their total IL of SMF-HCF-SMF interconnection only 0.88 dB [99]. Also recently, by using a large mode area (LMA) fibre, a transmission loss from the LMA fibre to the ARF was improved to 0.4 dB[100].

Efforts was also made to reduce the unwanted back-reflection from the glass-air interface. For fusion splice technology, a common method is to use angle-cleaved splices. By cleaving SMF with an angle of 8^o, the reflected light does not couple back into the guided mode and leaks out through the cladding to the outside. In 2007, splicing of flat and angle-cleaved 7-cell PBGFs was presented [101], with a transmission loss of SMF-PBGF connection of 0.9 dB and 3.0 dB, respectively for flat and angle-cleaved PBGFs. In 2016, splicing of 7-cell and 19-cell AC-PBGFs resulted in slightly lower RL of −50 dB [102] and the angle cleaving brought an additional splice loss of 1–2 dB.

3.5.2 Mechanical splice

Mechanical splices are used to create permanent joints between two fibres by holding the fibres in an alignment fixture and reducing loss and reflectance with a transparent gel between the fibres that matches the optical properties of the glass. This technique was used with SMF as well before the invention of HCF. Compared to fusion splice, this technique is truly cold splice so it enables no damage at the HCF end, which not only avoids the collapse of microstructure of HCFs but also provides a method to splice HCF with an AR coated fibre.

The initial attempt to use mechanical splice to connect SMF came with the fabrication of HCF based gas cells. In 2008, a 19-cell PBGF was mechanically spliced to a SMF at one end and a multi-mode fibre (MMF) at another end [103]. A 20 mm gap was intentionally kept between the fibres to let gas in and the total IL of the SMF-PBGF-MMF interconnection was measured to be 1.2-2.0 dB in the wavelength range of 1530-1610 nm. In 2013, a 7-cell PBGF was connected to the SMF and MMF via FC-APC connector [104]. In this design, the solid core fibres were cleaved with an 8^{o} to prevent the back reflection while HCF's angle was kept flat. The total IL for SMF-PBGF-SMF and SMF-PBGF-MMF were 21.8 dB and 10.8 dB respectively. The large ILs were possibly due to the large gap (175 μm) between the SCFs and HCF. At the same year, a large-core Kagome HCF and angle cleaved SMF were connected by using borosilicate capillary sleeves. Both tapered and not tapered HCF were spliced with SMF[105]. The transmission loss for SMF-HCF connection was 4.5 dB for tapered HCF while 2.8 dB for not tapered HCF. The RL was -59 dB and -43 dB, respectively. All of these splices were made for gas cell so that a small gap between HCF and solid core fibre has to be kept, which increases the IL. The first mechanical splice of SMF and HCF which provides low IL and long-term reliability was reported at 2014 [106]. By using FC/PC connectors, a 19-cell HCF was spliced to an LMA fibre with a transmission loss from LMA to HCF of -1.05 dB. A RL of -31 dB was also obtained due to a deposited AR coating on the LMA fibre.

3.5.3 Gluing splice

In 2019, our colleagues from the Czech Technical University in Prague developed a splice technology based on fibre-array technology and the interconnection is achieved by gluing HCF and SMF together [107]., The details of this technology are shown in Figure 3.12. A piece of Graded Index (GRIN) fibre was spliced to the SMF and then polished to an optimised length to convert SMF's MFD to the size of HCF and put into a fibre array. An AR coating was deposited to the end of GRIN fibre. Then a cleaved HCF was put into another fibre array. Followed by a carefully 5-axis adjustment of two fibre arrays, they are glued together to achieve a permanent and sealed connection. The technique was first developed in 2019 with a 19-cell PBGF. The IL of SMF-PBGF-SMF interconnection was measured to be only 0.87 dB with a RL as low as -30 dB. In 2021, the same group applied their technology to the latest NANF, which enables them to get a record low transmission loss for SMF-NANF connection of 0.32 dB and a RL below -40 dB over a 60 nm bandwidth [97]. In the same paper, instead of using a piece of GRIN fibre, they also tried thermally-expanded core fibres (TECs) as an MA, leading to transmission loss for SMF-NANF connection of 0.42 dB. Besides, the reliability of fibre array based splice technology was also tested recently [108]. The IL only changed by 0.02 dB when temperature changes from 25 °C to 85 °C and it fluctuated below 0.02 dB during 100 days is also below 0.02 dB.

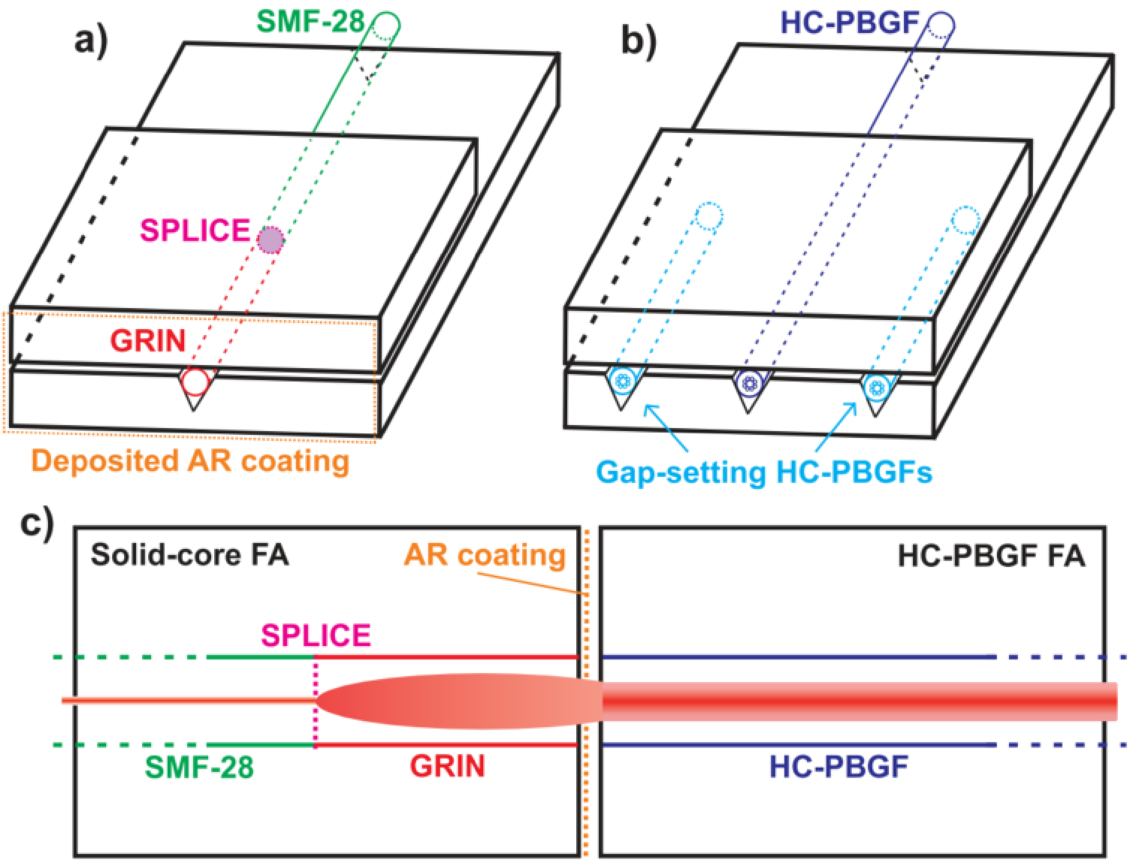

Figure 3.12 Illustration of the developed SSMF-PBGF splice technology by using fibre array. The graded index fibre (GRIN) serves as a MA between SSMF and PBGF. This picture is adopted from [107].

3.5.4 Other splice technologies

An interesting solution was published using micro-optic collimator technology [109], where a transmission loss of 0.53 dB was presented for SMF-HCF interconnection with RL better than −45 dB. This technique also enables realization of various compact micro-optic based components, i.e., optical isolators and beam splitters for HCFs [110,111].

Many applications require a determined state of polarisation inside the HCF, which leads to the need of polarisation maintaining fibre (PMF) to HCF splice. In 2008, a 7-cell PBGF was fusion spliced to a PMF with splice loss for PMF-HCF connection ranging from 0.31 dB to 0.77 dB while a successful polarisation extinction ratio (PER) varying in the range of 17.3-19.7 dB[112]. In 2021, a tubular ARF was spliced to PMF at both ends[113]. The PER was measured no less than 10 dB over1400 nm-2100 nm.

Regarding HCF to HCF interconnection, an interconnection has already been demonstrated via fusion splicing with only 0.16 dB average splice loss [114]. 1.28 dB loss was also achieved with micro-optic collimator [109].

3.6 Application of hollow core fibres

Due to the unique properties provided by HCFs as we described in section 3.4, they are used in many applications. In this section, I review several of the most promising/important applications, highlighting the key attractions/benefits of HCFs, progress to date and future prospects.

3.6.1 Gas photonics

One significant difference between HCFs and conventional SMFs is their void in core, which gives possibility to fill gases into the fibre to make gas cells for different applications. Many applications benefit from long interaction length between light and gases. To achieve long interaction length in a bulky gas cell, the long length is typically achieved by multiple beam reflection, i.e., White and Herriott designs, which is, however, limited to several tens' metres [115], and it is difficult to align and maintain. HCFs provide a practical and easy alternative to achieve long-path gas cells, which is the key concept behind the rising of so-called "gas photonics"[116] .

One of HCF gas cells applications is nonlinear gas optics. Compared to solid materials, gases not only provide higher threshold for laser power but also provide better tunability of nonlinearity and dispersion by controlling the pressure and mixtures of gases. The first landmark results in nonlinear gas-based fibre optics using an PBGF platform were reported by Benabid in 2002 [117] who demonstrated Raman scattering threshold energies that were two orders of magnitude lower than in previous geometries by using a 1 m length of PBGF filled with hydrogen to a pressure of 17 Bar. This result kick-started the field of gas-based nonlinear fibre optics and since then a large body of works have been performed in the area, including supercontinuum generation[118], electromagnetically induced transparency[119], laser generation based on Stimulated Raman Scattering (SRS)[120] and Stimulated Brillouin Scattering (SBS) [16]. One successful application is ultraviolet (UV) supercontinuum generation in HCFs. The conventional SMFs suffer from limited optical transparency and cumulative optical damage when delivering UV light, which leads to absence of SMFs based vacuum-UV (~100-200 nm) and deep-UV (~200-300 nm) supercontinuum source. Benefiting from HCFs' properties, Belli demonstrate a bright supercontinuum spanning more than three octaves from 124 nm to beyond 1200 nm, in hydrogen filled kagomé-style hollow-core photonic crystal fibre[118]. Another very important result in the recent years is the achievement of intensive SBS gain in gas filled HCFs. Although SBS gain in air-filled HCFs was demonstrated to be three orders of magnitude lower than that in SMFs [79], Yang has found that the SBS gain of gas increases quadratically with the pressure in the ideal gas approximation, which enables demonstration of an SBS gain 6 times higher than that in convetional SMFs with a CO_2 HCF gas cell with a gas pressure of 41 Bar.

When HCFs are filled with different gases as active medium, they can also serve as gain media used in the rising 'Hollow-core Optical Fibre Gas Lasers' (HOFGLASs) [2]. Typically, the population inversion was achieved by optical pumping at an absorption band of a gas. As different gases provide different absorption wavelength and emission wavelength, this new-class of 'hybrid' fibre-gas lasers holds the potential to generate diffraction limited beams in wavelength regions beyond the fundamental limitations of rare-earth doped solid core fibre lasers. Solid core fibre lasers typically operate in the 1 µm to 2 µm wavelength region. As shown in Figure 3.13, the emission regions are determined by the active ions, for example Yb, Er, Pr, Tm, with which the silica core is doped[121]. By doping Er3+ (2.8 µm, 3 µm, 3.45 µm), Dy3+ (2.9 µm), Ho3+(3.9 µm) in fluorozirconate hosts, lasing between 2 µm and 4 µm has been demonstrated. HOFGLASs can cover additional emission regions depending on the active gas used, Figure 3.13. Laser operation further into the infrared region(IR) utilizes rotation-vibration transitions in molecular gases, e.g., HBr, CO, CO_2[122–124]. Emission in the visible and UV typically relies on electronic transitions. Examples are dimer lasers [125] and I_2 [126,127] lasers. Besides the population inversion, other gain mechanisms include SRS[120] and SBS[16] just demonstrated recently, further increasing the tunability of wavelength range of HOFGLASs.

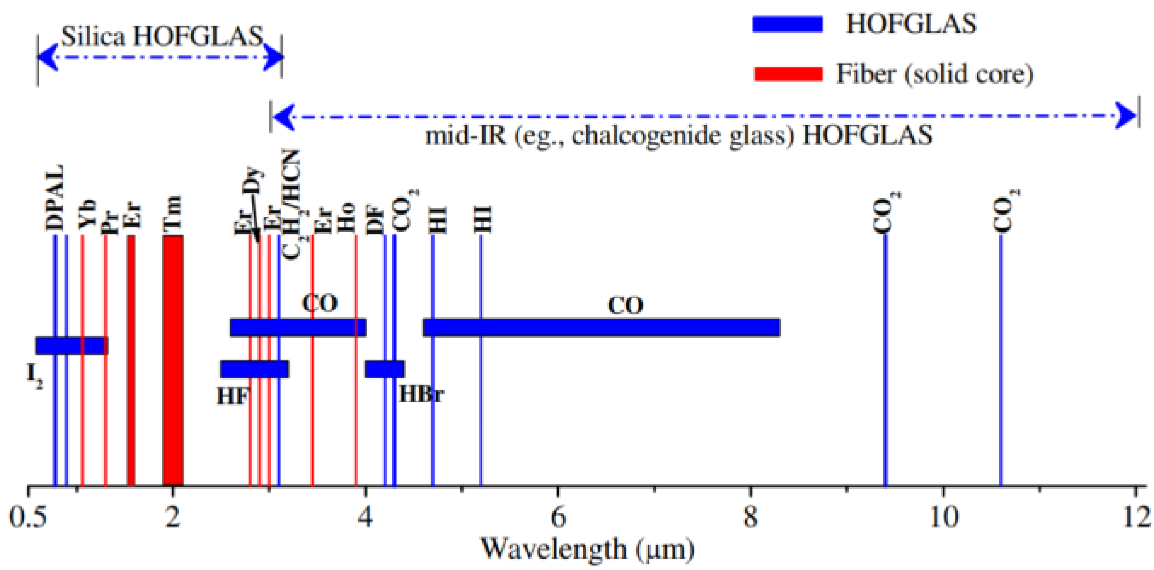

Figure 3.13 Examples of laser emission from typical solid core fibre lasers with silica and fluorozirconate hosts, and possible emission wavelengths in gases. The latter can principally be used in HOFGLAS with already available silica based HCFs and TeAsSe (TAS) chalcogenide glass fibres. The horizontal bars indicate many individual narrow lines. Figure adopted from [128].

Since the sensitivity of the majority of laser-based gas sensors can be relatively simply and significantly enhanced by increasing the interaction path length, access to non-complex and long optical paths is highly desired so that HCF gas cell based gas sensors represent a very straightforward idea, discussed in literature since the invention of HCFs. The first spectroscopy measurements in PBGFs date back to 2004 when experiments on acetylene were reported using a simple intensity-based measurement approach [84]. Since then numerous papers on the use of similar and more advanced spectroscopy techniques (e.g., wavelength modulation spectroscopy (WMS)[129], tunable diode laser absorption spectroscopy (TDLAS)[130], cavity ringdown spectroscopy (CRDS) [8], photothermal spectroscopy (PTS)[131,132] and sub-Doppler spectroscopy[133]) on an increasingly diverse range of gases (including C_2H_2[131], CO_2 [134] and CH_4 [135]) are to be found in the literature with reasonably impressive sensitivities claimed (e.g., parts-per-trillion for C_2H_2 in [132]). One problem for these HCF gas sensors is long gas filling time. Due to HCFs' small core, it often takes gases long time to fill the hollow-core. For example, to fill CH_4 into a 5.1 m-long HCF, it took 7 minutes in [135]. Drilling side-holes along HCFs is a possible way to reduce the filling time thus improving the sensor's response time, however, at the expense of fibre loss (0.07 dB/side hole in [136] and 0.01 dB/side hole in [137]). Besides, multi side-holes also reduce the HCF's mechanical strength. HCF based Fabry-Perot perhaps provide an alternative idea to solve this problem. By putting a short HCF into a high-finesse cavity, the interaction length could be enhanced by several orders times depends on the finesse, which may provide a good sensitivity and short filling time at the same time [9,10,138]. Up to now, a cavity finesse of 700 cavity have been demonstrated to enhance the interaction in photothermal spectroscopy for CH_4 and C_2H_2, achieving a noise-equivalent concentration as low as 2.7 parts-per-trillion.

One more but not the last applications for HCF based gas cells is frequency reference in optical metrology. Based on Lamb-Beer law, the sensitivity of gas sensors based on intensity-based measurement approach is improved with high absorption strength, which requires the detection laser is locked to the absorption dip of measured gases. HCF gas cells provide a compact, robust choice for these applications. Especially, a CO_2 gas cell made from HCF has been demonstrated recently no change of observed absorption spectrum over 3 years, making this technique more promising for the future [139,140].

Besides being used as gas cells, the filling gas was also found to structure HCFs, providing an extra method to tailor and enhance the optical performance of HCFs. For example, one recent study shows that by filling gas with higher pressure in the core area of a 7-tube ARF, a small refractive index change can be obtained in the core and cladding regions of the ARF, leading to a 5 times reduction of the confinement loss of this fibre [141].

3.6.2 Optical fibre sensing

The gas sensing based on HCFs have been discussed in the last section; however, other sensing applications based on HCFs have also been broadly investigated in the recent years. One typical application is based on the Fabry-Perot structure in which a short section HCF is spliced to flat cleaved SMF at its both ends[142,143]. As HCFs provide less thermal sensitivity as compared to SMFs [143], and can in principle be fabricated to be more sensitive to strain[144], curvature[145], external pressure[146,147], these HCF based sensors provide much less strain (pressure)-temperature cross sensitivity. By drilling holes at the wall of HCFs, the sensitivity of pressure can be even enhanced [148,149] and HCF-FPs can also be used to measure liquid's properties, e.g., liquid level [150], refractive index[151] and salinity [152]. Typical HCF-FPs are formed by just splicing two SMFs with HCFs. However, due to the MFD difference between SSMFs and HCFs, these HCF-FPs have only limited fringe visibility (below 5 dB when FP's length is over 250 μm). By splicing a ¼ pitch graded index fibre (GRIN) as a mode adapter, a fringe visibility of 13 dB could be obtained with a FP length of 500 μm thus leading to a higher sensitivity when used as a sensor [153]. The HCF-FP based sensor could also be improved by utilising an FP with high finesse, as the higher finesse provides narrow peaks thus better capability of frequency discrimination.

Other successful all fibre sensors include the fibre optic gyroscope (FOG) based on the Sagnac interferometer and HCFs have been demonstrated to improve performance in FOGs [154–156] .

Critical to this application, in addition to a low thermal sensitivity, is the low Rayleigh backscattering and low optical nonlinearity since these effects can otherwise deteriorate the phase error. Excellent single mode, polarisation maintaining performance of the fibre are also essential requirements in FOGs. ARFs especially NANFs, offer great benefits on all of these fronts. A recent work on a 6-tube NANF with effectively single mode behaviour and less polarisation mode coupling than SSMF, have demonstrated a long-term bias stability about 0.05 deg/h for observation times of 1–10 h, within about 10× the requirement for civil aircraft navigation usage, looking very promising for these applications [154].

Several sensor applications, particularly those associated with space borne missions or with use in nuclear plant/waste management, require long-term operation of fibres in high radiation environments. However, the SMF suffers radiation induced attenuation (RIA) in space, resulting in the decay of light power in the SMF[157]. Again, due to the fact that HCFs guide light in air/vacuum, HCFs are not prone to radiation damage, making them also attractive in these radiation-exposed applications [158].

3.6.3 Microwave photonics

Microwave photonics uses optical devices and techniques for advanced processing and transport of radio frequency (RF) signals. Although integrated microwave photonics is compelling due to advantages such as small size and compactness, optical fibres still play a key role due to their ultralow loss (particularly relevant for long distances). One of the key microwave photonics requirements is to be able to set a controllable delay of the signal being processed. Defining a fixed delay is straightforwardly realized with minimum loss or signal distortion via signal propagation through a length of an optical fibre, that is so-called optical delay line. For stable operation of microwave photonics filters (MPFs) and other related devices such as optoelectronics oscillators (OEOs), the delay introduced by a delay line should be stable with temperature. Even when using optical fibres for transport of the microwave signal (such as clock distribution [159], 5G networks [160], or radio astronomy [161]), changes in the RF signal phase due to temperature are of importance. The RF signal phase is given by

$$\phi_{RF} = \omega \tau_g , \tag{3.21}$$

where ω is the angular frequency of the RF phase signal and τ_g is the time delay given by a fibre, determined by equation (2.14). Although SMF based delay lines have demonstrated a great improvement compared to coaxal cable, they are still not enough in many applications. Several different techniques have been explored to improve delay lines thermal stability. To compare their thermal stability, we normalise the RF signal phase thermal change to the total RF signal phase,

$$S_{\phi_{RF}} = \frac{1}{\phi_{RF}} \frac{d\phi_{RF}}{dT} . \tag{3.22}$$

The thermal sensitivity of SMF based delay lines is around 8 ppm/K. One approach to improve this is to coat SMFs by a material with negative CTE, which is known as phase stable optical fibre (PSOF) [162–164], reducing the thermal sensitivity to 1-2.2 ppm/°C. Another approach is to use HCFs. As we discussed before, HCFs offer one order of magnitude improvement in terms of thermal sensitivity compared to SMF. This advantage has already been demonstrated in microwave photonics, resulting in the demonstration of an optoelectronics oscillator (OEO) with 16 times smaller sensitivity of the oscillating frequency to temperature as compared to an OEO made with SMFs [47]. By using the carefully-designed PBGF which has a TCD close to 0 ps/km/K [63], an OEO with >100 times better thermal stability than SMF has been reported [165]. Besides lower TCD, HCFs have other advantages over SMFs relevant for microwave photonics, e.g., low nonlinearity in combination with low chromatic dispersion, which makes them more promising as delay lines used in microwave photonics.

3.7 Summary

In summary, hollow core fibres, especially the nested antiresonant fibres, have seen steadily progress in these years in terms of fibre attenuation. The low attenuation has enabled achievement of high-finesse hollow core fibre based Fabry-Perot interferometers. We then introduced hollow core fibres properties, e.g., low dispersion, low thermal sensitivity and low nonlinear effect in section 3.4 to show advantages of hollow core fibres utilisation in a high finesse Fabry-Perot interferometer. We also introduced hollow core fibre-single mode fibre interconnection in this chapter as it is the key technology to realize all fibred hollow core fibre based Fabry-Perot interferometers as we will present in Chapter 6. In the last section, we reviewed some applications of hollow core fibre based applications. These applications showed advantages of hollow core fibres, which also showed prospects of high-finesse hollow core fibre based Fabry-Perot interferometers.

Chapter 4 Characterisation of long-length Fabry-Perot interferometers

As we are targeting to make long-length HCF-FP, their FSRs are smaller than the best resolution (~ 0.01 nm) of our optical spectrum analyser (OSA, Ando AQ6371B). The optical scanning method which is often-used for long-length FP characterization requires a laser with a very narrow linewidth when dealing with high-finesse and long length FP. Both of them are impractical in our case. In this chapter, we will introduce the principle of our proposed method to characterize long-length FP.

4.1 Setup of measurement and its analysis

The setup to measure a long-length FP is shown in Figure 4.1. An incoherent tunable optical source is built by using two cascaded erbium doped fibre amplifiers (EDFAs) with a tunable bandpass photonics optical filter (TBPF, Alnair Labs BVF-200) inserted. The amplified spontaneous emission (ASE) from EDFA1 is used as broadband incoherent light source while EDFA2 is used to amplify power of the spectrally-narrow ASE slice selected with the TBPF. The wavelength and bandwidth of the TBPF can be both tuned within 1530-1570 nm and 0.1-10 nm, respectively. Subsequently the light is launched into a FPI under test. The transmitted light forms an incoherent frequency comb with spacing corresponding to the FSR of the FP, which is then detected by a photodiode (Discovery Semiconductor, DSC30S). Detection of the comb generates multiple heterodyne beating signals and they are measured with an RF spectrum analyser (Agilent, E4446A). The RF spectrum analyser is connected to a computer, which enables us to read and process the signal by a LabVIEW program.

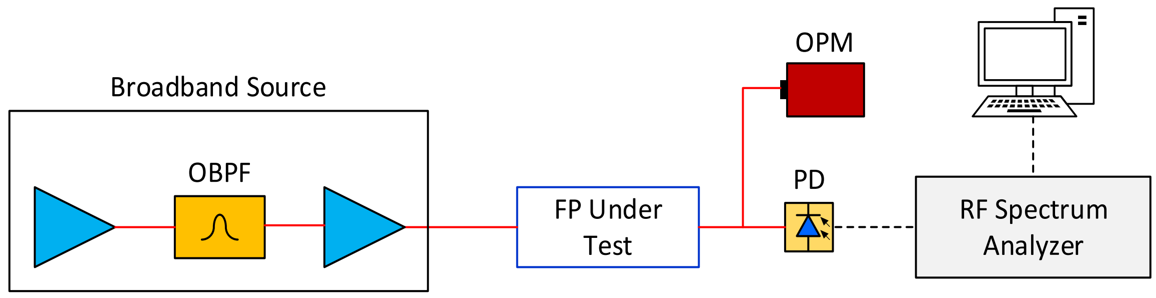

Figure 4.1 FP characterization set-up. The broadband light source: Two cascaded Erbium-doped fibre amplifiers (EDFAs) passed through a 10-nm tunable bandpass photonics optical (TBPF). PD: photodetector. OPM: optical power meter.

4.2 Characterisation of finesse and FSR

RF signal obtained with the RF spectrum analyser is analysed as follows. The complex amplitude density of light at the output end of the FP under test is given by

$$S_I(v) = t(v)S_0(v) \tag{4.1}$$

where $S_0(v)$ denotes the complex amplitude density of light out of the broadband source and $t(v)$ the transmission coefficient of the FP. The signal in the time domain E(t) is the Fourier transform of the signal expressed in Equation (4.1).

$$E(\mathrm{t}) = \int t(v)S_0(v)e^{-j2\pi vt}dv \tag{4.2}$$

The PD transforms the optical signal into an electrical signal (a photocurrent) which is converted to a voltage signal via by a 50 Ω load of the RF spectrum analyser. The voltage signal is

$$u(\mathrm{t}) \propto \gamma P(\mathrm{t}) \propto \gamma E(\mathrm{t})E^*(\mathrm{t}) \tag{4.3}$$

Here, P(t) indicates power of the optical signal and γ is the responsivity of the PD. RF spectrum analyser signal is mathematically obtained as Fast Fourier transform of the time domain signal and the averaging signal showing on the RF spectrum analyser is

$$\mathrm{e}(f) = \left\langle \int u(\mathrm{t})\,\mathrm{e}^{-j2\pi ft}\,dt \right\rangle = \left\langle \int t(v)S(v)t^*(f-v)S^*(f-v)dv \right\rangle \tag{4.4}$$

Thus, the frequency domain signal looks as a broadband signal modulated by the FP transmission function. In the RF frequency domain, the spectrum of the broadband ASE signal can be treated as a constant. The above equation can be then written as

$$\begin{aligned} \mathrm{e}(f) &\propto \left\langle \int t(v)S(v)t^*(f-v)S^*(f-v)dv \right\rangle \\ &\approx \int t(v)t^*(f-v)dv \cdot \left\langle \int S(v)S^*(f-v)dv \right\rangle \\ &\propto \int t(v)t^*(f-v)dv \end{aligned} \tag{4.5}$$

By substituting an FP's transmission coefficient, we can further get

$$\begin{aligned} \mathrm{e}_n(f) &= \int t(v)t^*(f-v)dv \\ &\propto \frac{1}{e^{i\frac{\pi f}{FSR}} - R^2 e^{-i\frac{\pi f}{FSR}}} \end{aligned}, \tag{4.6}$$

which is the self-convolution of the FP's transmission coefficient. The details of this derivation can be found in Appendix A. The RF spectrum analyser only gives the magnitude signal of a Fourier transform, which is

$$\left|\mathrm{e}_n(f)\right| \propto \frac{1}{\sqrt{1+\left(\frac{2F_e}{\pi}\right)^2 \sin^2\left(\frac{\pi f}{FSR}\right)}} \approx \frac{1}{\sqrt{1+\left(\frac{F}{\pi}\right)^2 \sin^2\left(\frac{\pi f}{FSR}\right)}} \tag{4.7}$$

The approximation can be used when R is large enough to use the first order Taylor expansion, which is the case of a high-finesse FP. Here,

$$F_e = \frac{\pi R}{1-R^2}. \tag{4.8}$$

The parameter F_e is defined here to keep the form of the RF spectrum same as FP optical spectrum as shown in (2.12). Compared with finesse $F = \pi\sqrt{R}/(1-R)$ of an FP (equation (2.9)), it has a similar expression. The difference is that here we use R^2 instead of reflectivity R. When R is close to unity, $F_e \approx F/2$. When we set the RF spectrum analyser to display RF power, the signal is then:

$$P(f) \propto \left|\mathrm{e}_n(f)\right|^2 = \frac{1}{1+\left(\frac{2F_e}{\pi}\right)^2 \sin^2\left(\frac{\pi f}{FSR}\right)} \approx \frac{1}{1+\left(\frac{F}{\pi}\right)^2 \sin^2\left(\frac{\pi f}{FSR}\right)} \tag{4.9}$$

From the above analysis, we can deduce some basic facts about our method to characterize an FP.

1. The RF transmission spectrum is self-convolution of FP optical transmission spectrum. The key difference is that the RF spectrum shows peaks that have FWHM twice larger.
2. There are many peaks showing on the RF spectrum analyser, each peak corresponds to N times of FSR. When measuring the signal at high RF frequency, the method is very sensitive to FSR change. For example, for an FP with an FSR of 10 MHz, if we measure the signal at 10 GHz and if FSR changes, the peak shift around 10 GHz changes 1 000 times of the FSR change. When dealing with high-finesse (e.g., >1000) FPs, as we are using an incoherent source, the chromatic dispersion broadens the peak width. The higher RF frequency we are measuring, the broader will the peak width be. This will reduce the measured finesse. Thus, care must be taken to avoid measurement error due to the HCF chromatic dispersion in the future fabrication of HCF-FPs. In such a case, we measure the signal at low RF frequency (several hundreds of MHz) and using a small bandwidth of OBPF (down to 0.2 nm).
3. By fitting RF transmission spectrum using Equation (4.7) or Equation (4.9) in LabVIEW, we can obtain key FP parameters such as finesse and FSR.

There must be noted that the above analysis neglects the chromatic dispersion in an FP. When dealing with very high finesse which has very narrow transmission peaks, it's better to measure the signal at low RF frequency to avoid dispersion's effects.

To validate our theoretical analysis, we built several SMF-FP with lengths ranging from 2.5 cm to 8 cm. The SMF-FP was built by connecting a piece of FC/PC-connectorized SMF with two high-reflectivity coated fibre connectors. Subsequently, we characterized them with the optical spectrum analyser (OSA) (spectral resolution of 0.01 nm) and the RF spectrum analyser. Figure 4.3 shows the results for a 4-cm long FP. The FSR extracted from the OSA trace (Figure 4.3(a)) is 0.02 nm, corresponding to 2.65 GHz at 1530 nm. This is in excellent agreement with the result from the RF measurement (Figure 4.3 (b)), which gives 2.658 GHz. The measured RF spectrum is fitted using Equ.(4.9), which gives very good fit, Figure 4.3 (b). Extracting the finesse from this fit gives a value of F=15.4 and a mirror' effective reflectivity of 81.6%, which is in excellent agreement with the actual mirror reflectivity of 82%. Given the excellent agreement between the data obtained with the OSA and extracted from the RF spectrum with that expected from calculations, we can conclude that our method based on the analysis of the RF spectrum is reliable and accurate.

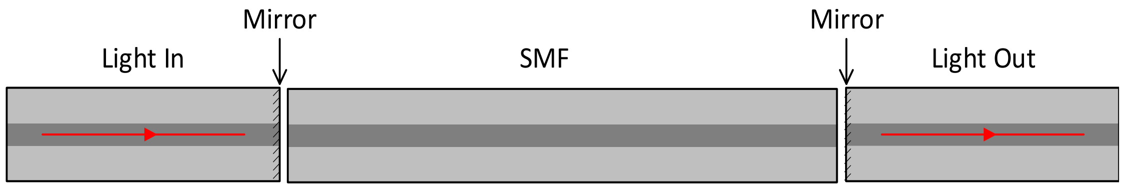

Figure 4.2 The schematic of the SMF-FP used to demonstrate our FP characterisation method. It is formed by jointing a piece of SMF with other two lead SMFs at both ends. The ends of the lead SMF are coated with 4-layer dielectric mirrors, which provides reflectivity of 82% over the 1530-1570 nm wavelength range, serving as mirrors in the FP.

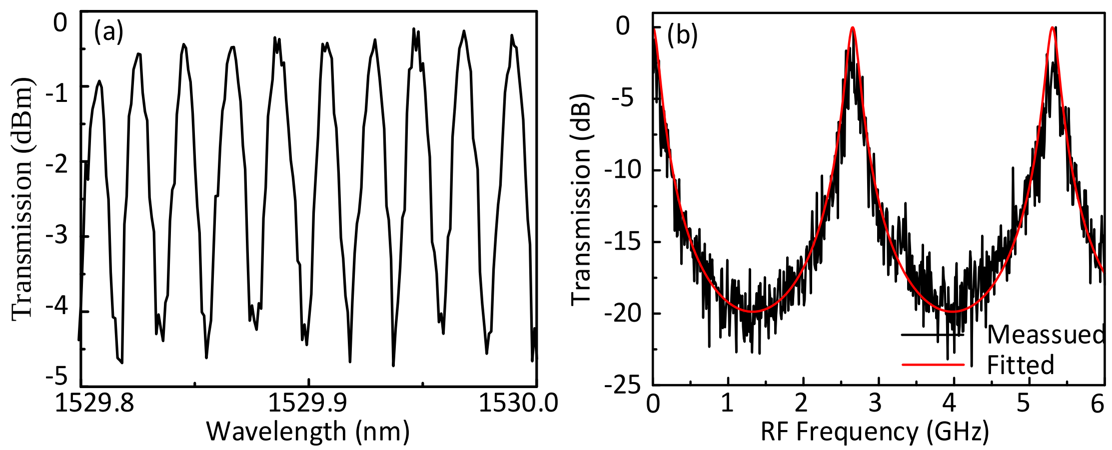

Figure 4.3 The transmitted spectra of a 4-cm long SMF-FP. (a) Optical spectrum measured by an OSA; (b) RF spectrum on the RF spectrum analyser. The normalised data (black line) is fitted using Equation (4.9) (red line).

4.3 Evaluation of insertion loss

By comparing the difference of optical power P_{diff} before and after the FP under test, we can estimate the insertion loss of an FP. The principle is that the total power loss P_{diff} is proportional to the integration of FP filtering characteristics (given by Equation (2.12)) and insertion loss. To enable straightforward experimental evaluation, we derived the following equation, which only requires measurement of the difference of the total optical power before and after the FP in the set-up in Figure 4.1 (P_{diff}), and finesse and FSR obtained in the previous section:

$$\mathrm{IL} = 10 \cdot \log_{10}\left[\int_0^{FSR} \frac{1}{1+\left(\frac{2F}{\pi}\right)^2 \sin^2\left(\frac{\pi v}{FSR}\right)} dv\right] - P_{diff} \tag{4.10}$$

4.4 Summary

In summary, we proposed a method to characterise a long-length FP by utilising an incoherent broadband source and an RF spectrum analyser. The finesse and FSR of an FP can be analysed by the beating signal on the RF spectrum analyser, enabling quick feedback during fabrication of the future hollow core fibre based Fabry Perot interferometers (HCF-FPs). The insertion loss of the FP then can be estimated by the optical power difference before and after the FP with knowing the finesse. We then will use the method to characterise the HCF-FP during and after making them.

Chapter 5 Finesse limits in HCF-FP

Although there are several reports on HCF-FPs, all of them were made without active alignment of the cavity mirrors, as mentioned in section 2.3.4. Thus, the ultimate performance of an HCF-FP, i.e., how much finesse we can obtain is still to be analysed. In this chapter, we will present our theoretical analysis and experimental results exploring the performance limits of HCF-FPs.

5.1 HCF-FP structure and its theoretical analysis

5.1.1 HCF-FP structure

The basic structure of an HCF-FP that I have chosen to study is shown in Figure 5.1. Two mirrors are put close to the HCF ends. In an ideal case, i.e., when the HCF is straight-cleaved and mirrors just touch the HCF ends without angle misalignment, light existing the HCF and reflected back from the mirrors can be all coupled back into the HCF. In practice, part of this light is lost. We define coupling efficiency as a parameter to measure how much light is coupled back, it can be calculated by

$$\varepsilon = \frac{\left|\iint E_r E_0^* r dr d\theta\right|^2}{\iint |E_r|^2\, r dr d\theta \iint |E_0|^2\, r dr d\theta}, \tag{5.1}$$

where E_0 is the transverse electric field at the HCF end facet and E_r is the reflected field when E_0 emerges from the HCF, is reflected from the mirror, and reaches the HCF end facet. The limited coupling efficiency reduces the light reflected from the mirror coupled back into the HCF. We define the "effective reflectivity" of the FP mirror as

$$R_e = \varepsilon R\,. \tag{5.2}$$

In this case, the reflectivity in (2.9) needs to be replaced by the effective reflectivity here to obtain the finesse,

$$F = \frac{\pi\sqrt{R_e G}}{1 - R_e G}\,. \tag{5.3}$$

G defines the fibre loss as described in Equation (2.5). Once the mirror's reflectivity and fibre loss are fixed, the achievable finesse is limited by coupling efficiency. There are several factors that influence the coupling efficiency, i.e., fibre-mirror gap, mirror-tilt and cleave quality (angle and overall flatness) of the HCF, which we will analyse in details in the following section. Further, we refer to ε also as the 'coupling loss', which is the coupling efficiency ε expressed in dB.

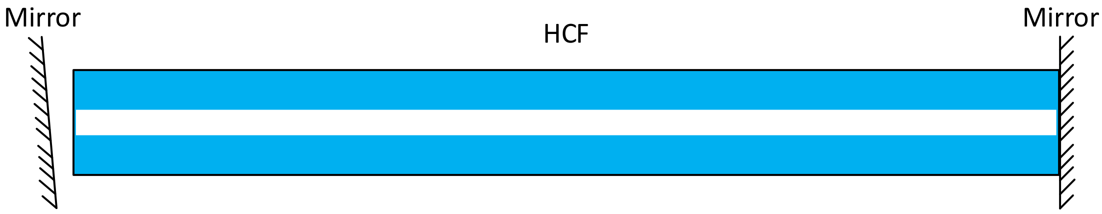

Figure 5.1 Basic structure of the analysed HCF-FP.

5.1.2 Theoretical analysis

To calculate the coupling efficiency, we need to calculate the reflected field E_r in equation (5.1). Once the light leaves the HCF, the confinement is no longer maintained, and the beam begins to spread. The diffraction of the HCF mode can be calculated by diffraction theory, however, it is complicated and thus we use an approximation.

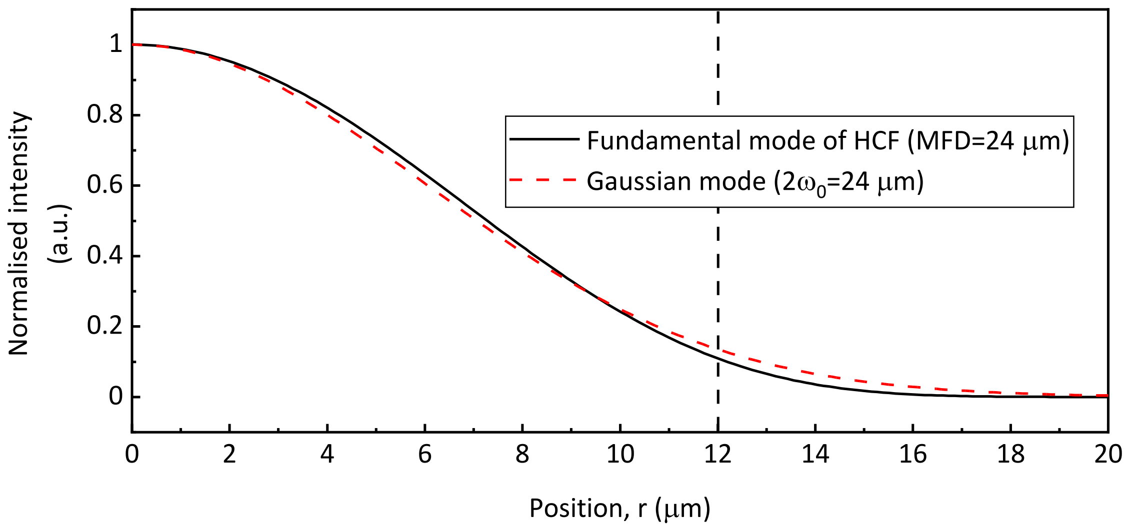

Figure 5.2 Comparison of the fundamental mode of an HCF and a gaussian mode. The gaussian mode were set to unity amplitude at r=0, and $1/e^2$ intensity at r=MFD (vertical dashed line).

Figure 5.2 shows the calculated fundamental mode of an HCF with a MFD of 24 μm, compared with a Gaussian mode. The HCF is a 6-tube NANF with the same structural parameters as reported in [17]. The Gaussian mode were set to unity amplitude at r=0, and $1/e^2$ intensity at r=MFD. As we can see here, the intensity profiles in the region where most of the power is contained are similar. Thus, we approximate that E_0 has a Gaussian mode profile and then consider propagation of the Gaussian mode to calculate the reflected field E_r. The amplitude of a Gaussian mode is given by

$$E_0 = A_0 \exp\left(-\frac{r^2}{\omega_0^2}\right). \tag{5.4}$$

Here, w_0 denotes the beam radius of the Gaussian mode, which corresponds to half of the MFD of the HCF fundamental mode. In a free space, such a Gaussian mode propagates along a distance z as

$$E(r,z) = A_0 \frac{\omega_0}{\omega(z)} \exp\left(-\frac{r^2}{\omega(z)^2}\right) \exp\left(-i\left(kz + k\frac{r^2}{2R(z)} - \psi(z)\right)\right) \tag{5.5}$$

where ω (z) is the radius at which the field amplitudes fall to 1/e of their axial values, R(z) the radius of curvature of the beam's wavefronts, and ψ(z) is the Gouy phase at the plane z along the beam [26].

$$\omega(z) = \omega_0 \sqrt{1 + \left(\frac{z}{z_R}\right)^2} \tag{5.6}$$

where

$$z_R = \frac{\pi \omega_0^2}{\lambda} \tag{5.7}$$

is called the Rayleigh distance. The wavefront curvature propagates following expression:

$$R(z) = z\left[1 + \left(\frac{z_R}{z}\right)^2\right] \tag{5.8}$$

Then, for different cases (HCF-mirror gap, mirror tilt), the reflected mode can be calculated by its geometrical transformation, which is described in the following sub-section.

Gap between HCF and the mirror:

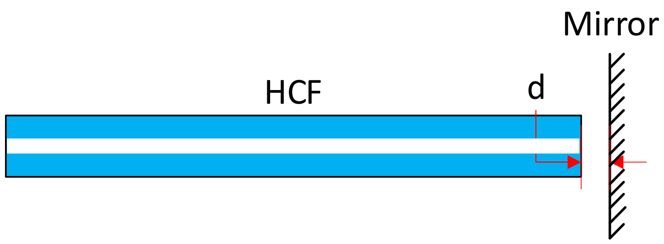

Figure 5.3 The schematic when there is a gap d in between the HCF and the mirror

When there is a gap d in between the HCF and the mirror, the reflected mode can be seen as E_0 propagating by a distance 2d, so E_r is calculated by substituting

$$z = 2d \tag{5.9}$$

into equation (5.5).

Mirror tilt:

When the mirror is tilted, it can be regarded as the mirror changes the light path. When the mode is reflected back to the HCF end, the mode amplitude at point A (x_1, y_1, 0) is the same as the point A'(x_2, y_2, z_2) when the mode is propagated in free-space on the surface of the mirror image of HCF end, as shown in Figure 5.4 (b). In such a case, it's difficult to calculate with polar coordinates, so that we perform the calculation it in Cartesian coordinate system. Let us suppose that the mirror is tilted only at x plane, which is reasonable as the Gaussian mode is axisymmetric. The relationship between A (x_1, y_1, 0) and A'(x_2, y_2, z_2) can be calculated as

$$\begin{aligned} x_2 &= \frac{x_1 - d\tan(2\theta)}{1+\tan(\theta)\tan(2\theta)} \\ y_2 &= y_1 \\ z_2 &= \frac{2\left[d + x_1\tan(\theta)\right]}{\left[1+\tan(\theta)\tan(2\theta)\right]\left[1-\tan^2(\theta)\right]} \end{aligned} \tag{5.10}$$

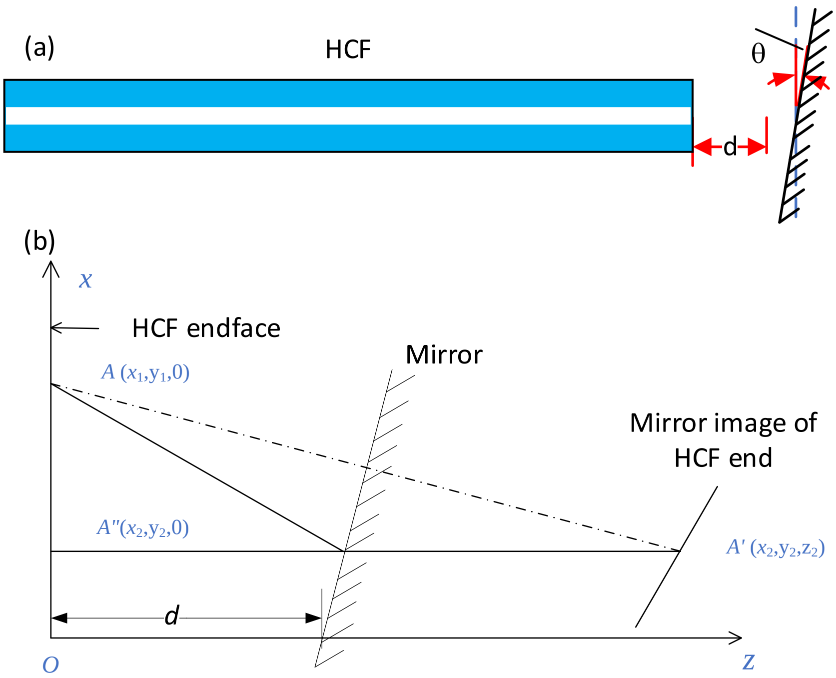

Figure 5.4 (a) The schematics when the mirror is tilted; (b) The geometrical relationship of reflected mode propagating when the mirror is tilted.

HCF cleave angle:

When the HCF is cleaved with an angle, we suppose that the mode still propagates as in free space without any refraction effect as the effective index of the fundamental mode of the HCF is very close to unity. However, the minimum distance between the mirror and HCF core centre is limited by the angle, as shown in Figure 5.5,

$$d = D/2 \cdot \tan(\vartheta), \tag{5.11}$$

where ϑ is the cleave angle. Although this may not be the dominant coupling loss factor related to the cleave quality, it is the most straightforward to evaluate theoretically and measure experimentally and can thus provide useful insight.

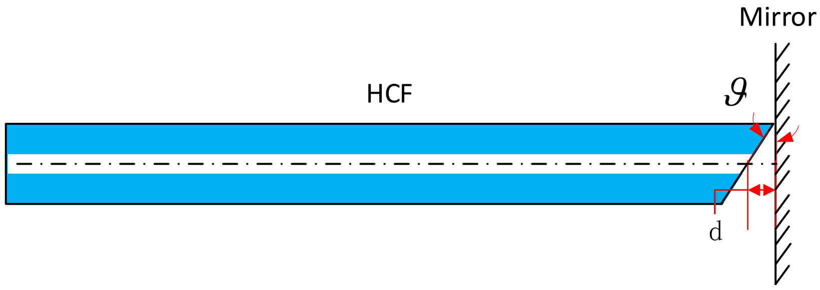

Figure 5.5 The schematic when the HCF is angle cleaved

For illustrative purposes, we calculate how the coupling loss, together with HCF-FP performance, i.e., finesse change due to mirror tilt, its distance from the HCF end and HCF cleave angle using the above equations. For this calculation we assume that the HCF fundamental mode has a Gaussian shape with a MFD = 24 μm. We calculate finesse and insertion loss (see section 2.2.3) changes due to the above factors when considering the mirror's reflectivity of 99.9% and transmission of 0.1% (loss-less mirrors). We set the integration limits to ±2 times MFD as over 99.994% of the power is constrained within this range.

Figure 5.6 shows the predicted FP performance and its degradation due to tilts in both mirrors and due to placing the mirrors at a finite distance from the HCF end facet. We see that placing mirrors more than 2 μm from the HCF end facet brings significant degradation to the coupling loss, finesse and insertion loss. Mirror tilts are also very critical, especially when mirrors are less than 2 μm from the HCF end facet, where tilt as small as 0.02° produces appreciable change in the coupling loss, thus degrading both finesse and insertion loss. For a 2 μm distance, to keep the coupling loss< -0.002 dB, and the insertion loss <-3 dB, the tilt angle needs to be controlled to within ± 0.02°.

The minimum distance at which we can place the mirror from the HCF depends on the quality (flatness, angle) of the HCF cleave. Considering HCF with an outer diameter of 340 μm, we can calculate the minimum achievable distance between the HCF core centre and the mirror for a given cleave angle. As follows from Figure 5.7, the cleave angle should be below 0.5° to avoid any appreciable degradation in coupling loss, thus also in finesse and insertion loss. Fortunately, this can be achieved with careful fibre cleaving using commercially-available fibre cleavers.

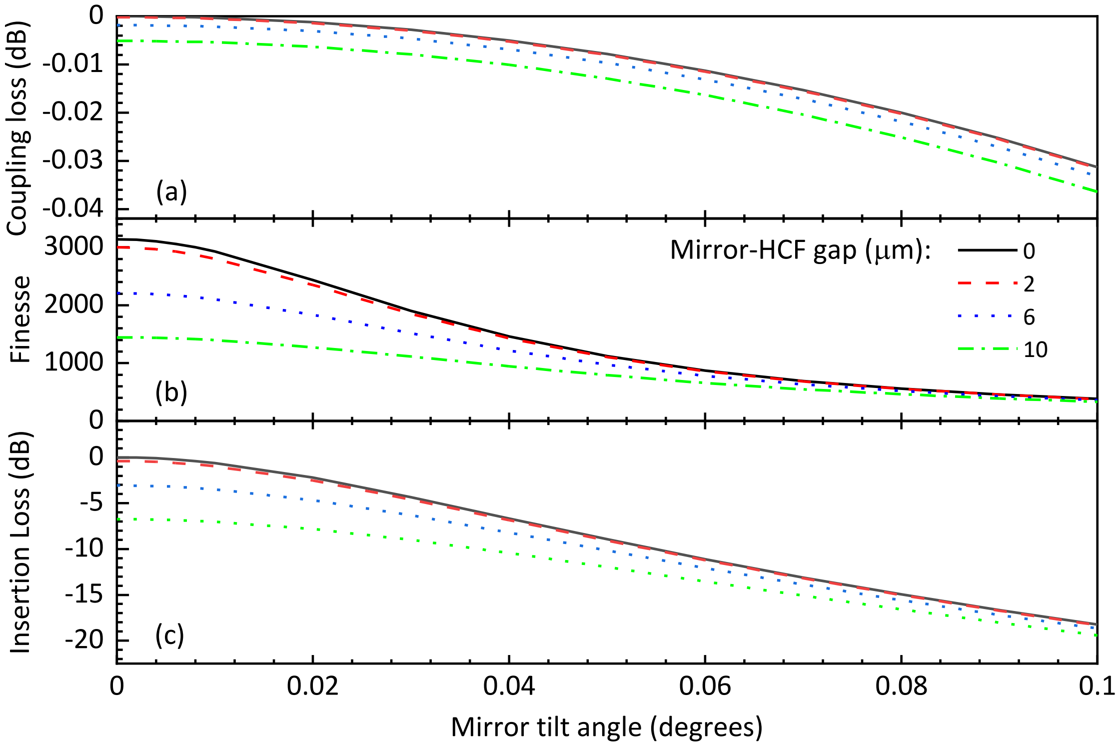

Figure 5.6 (a) Coupling loss, (b) finesse and (c) insertion loss versus mirror tilt angle, for different values of gap between the HCF end-facet and the mirror (black solid, 0 μm; red dash, 2 μm; blue dot, 6 μm; green dash dot, 10 μm).

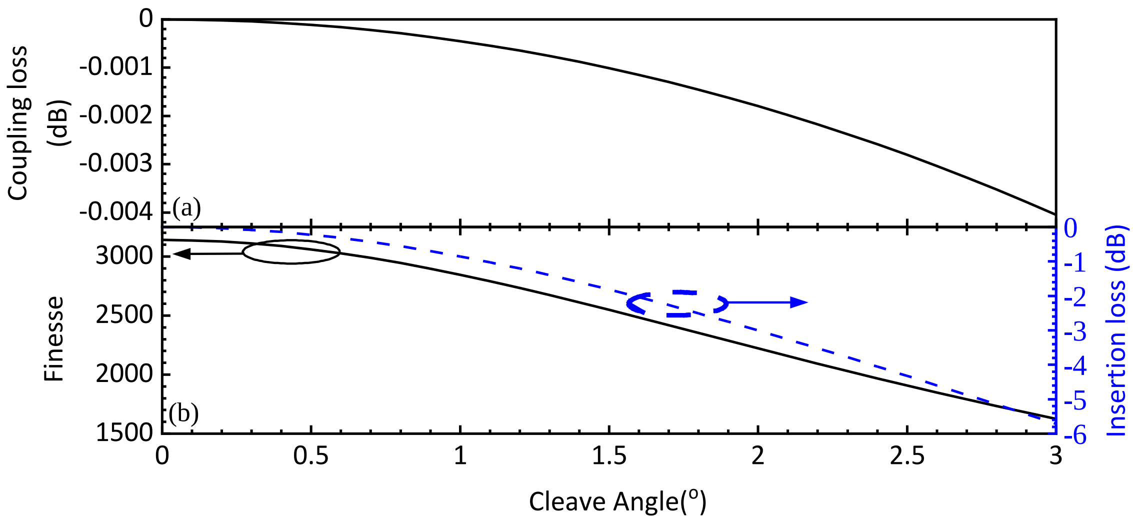

Figure 5.7 (a) Coupling loss; (b) finesse (black solid) and insertion loss (blue dash) versus cleave angle of the HCF ends.

Figure 5.8 shows how finesse, insertion loss, $\delta\nu$, and Q factor are influenced by the HCF loss, considering the latest three generations of NANF with loss of 1.3 dB/km, 0.65 dB/km and 0.17 dB/km [17,18,21]and the same FP parameters. As expected, both finesse and insertion loss deteriorate with HCF length and loss. To keep the insertion loss < -3 dB, the HCF length needs to be limited to 2.5 m for HCF with an attenuation of 0.65 dB/km and 11.2 m for HCF with loss of 0.17 dB/km.

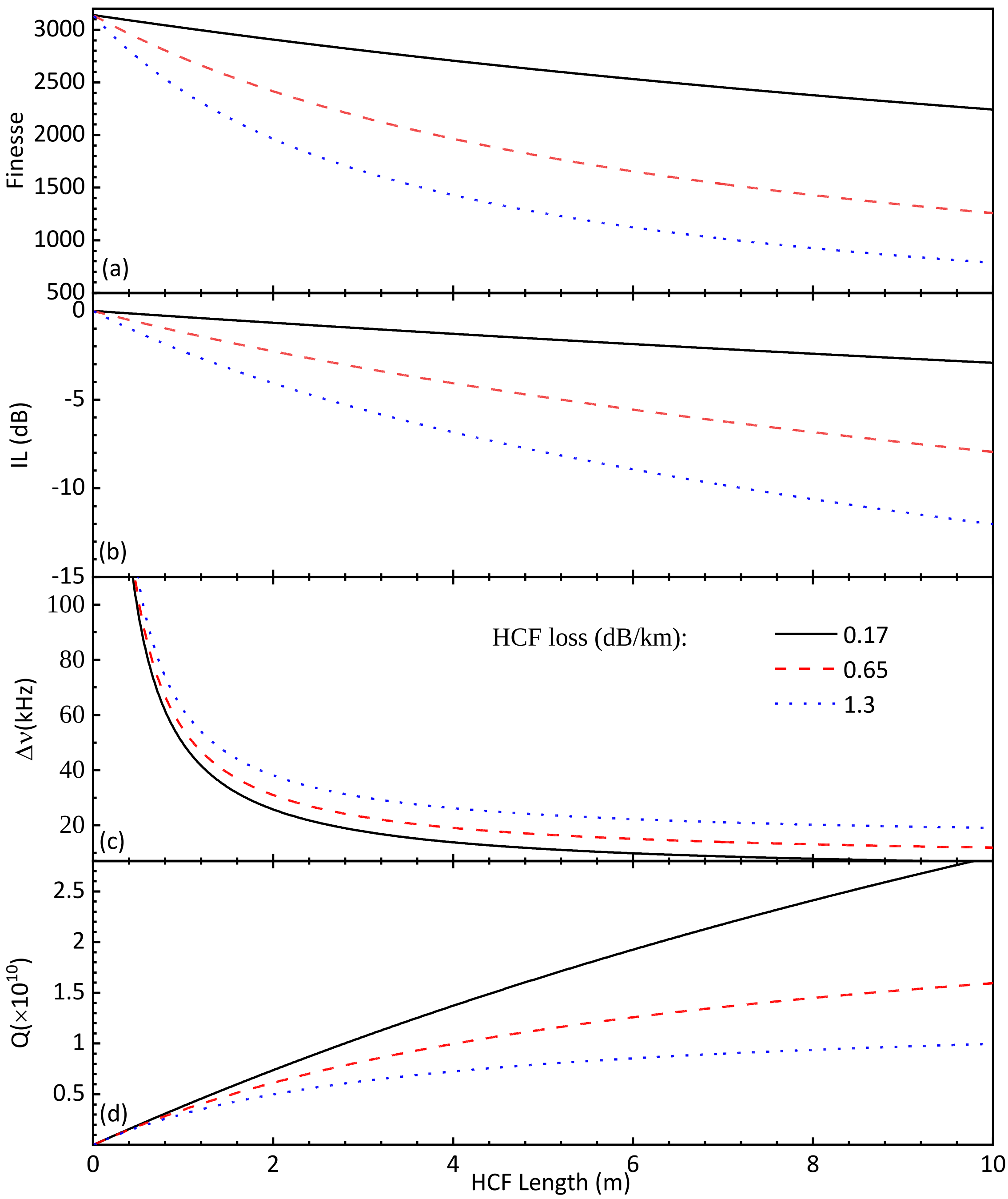

Figure 5.8 Finesse (a), Insertion loss (b), $\delta\nu$ (c), and Q (d) of HCF-FP versus HCF length for three values of the HCF loss (black solid, 0.17 dB/km; red dash, 0.65 dB/km; blue dot, 1.3 dB/km) with mirrors reflectivity of 99.9%.

5.2 Experimental setup and results

5.2.1 HCF-FP setup

To study the performance limit of the HCF-FP, we built a setup as shown in Figure 5.9, including the light coupling arrangement. The HCF is a 6-tube NANF, the cross-section of which is shown as inset in Figure 5.9. In experiments, we used the NANF sample with a transmission loss measured using the cut-back method of 0.65 dB/km. The NANF sample was first cleaved at both ends with the end-face quality carefully inspected for any cracks or irregularities. Both fibre ends were put onto 3-axes micro-positioning stages. The transmissivity of the two cavity mirrors (2-mm thick silica glass with antireflective coating on one side and high-reflective thin film dielectric coatings on the other side, reflectivity specified by the manufacturer, Union Optics, China as ">99.8%") was measured to be -32.6 dB (0.055%) and -31.1 dB (0.078%). From these measurements, the maximum possible reflectivity (that could be achieved only if the mirrors have no internal loss) was calculated to be 99.945% and 99.922% respectively. The two mirrors were mounted on tilt and yaw mounts and put close to the HCF end faces. Light was launched into the FP from SSMF using a pair of lenses. At the FP output, identical optics was used to couple light back into the SSMF. The coupling arrangement is described in the following sub-section.

5.2.2 SMF-HCF interconnection

To avoid exciting HOMs in the NANF, we need to adapt the optical field between the SMF and NANF. The principle of mode adaption by using a pair of lenses is shown in Figure 5.10. The first fibre's end is put in the front focus of the first lens while the second fibre's end is put in the back focus of the second fibre's lens. By assuming that light traveling out of the first fibre has Gaussian beam profile, the two lenses focal length ratio should be the ratio of MFDs of two fibres,

$$\frac{MFD_2}{MFD_1} = \frac{FL_2}{FL_1} \tag{5.12}$$

Since SMF's MFD is about 10.4 μm while the NANF's MFD is about 24 μm, the ratio of two lenses focal lengths was chosen to around 1:2. Considering we need enough space between lens and HCF to put a mirror to make FP and availability of lenses, we chose the first lens focal length of 18.75 mm (Collimator, F280APC-1550, Thorlabs) and the second lens focal length of 40 mm (Best form lens, LBF254-040, Thorlabs).

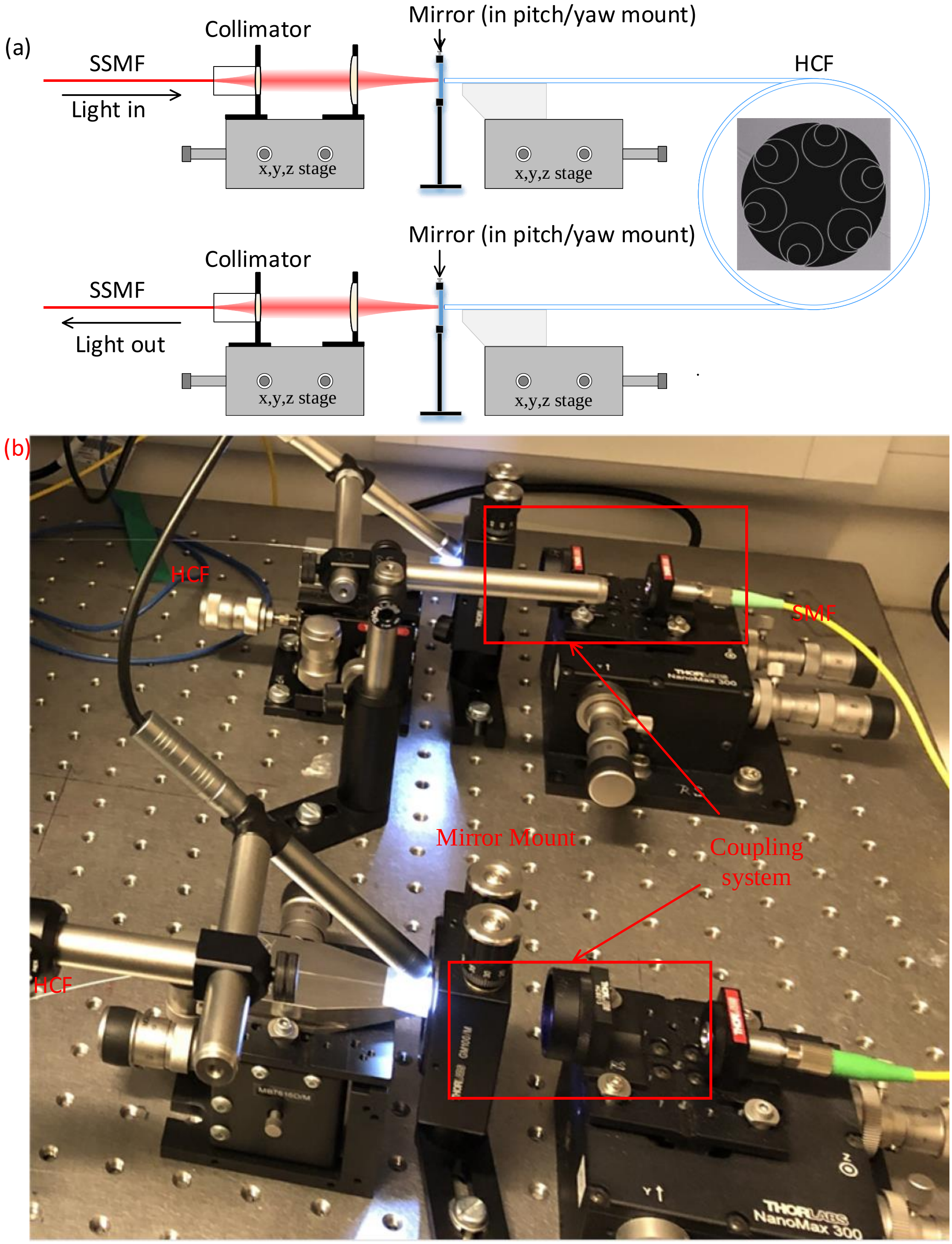

Figure 5.9 (a) HCF-FP with light coupling to and from an SMF. Inset: a cross-sectional scanning electron microscope (SEM) image of the HCF microstructure. (b) A picture of real setup with HCF sample at the left (not shown).

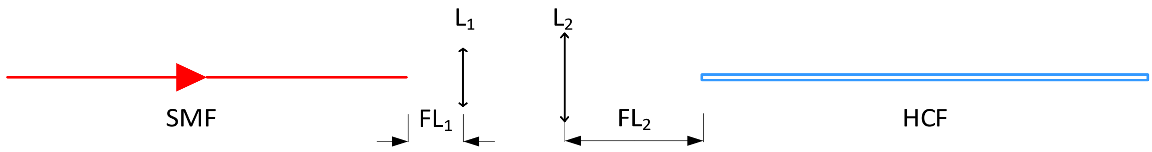

Figure 5.10 The schematic of MFD adaption by a pair of lenses.

To examine how the pair of lenses improve the interconnection of SSMF and NANF, we compared it with butt coupling of SMF and NANF. The insertion loss of SMF-NANF by different coupling methods are compared in Table 5.1. As we can see, the insertion loss is improved by more than 2 dB when lenses are used.

Table 5.1 SMF-NANF insertion loss by different coupling method

Power (dBm)	Input Power (dBm)	Output Power (dBm)	Insertion Loss
Butt Coupling	15.2	12.9	-2.3
Lens Coupling	15.2	14.9	-0.3

The HOMs components were then examined by measuring the output spectrum by an OSA. Since there are HOMs in the NANF, and different modes have different group delay, we could observe multi-path interference (MPI) at its output spectrum. To explain this, assuming that there are only two modes in the NANF, one of which is the fundamental mode while another one is a HOM. The power detected at OSA should be

$$\begin{aligned} P(\lambda) &\propto (1+a_1 e^{-j\omega\Delta\tau})(1+a_1 e^{j\omega\Delta\tau}) \\ &= 1 + a_1^2 + 2a_1\cos(\omega\Delta\tau) \\ &\approx 1 + 2a_1\cos(\omega\Delta\tau) \end{aligned} \quad . \tag{5.13}$$

where $\Delta\tau$ is the time delay difference of the two modes and a_1^2 is the power ratio between the HOM and the fundamental mode. Normally, the excited power in HOM is very small compared to the power in the fundamental mode, thus, $a_1^2 \ll 1$ and it can be neglected. As different HOMs correspond to different time delay, we can then analyse different HOMs power ratio to the fundamental mode by Fourier transforming of the spectrum at the optical domain. Figure 5.11(a) shows NANF output spectrum by different coupling methods. The output spectra are normalised to the optical source. We can see clearly fringes with two different periods, meaning that there are at least two excited HOMs in that fibre. The details then can be seen in Figure 5.11(b), which is the Fourier transform of the Figure 5.11(a). By using lenses coupling, all of them are suppressed by ~ 8dB.

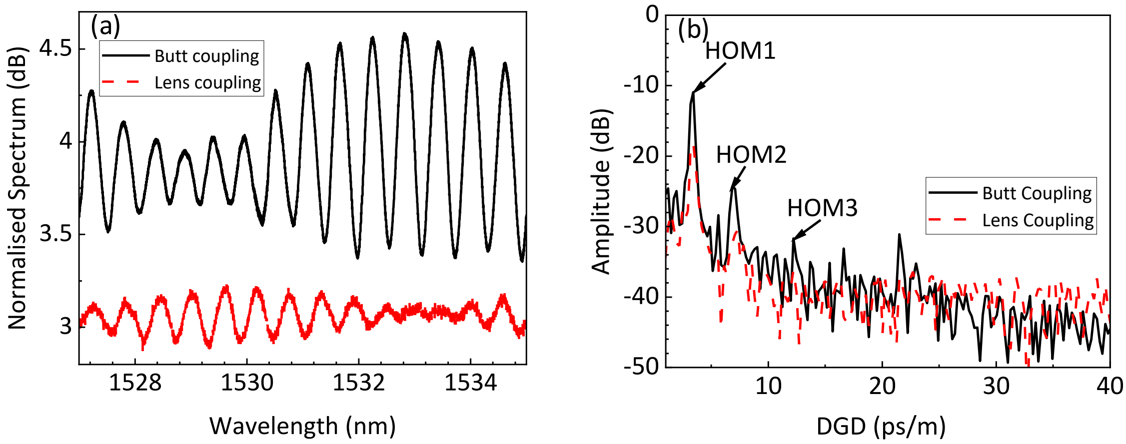

Figure 5.11 Transmission spectra of NANF and differential group delay (DGD) calculated by the Fourier transform from the transmission spectra.

5.2.3 Experimental results of HCF-FPs.

We built several HCF-FPs and studied their properties. When building these HCF-FPs, to achieve a finesse as high as possible, mirrors position (as shown in Figure 5.9), i.e., angle and distance to the HCF, need to be tuned very carefully. When tuning the mirrors position, we used the methods described in 0 to monitor the HCF-FP. For the coarse alignment, we just measured the optical power at the output end of the HCF-FP. As we increased the coupling efficiency, more power can be resonant inside the cavity leading to an increasing power at the output of HCF-FP. Once the maximum output power had been achieved, we measured the finesse on the RF spectrum as described in 0 enabling us to perform fine alignment.

Five different HCF-FPs with lengths of 0.65, 1.10, 2.50, 5.03, and 9.25 m were made. For illustrative purposes, we show the measured RF spectra and their fits (using Equation (4.9)) for the shortest and longest-length HCF-FPs, Fig. 6. The small spikes at the bottom of the RF power spectra are artefacts originating from the EDFA electronics and were observed in all our measurements. The fits (shown in insets) were performed on the first RF peak (RF frequency corresponding to the FP's FSR).

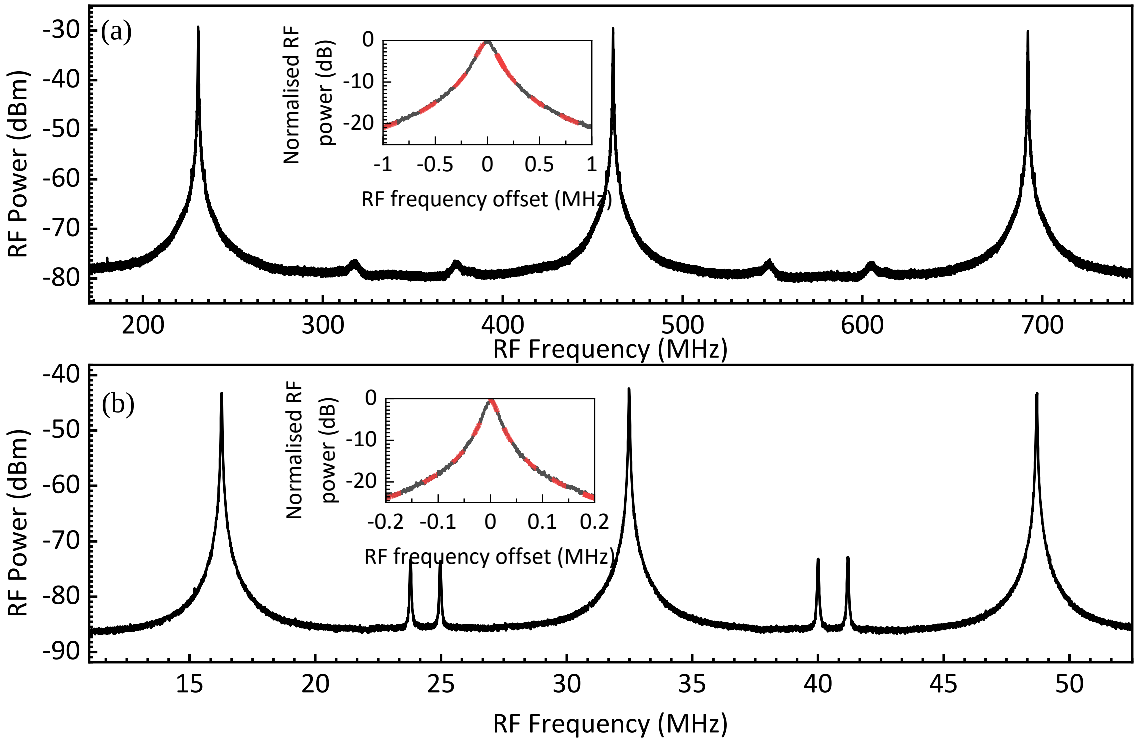

Figure 5.12 RF spectra measured at HCF-FPs outputs with the (a) shortest (0.65 m) and (b) longest (9.25 m) HCF length. The inset shows the normalized spectrum of the first RF peak (black solid: measured; red dashed: fit using Equation (4.9)by Levenberg-Marquadrdt algorithm). RF spectrum analyzer settings: (a) resolution bandwidth (RBW): 39 kHz, video bandwidth (VBW): 39 Hz; (b) RBW: 10 kHz, VBW: 5 Hz.

The measured FSR, finesse and P_{diff} for all samples are summarized in Table 1.

Table 5.2 Measured FSR, finesse, and P_{diff}

HCF-FP Length, m	FSR, MHz	Finesse	δν, kHz	P_{diff} , dB
0.65	230.7	2430	94.9	-38.0
1.10	136.2	2245	60.7	-38.0
2.52	59.6	2003	29.8	-39.5
5.03	29.8	1600	18.6	-39.7
9.25	16.2	1212	13.4	-41.3

5.2.4 Finesse and insertion loss

Finesse (Table 5.2) and Insertion loss (Equation (4.10)) for all five HCF-FPs are shown in Figure 5.13 (black, square dots). Both parameters degrade as the fibre length increases due to the signal attenuation in the fibre, as we have predicted (Figure 5.6).

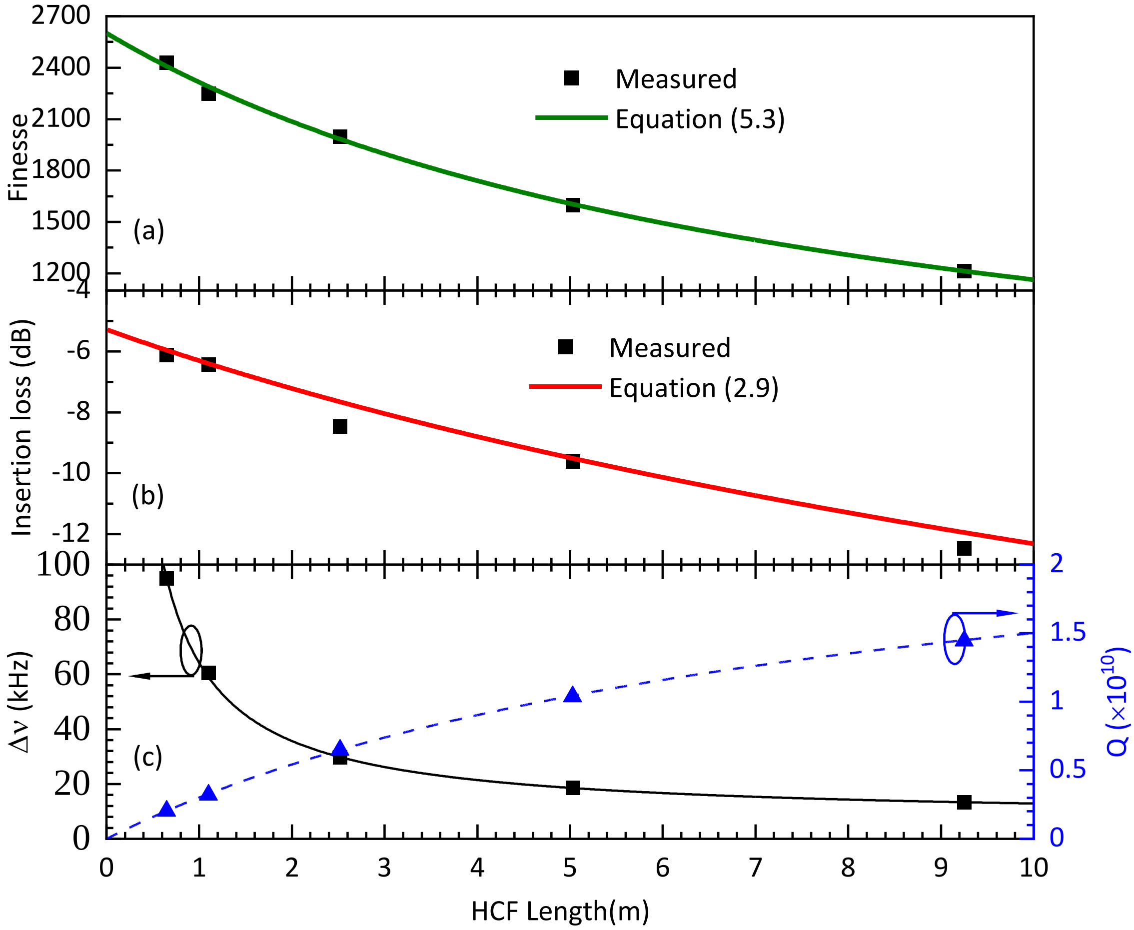

Figure 5.13 (a) Finesse (measured, black squares); fitted with Equ. (4.11) (green solid line); (b) IL of HCF-FPs (measured, black squares) and processed with Eq. (4) (red solid line); (c) corresponding FWHM of transmission peaks δν (solid black) and Q (dashed blue) for different HCF lengths.

By rewriting Equation (5.3):

$$F = \frac{\pi\sqrt{R_e \cdot 10^{\alpha_l L/10}}}{1 - R_e \cdot 10^{\alpha_l L/10}} \tag{5.14}$$

and considering all HCF-FP samples have identical effective reflectivity R_e, we can fit the measured data shown in Figure 5.13(a), finding the effective reflectivity R and HCF attenuation α_l (in dB/km) as fitting parameters. For our data, we found α_l = -0.65 dB/km and R = 99.88%. The loss value agrees well with that measured with the cut-back measurement [18]. The effective reflectivity is consistent with the mirror specification (reflectivity >99.8%) and with our mirror transmission measurement that put the upper bound of the mirror reflectivity to 99.94%. This analysis thus reliably provides parameters relevant to the HCF (α_l) and we elaborate on this in the later chapter. It also provides key parameters necessary for accurate estimation of HCF-FP performance, as we show chapter 7.1.

The calculated finesse using Equation (5.14) and the fitted R and α_l is plotted in Figure 5.13(a) (green solid line), showing excellent agreement with the measured finesse data. Further, we calculated insertion loss using Equation (4.10) with the fitted R, α_l, and measured mirror transmission $t_{1,2}$ (Figure 5.13 (b), red solid line) which again shows excellent agreement with the measured insertion loss data.

The remarkable agreement between both fits and the measured data confirms the validity of our earlier assumption that R is identical for all HCF-FP samples, showing high repeatability of our HCF cleaving and mirror alignment.

5.2.5 Broadband characteristics

Figure 5.14 (a) shows transmission of the 9.25-m HCF-FP measured with an OSA with an optical resolution of 0.02 nm. This resolution is too low to see the individual resonant transmission peaks but represents the transmission loss of the HCF-FP averaged over 0.02 nm. This transmission loss changes by as much as 1.3 dB over the measured 5 nm bandwidth, which we believe is acceptable for most applications. However, it is worth analysing its origin, which may suggest strategies as to how to reduce it.

To gain understanding, we first repeated the measurement without the two mirrors, Figure 5.14 (a). Even without mirrors, we see a power variation. We performed a Fourier transform, which shows a peak around 2.6 ps/m, which corresponds to the group delay between the NANF fundamental and LP_{11} mode, which is guided with significantly higher loss than the fundamental mode[18].

Subsequently, we performed a Fourier transform of the HCF-FP transmission spectrum, Figure 5.14 (b). We see the first peak corresponds to a double delay of the LP_{11} mode with another two peaks at the harmonics. We speculate these peaks are due to light remaining in the LP_{11} mode after successive round-trip(s) inside the HCF which then interferes with light in the fundamental mode, suggesting there is some level of coupling from the fundamental mode into the LP_{11} mode at the HCF-mirror interface. Due to the different symmetry of the LP_{11} mode and the fundamental mode, coupling between them requires some sort of asymmetry like an angle-cleave at the HCF or the mirror not being perfectly perpendicular to the reflecting beam. The reduction of the transmission loss ripple would require less coupling into HOMs or increasing HOMs' loss. The former method needs a good coupling from SMF to HCF and good mirror alignment at HCF-mirror interface. The latter one is to use HCF with HOMs with higher loss. Recent DNANFs have shown that by optimising the design we can achieve a LP_{11}'s loss 1 000 times higher than fundamental mode's loss, which would be a good candidate for us to use.

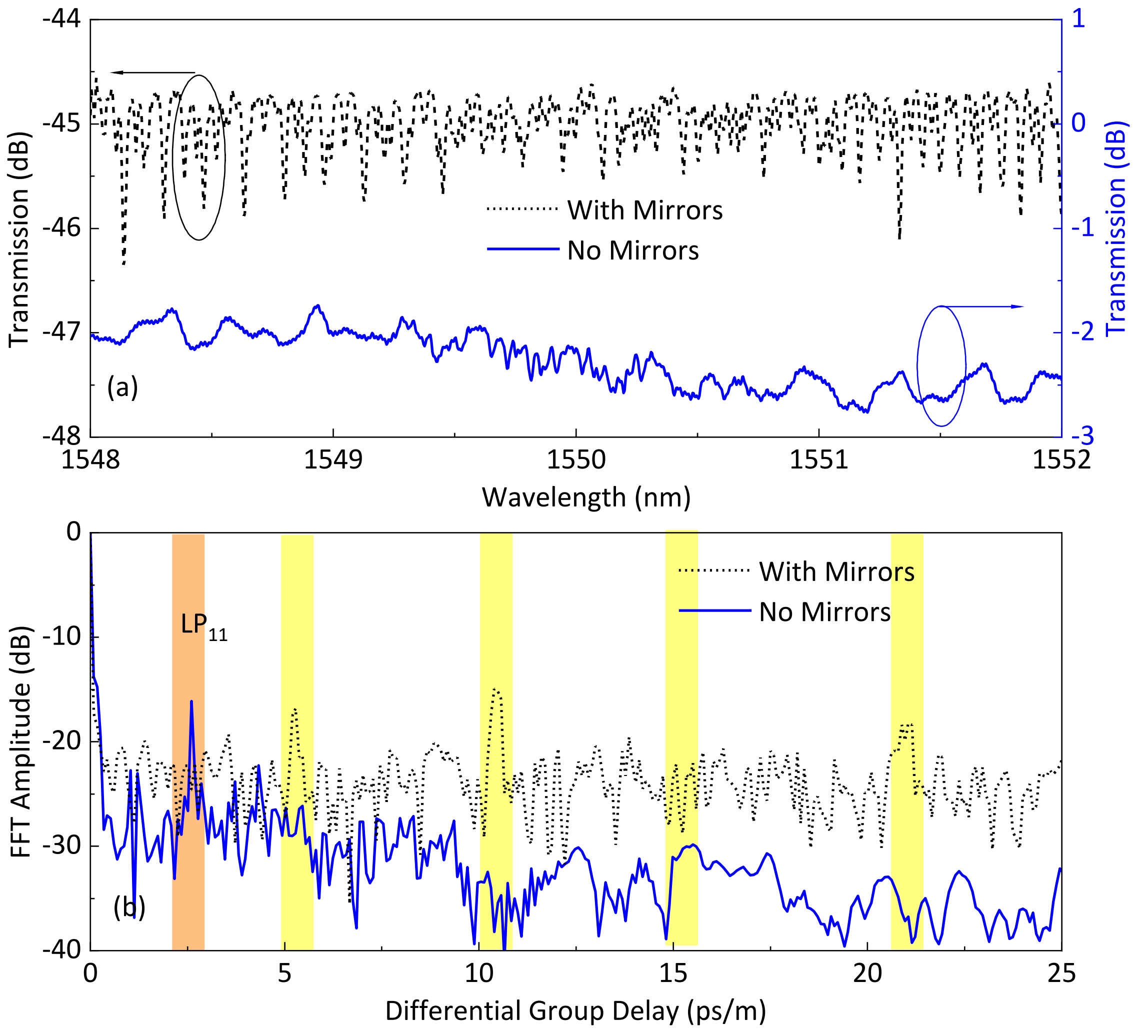

Figure 5.14 Transmission spectrum of the 9.25 m HCF-FP (dashed black line) and through HCF only (by removing the two mirrors, blue solid line) measured by OSA with 0.02 nm resolution. (b) Fourier transform of (a). Orange line shows expected position of the LP11 mode. Yellow lines show its double and its two harmonics.

5.3 Summary

Firstly, we analysed theoretically how mirror tilt, distance between the HCF and the mirror, HCF cleave angle, and attenuation of the state-of-the-art HCFs influence the performance of HCF-FPs. Following this, we constructed several HCF-FPs with HCF lengths between 0.65 m and 9.25 m and characterized them in terms of insertion loss, and finesse. Comparison of the experimental results with our theoretical analysis enabled us to estimate the key parameter that (together with the HCF attenuation) set the HCF-FP performance limits. We concluded that the coupling loss, defined in terms of the light lost when the HCF output is coupled back into the HCF via the mirror, is of critical importance. In our work the coupling loss was better than 0.0028 dB (corresponding to 99.94% of the light being coupled back into the HCF). We speculate this extremely low coupling loss is achieved mainly thanks to the HCF cleave quality.

The achieved low coupling loss would allow a finesse of over 5000 provided mirrors with a high enough reflectivity were used. Experimentally, we achieved a finesse of up to 2430 with a HCF length of 0.65 m and a finesse of 1212 with a HCF length of 9.25 m, limited by the above-mentioned coupling efficiency for short HCF-FP and HCF attenuation (0.65 dB/km used here) for the long HCF-FP. In terms of the transmission peak $\delta\nu$ and Q factor, we have achieved experimental values as low as 13 kHz for $\delta\nu$ and as high as 1.45×10^{10} for Q. This corresponds to an effective light propagation distance as long as 7 km inside the HCF-FP.

To achieve similar values in free-space-based FPs that are limited in their length, a finesse in excess of 110 000 would be needed (considering a routinely-used FP length of 10 cm), making the device extremely alignment sensitive and requiring mirrors with extremely high reflectivity/quality.

The achieved finesse of 2430 means that the power inside the cavity is 1550 times stronger than at the input, potentially enabling efficient (nonlinear) interaction with gases inside the HCF. This is of interest in a number of areas, e.g., in lasers, Raman sensing, or wavelength conversion and high-harmonic generation.

Part of the work in this chapter was published in [166].

Chapter 6 All-fibred hollow core fibre based Fabry Perot interferometers

In the previous chapter, we concluded that the finesse of HCF-FP can be made to be over 5 000. However, the setup is not sealed, and thus cannot be used in long-term applications since the HCF ends were not sealed, enabling air-born pollution like water vapor and dust to enter the hollow core. This chapter describes how all-fibred HCF-FPs are made by combining the splice technology used in [107] and the HCF-FP characterisation method described in 0. We made two HCF-FPs with a length about 5 m and 23 m, respectively. This work was done by collaboration with colleagues from the Czech Technical University in Prague.

6.1 Fabrication of all-fibred HCF-FPs

The schematic and a photograph of the all-fibred HCF-FP is shown in Figure 6.1(a) and Figure 6.1(b). The HCF used is a NANF similar to the one reported in [18] with a loss of 0.9 dB/km, operating in the 1550-nm wavelength region. The HCF-FP is pigtailed with SMF. Because of the mode mismatch between the fundamental mode of the HCF used (24 µm) and standard SMF (10 µm), a suitable piece of GRIN fibre was inserted in between the two to enable mode field adaptation [91,99]. The GRIN fibre was first fusion spliced to the SMF. Before connecting it to the HCF, a mirror was deposited on its end-face. As the system was not the same as in last chapter, and the gluing process may deteriorate the coupling loss, we didn't use a mirror with that high reflectivity as for free space HCF-FP. As an instead, we used a 13-layer Ta_2O_5/SiO_2 dielectric coating-based mirror with a reflectivity specified as >98% (from 1500-1570 nm). We did not use fusion splicing to interconnect the mirrors to the HCF, as this would destroy the mirror and could cause deformation of the HCF microstructure. We also did not use interconnection technology as shown in [10], since this approach does not allow for active alignment of the angle between the HCF and the mirror, imposing inherent limitation to reproducibility as well as the maximum achievable finesse. Instead, we used a modified fibre-array technique (used industrially for fibre pigtailing of planar lightwave circuits, PLCs) which we have refined for low-loss interconnection (<0.15 dB/interconnection) between HCFs and SMF [99]. Here, the SMF spliced to the GRIN is first glued into a V-groove array, polished to the desired GRIN fibre length, and afterwards, a coating is deposited on the end facet (the mirror in the work presented here). Then the carefully cleaved NANF is inserted into another fibre array V-groove and glued in to that. The two fibre arrays are actively aligned (in x,y,z, pitch, and yaw) before gluing the fibre arrays together to obtain a permanent and sealed interconnection, which does not allow any air-born pollutants to enter the hollow core cavity, and thus ensures no degradation in the long-term performance. A photograph of a typical glued interconnection is shown in Figure 6.1(c).

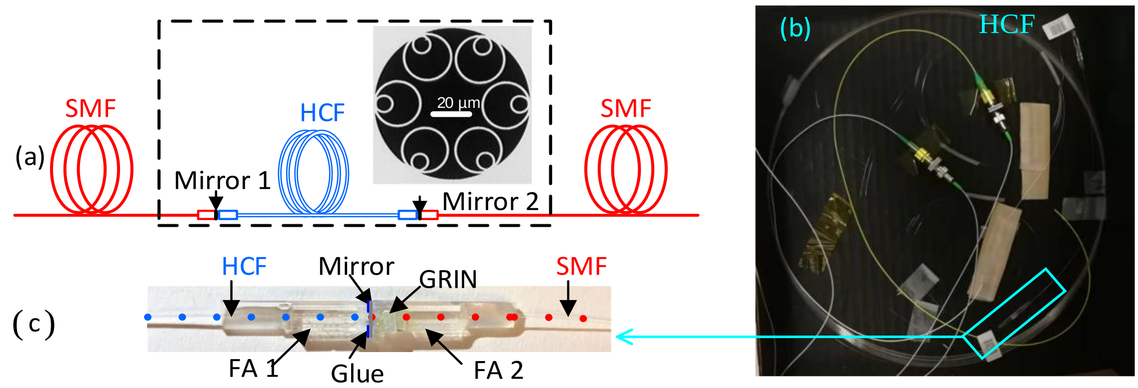

Figure 6.1 (a) Configuration of the all fibred HCF-FP with a cross-sectional scanning electron microscope (SEM) image of the HCF used. (b) Photograph of the all-fibred HCF-FP. (c) Photograph of the fully assembled SMF-GRIN-Mirror-HCF interconnection. FA: fibre array, GRIN: Graded-index fibre based mode field adapter.

By charactering the FP in real time during alignment using the method described in 0, we could optimise the FP to achieve the best finesse. We made two HCF-FP samples using 5 and 23 m long HCFs. When aligned (prior to gluing), their Finesses were 195 and 160, respectively. After gluing using a UV-curable glue, we witnessed a slight finesse reduction to 153 and 133, respectively. The deterioration is due to the mirror tilt when the glue is unevenly solidified due to curing. This may improve by optimising the curing process. Although we believe this may be improved by further refining the gluing process, the high-finesse (>120) FPs obtained are robust and have not degraded with time (we have measured the 23-m HCF-FP after almost three years since gluing them and have not seen any degradation, see Appendix B).

The 23-m HCF-FP had a smaller finesse both before and after the gluing as compared to the 5-m device. By considering the HCF loss of 0.9 dB/km and mirror reflectivity of 98.6%, analysis suggests that it is due to the HCF's attenuation.

6.2 Characterization

Following the fabrication, we characterized the FPs using two techniques - besides the convenient, fast, and high-dynamic range RF technique we have developed; we also measured it directly in the optical domain. We measured all of the important parameters (insertion loss, birefringence, and dependence on the wavelength). Finally, we measured the FPs' thermal sensitivity.

6.2.1 Characterization in the RF domain

The FP's transmission spectra including information about FSR and finesse were measured in RF domain using the method described in 0. Normalized RF power spectra showing 5 peaks around 500 MHz and normalized RF power spectra showing one peak with fitted curves for the fabricated HCF-FPs are shown in Figure 6.2. The broadband source used for this measurement had a 1 nm optical bandwidth (this narrow bandwidth allowed us to perform spectrally-dependent characterization shown later) with a central wavelength of 1550 nm (selected with the optical bandpass filter used in the source set-up, Figure 4.1). The small spikes at bottom of the RF power spectra may be artefacts originating from noise in the EDFA electronics as we have mentioned earlier. When fitting the experimental data with Equation (4.9) by Levenberg—Marquardt algorithm, we used only data above -10 dB (the blue dashed-dot line in the figure) to avoid any contribution from the measurement noise. Despite this, we achieved a very good fit even beyond the fitting range. From the fitting parameters, the FSR and finesse were measured to be 28.1 MHz and 153 for the 5 m HCF-FP and 6.5 MHz and 133 for the 23 m HCF-FP.

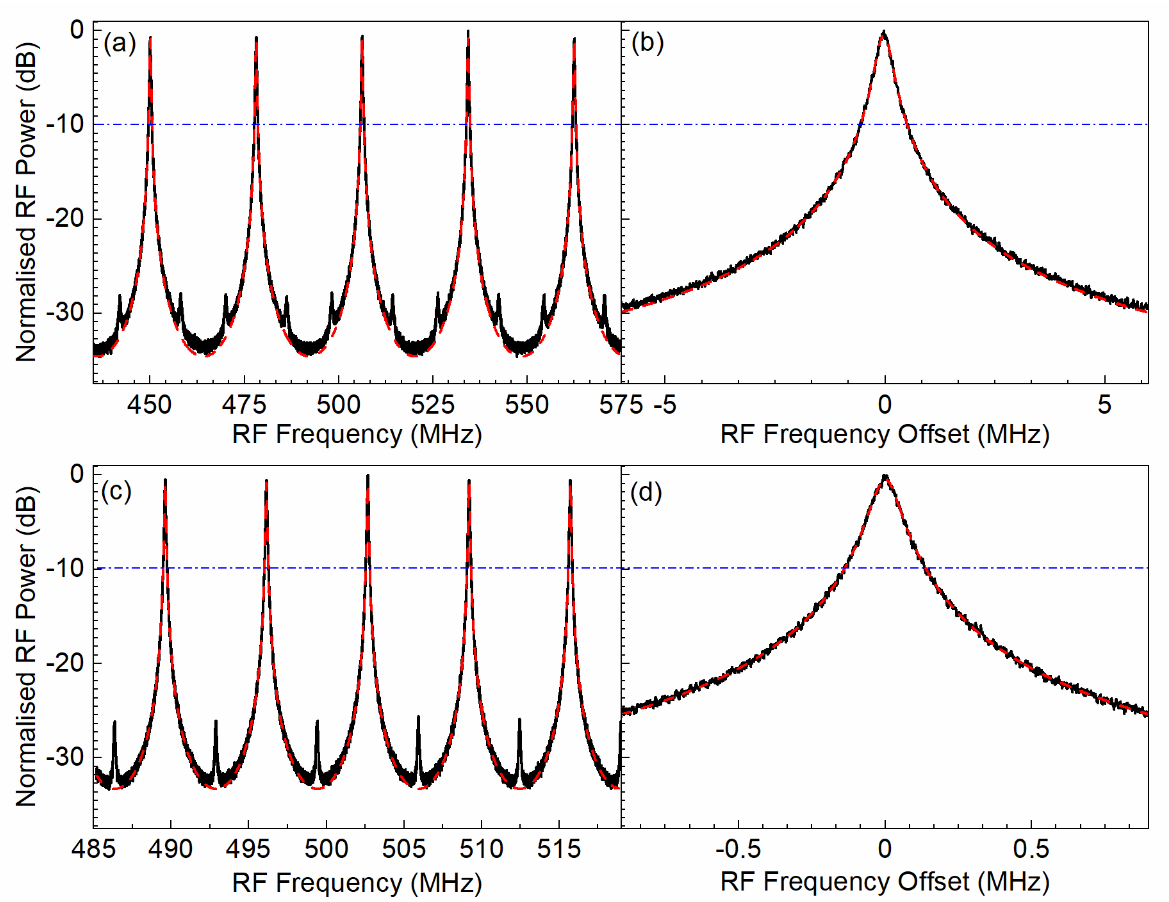

Figure 6.2 Measured and fitted RF spectra for 5 m-HCF-FP (a, b) and 23 m HCF-FP (c, d). Normalized RF power spectra around 500 MHz (a,c) and their details around one peak (b, d). Solid black: measured, red dashed: fitted with Equation (4.9).

Subsequently, we measured the RF spectrum of the HCF-FPs over the entire C band (by tuning the wavelength of the 1-nm bandwidth tunable bandpass filter, Figure 6.3). The results of both FPs are displayed in Figure 6.3 (a) (finesse) and Figure 6.3 (b) (FSR). The finesse values range from 140 to 160 for the 5-m HCF-FP and from 120 to 138 for the 23-m HCF-FP. Considering this measurement data and their variation across the C-band, the effective reflectivity was calculated to be between 97.8% and 98.1% (5-m HCF-FP) and 97.4% to 97.75% (23 m HCF-FP). The FSRs, Figure 6.3 (b) slightly decrease with wavelength (by 150 Hz for 5-m HCF-FP and 600 Hz for 23-m HCF-FP over the entire C-band). This is due to the HCF chromatic dispersion, which we confirmed by fitting the data in Figure 5.3 (b) and calculating HCF chromatic dispersion from them, obtaining value of 2 ps/nm/km. This is consistent with value expected for our NANF-type HCF [18]. It is worth mentioning that this value of chromatic dispersion is 8 times lower than SMF and thus our HCF-FP is expected to have 8 times smaller variation of its FSR as compared to SMF-FP.

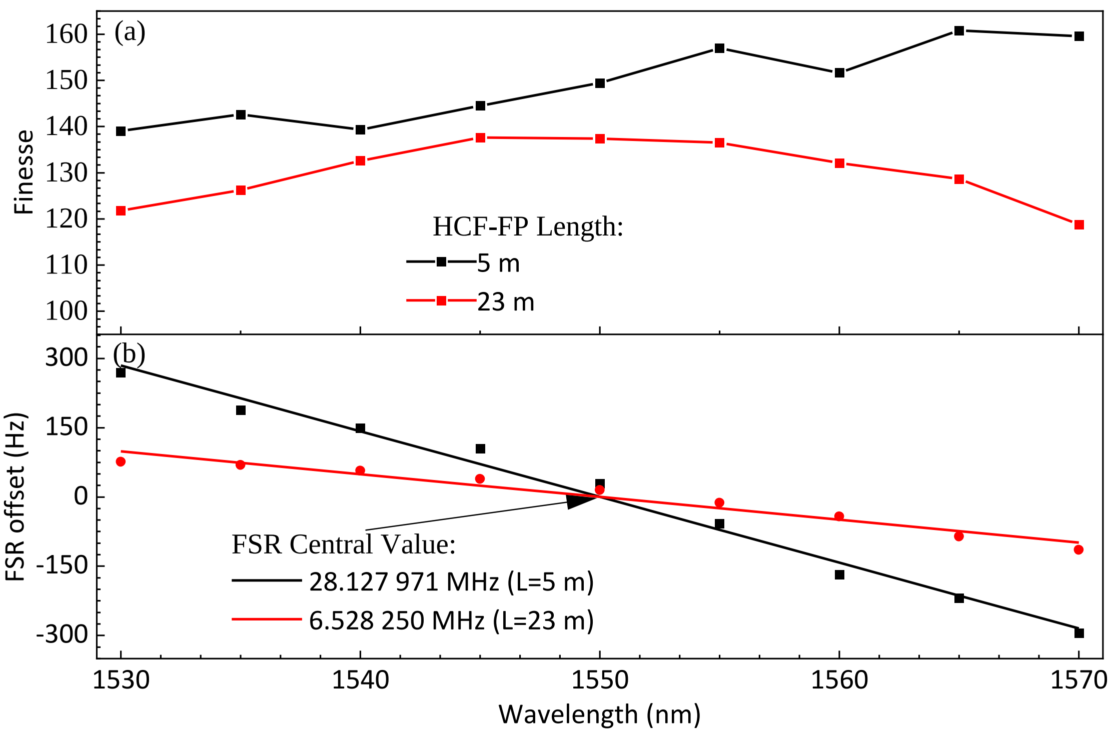

Figure 6.3 (a) Finesse and (b) FSR offset of the two HCF-FP samples measured with the RF method every 5 nm across the C band.

6.2.2 Characterization in the optical domain

Further FP parameters such as insertion loss (FP transmission loss at resonance) and polarization dependence are less straightforward to measure using the RF analysis technique. Thus, we implemented a characterization technique operating directly in the optical domain, as shown in Figure 6.4.

We scanned the input light frequency of a narrow-linewidth (< 10 kHz) fibre laser (NP Photonics, 1556 nm) by applying a sawtooth waveform on its RF port. The output was photodetected and visualized on an oscilloscope. The laser RF port response was calibrated to obtain the spectral characteristics of the FP transfer. To measure the insertion loss of the FP, the output was normalized to the case when the HCF-FP was replaced by a piece of patchcord.

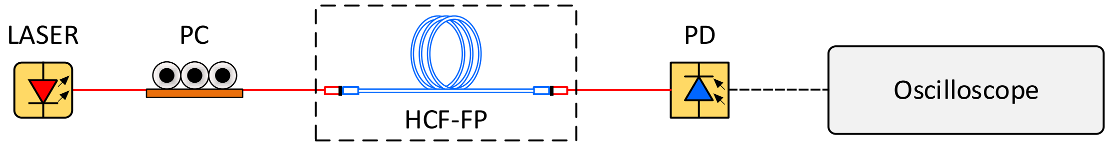

Figure 6.4 Set-up to characterize the HCF-FPs in the optical domain. PC: polarization controller; PD: photodetector.

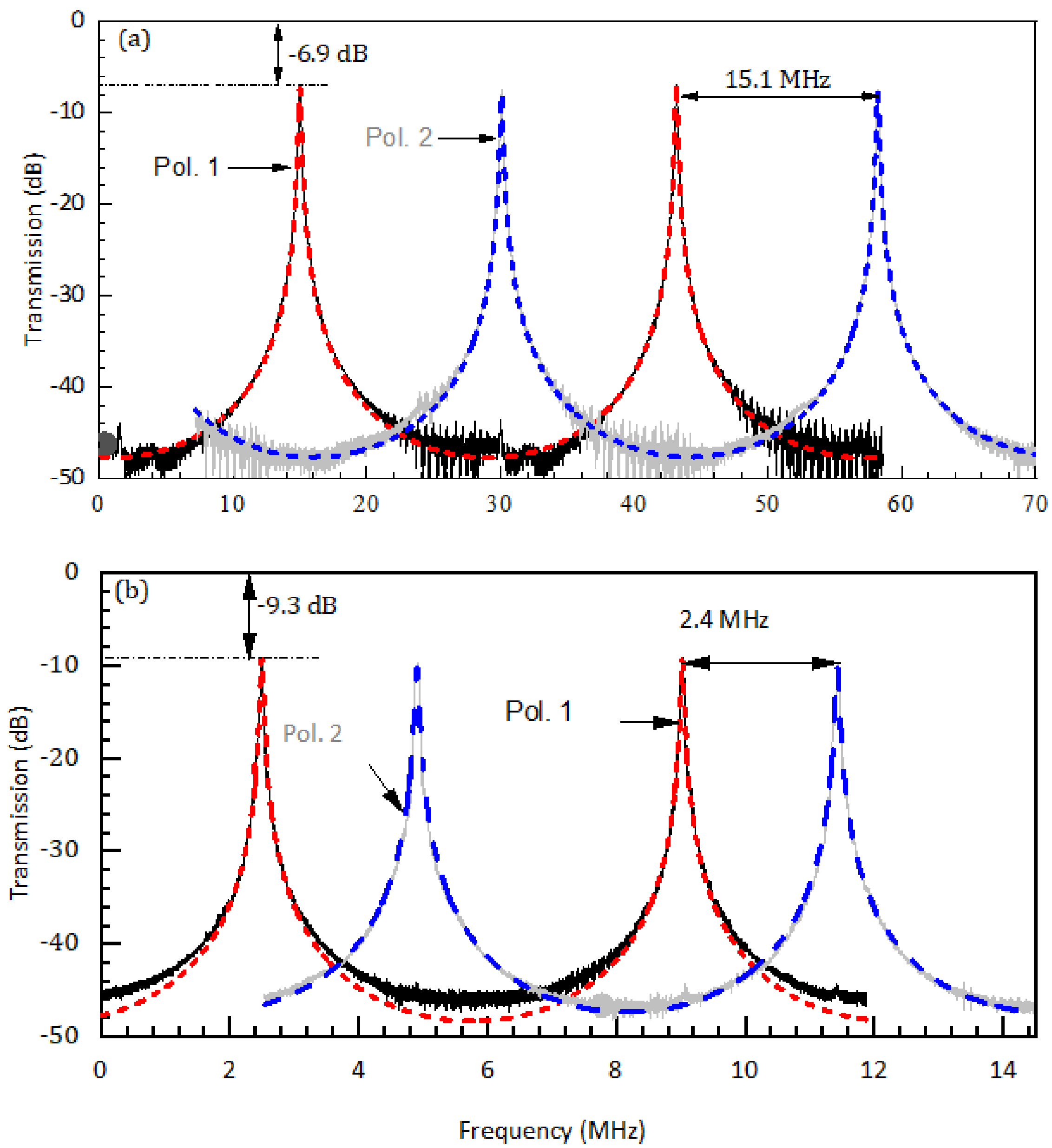

Figure 6.5 Measured optical transmission spectra along the two principal axes of birefringence (Pol. 1, black and Pol. 2, grey solid) of (a) 5 m and (b) 23 m HCF-FPs. The insertion loss and polarization-induced spectral splitting are also shown. The red and blue dashed lines are data fitted by equation (2.12).

Due to the birefringence of the HCF (caused by the fabricated HCF inner structure not being perfectly symmetric and by HCF bending/coiling[167]), transmission peaks occur at two different positions within one FSR period when varying the polarization state of the launched light (via a polarization controller, Figure 6.4). It is worth mentioning that this phenomenon is also observed with SMF-FPs in which a very small residual fibre birefringence causes this splitting. The transmitted spectra for the two polarization eigenstates of two HCF-FPs are displayed in Figure 6.5. The polarization peak spectral splitting was 15.1 and 2.42 MHz for the 5 and 23 m HCF-FPs, respectively. The phase birefringence can be calculated from the peak splitting by

$$B = n_{eff} \cdot \frac{\delta v}{c} \cdot \lambda^2 \tag{6.1}$$

where δv is the optical frequency difference of the same resonance order of the two polarisation modes. If we suppose that the two peaks for the 5 m HCF-FP were within the same FP resonance order and for the 23 m HCF-FP the FP resonance order difference was two (which we have not confirmed yet), we calculated HCF phase birefringence would have been 7.8×10^{-8} and 8×10^{-8} from the 5 m HCF-FP and 23 m HCF-FP respectively. The value also agrees well with the values reported in [167,168] for ARFs.

We measured the FP's insertion loss to be -6.9 dB for the 5 m HCF-FP, Figure 6.5, with the fitted finesse of 166 and 154 for the two polarization eigenstates, respectively. For the 23 m HCF-FP, the FP insertion loss was 9.3 dB and the fitted finesse was 139 and 130 (corresponding to 3-dB transmission peak width of 47 and 50 kHz), respectively. The obtained finesses are consistent with the RF method. Based on our theoretical analysis using Equation (2.11), the FP insertion loss is mainly caused by the mirror loss (~ 0.5% for the mirrors used). Replacing the current mirrors with improved mirrors with a loss of 0.1% would reduce the FPs insertion loss by ~3 dB. Furthermore, by improving the gluing technique (i.e., no degradation of finesse during the gluing process), we could further improve the FP insertion loss by ~2 dB for the two HCF-FPs. This is calculated by equation (4.10) considering the finesse reduction in our current HCF-FP.

6.2.3 Characterization of the thermal response

Thermal response here refers to how the transmission peaks frequency shifts with temperature. We characterized the thermal response of our 5 m HCF-FP using the set-up shown in Figure 6.6. For comparison purposes we placed the 5 m HCF-FP together with a 3.6 m SMF-FP (which has the same optical length nL as the 5 m HCF-FP) into the same thermal chamber. The SMF-FP was made by the technique mentioned in section 0. The light source (NP Photonics used earlier, but here operated at fixed wavelength) was split and launched simultaneously into both FPs. PCs were used at both interferometer inputs to align the input polarization to one of the two FPs' eigenstates. The output power of both FPs was monitored using two photodiodes.

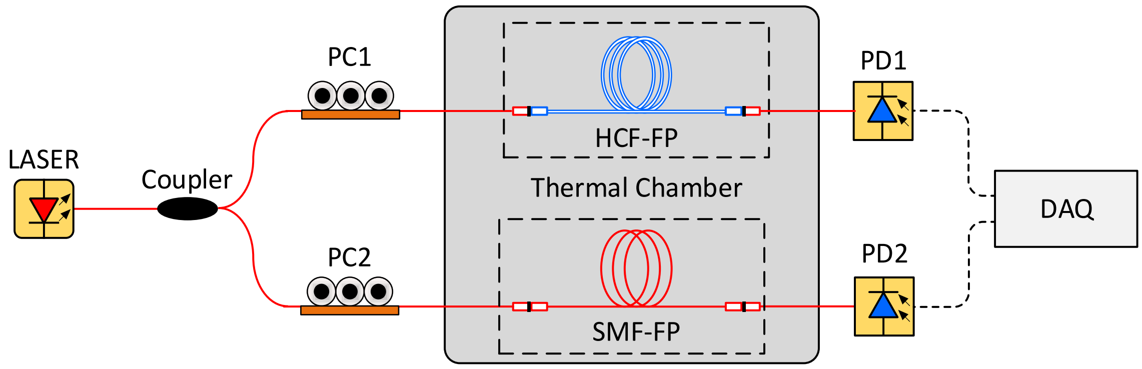

Figure 6.6 Set-up for the thermal response measurement. DAQ: Data Acquisition System.

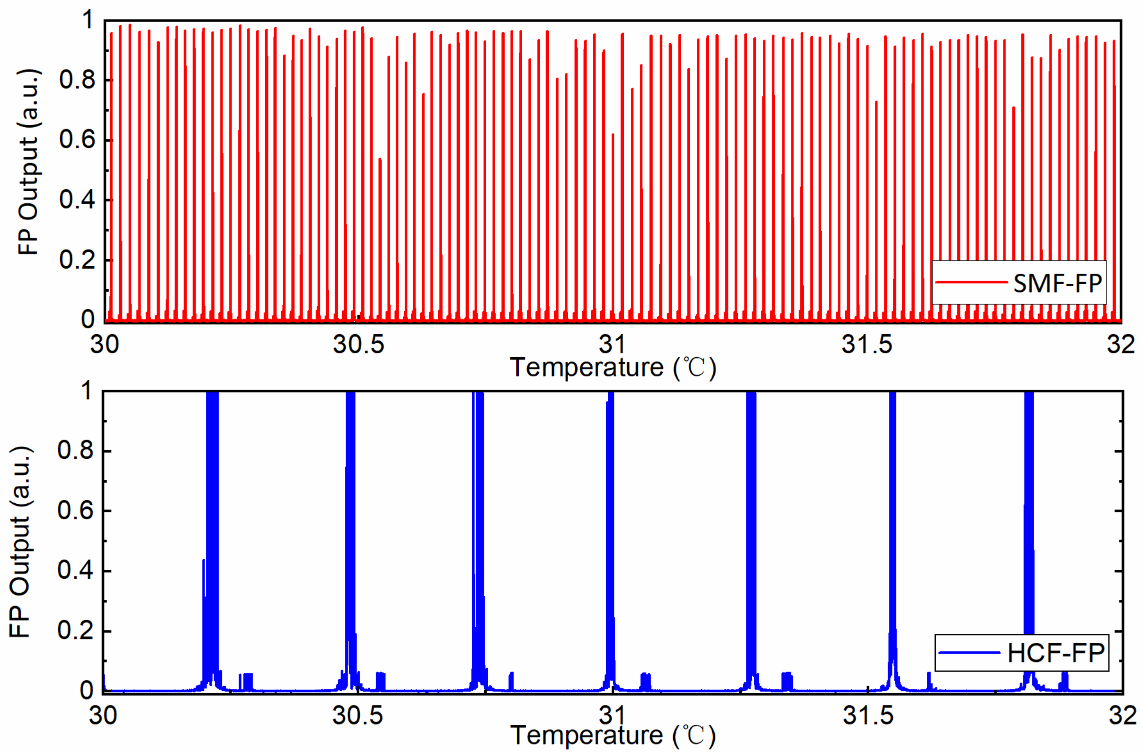

Figure 6.7 Example measurement of FP outputs for SMF-FP (red solid line) and HCF-FP (blue dashed line) when temperature is changed.

We tested the thermal response from 30°C to 40 °C Figure 6.7 shows how FPs outputs changed as a function of temperature for both HCF-FPs from 30 °C to 32 °C. Each peak corresponds to a phase change of π and the thermal phase change can then be calculated by counting these peaks (N peaks) observed

$$\Delta\Phi = N_{peaks} \cdot \pi \,. \tag{6.2}$$

From the results shown in Figure 6.8, we see that the phase change per unit length of HCF-FP is much smaller than that of SMF-FP when temperature changes. The calculated thermal sensitivities are 0.57 ppm/°C and 8.27 ppm/°C, respectively for HCF-FP and SMF-FP. These results agree well with the previous measurement of HCF and SMF [14]. Thus, the thermal sensitivity of HCF-FP is 14.5 times lower than that of SMF-FP, which matches well with the theoretical prediction. The thermal sensitivity of the made FPs at other temperatures is not the interest of my scope here, so I did not test it here. However, we can expect from [88] it will increase at cryogenic temperatures. That is because although silica's CTE can be even negative at cryogenic temperatures, the fibre we used here are dual-coated and the coating can be stiffer at cryogenic temperature. However, by using thinly coated HCF, this problem can be solved. Although it is not public domain, my colleague has tested a thinly coated HCF at low temperature, which has zero thermal sensitivity at cryogenic temperatures.

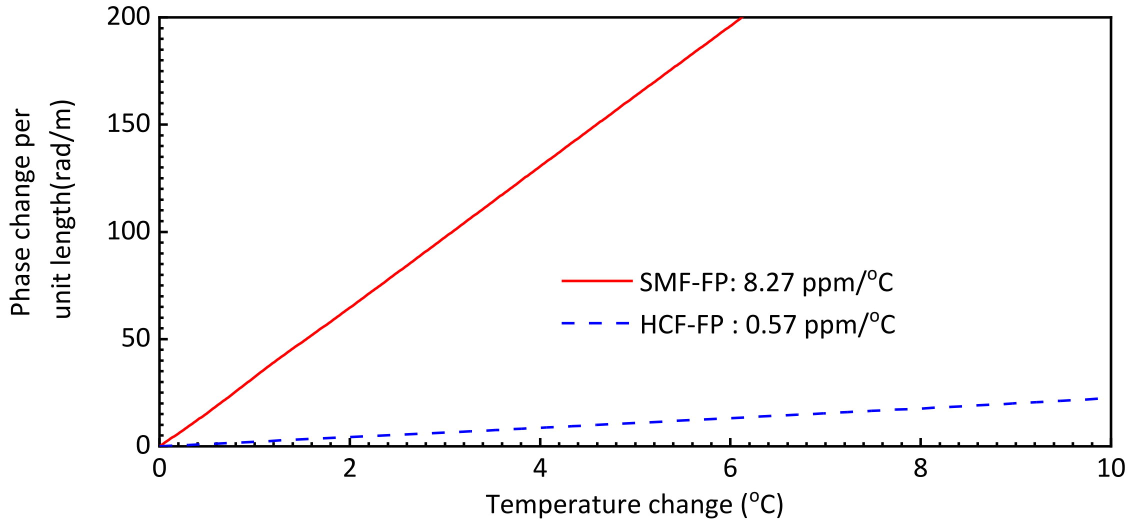

Figure 6.8 Phase change per unit length of HCF-FP and a SMF-FP (of equivalent optical length) as the temperature is increased.

6.3 Summary

In summary, we fabricated 5-m and 23-m long HCF-FPs. Our fully assembled permanent-connection based FPs have finesse >120 over the entire C band, which represents the first demonstration of all-fibred long HCF-FPs with such a high finesse. Especially, this is the first time to demonstrate HCF-FPs that can be used in long-term. This was enabled by the combination of the latest-generation of low-loss (sub-1dB/km) HCFs and the recently developed technique for permanent, low loss, fusion-splice-less sealed HCF interconnection with standard optical fibres. We achieved a FP transmission peak width as narrow as 47 kHz (with an equivalent time delay of 3.2 km). This is only a factor of three wider than for state-of-the-art bulk FP cavities that are typically 10 cm long and have a finesse in excess of 10^5. We also showed HCF-FPs to have 14.5 times lower thermal sensitivity than SMF-FPs, which is due to the HCF's low thermal phase sensitivity. The performance we demonstrate here, together with the expected high nonlinear threshold, will be of interest in many applications in which SMF-FPs cannot be used and free-space FPs are impractical.

I also summarise here some parameters (e.g., length, FSR, finesse and Q value) of our home made HCF-FPs shown in chapter 5 and chapter 6 and one free-space FP made from ULE glass [4] and SMF-FP made from Luna Innovations [34]. As we can see clearly here, HCF-FPs can really combine the advantages of free-space FP and SMF-FP. HCF-FPs show better thermal sensitivity than SMF-FP. This is from the property of HCFs. Although it is still not comparable to the free-space FP made from ULE glass, we can expect better performance of HCF-FP in the future if we fully reduce the HCF's thermal sensitivity. In the meantime, HCF-FPs show an advantage of light weight and easy to operation compared to free-space FP.

Table 6.1 Summarise of our home-made HCF-FPs with free-space FP and SMF-FP

	Free-space FP [4]	SMF-FP [34]	Free-space coupling HCF-FP (in chapter 5)	All-fibred HCF-FP (in chapter 6)
Length	0.48 m	< 10 m	0.6 - 10 m	23 m
FSR	312 MHz	> 10 MHz	16 -230 MHz	6.5 MHz
Finesse	282 000	2 000	2300	133
Peak width	1.1 kHz	5 kHz	13 kHz	47 kHz
Q value	1.7×10^{11}	4×10^{10}	1.45×10^{10}	4×10^{9}
Thermal sensitivity (ppm/K)	≈ 0	1.6 GHz/°C	Not tested	0.11 GHz/°C

This work was published in [169].

Equation Chapter (Next) Section 1

Chapter 7 Applications of Fabry-Perot interferometers

In the last two chapters, we have made HCF-FPs with two different structures. In this chapter, we will use the two developed HCF-FPs in two different applications. As high-finesse HCF-FP is very sensitive to the fibre loss and we have concluded that our setup shown in Figure 5.9 can produce reproducible results, we will use the HCF-FP setup shown in Figure 5.9 to measure HCF transmission loss. Our home-made HCF-FPs, shown in Figure 6.1, has shown long-term stability. In this chapter, we will use it to make a narrow-band microwave photonics bandpass filter.

7.1 HCF-FP used in fibre loss measurement

Considering the HCF transmission loss α_l, coupling loss ε at the mirror and mirror reflectivity R, the average loss per pass in an HCF-FP is given by

$$A = \alpha_l L + 10\log_{10}(\varepsilon) + 10\log_{10}(R) \text{ [26].} \tag{7.1}$$

The average loss per pass can also be calculated from the finesse. The relationship between the average loss per pass and finesse can be get by combining equation (7.1) and equation (5.14),

$$F = \frac{\pi\sqrt{10^{A/10}}}{1-10^{A/10}} \tag{7.2}$$

As we have demonstrated in section 5.2.4 that reproducible results were achieved with our setup shown in Figure 5.9. In particular, this means that every time we made the HCF-FP, the coupling loss ε is identical within a very small error, allowing us to treat it being constant. Since the mirror reflectivity R does not change as we use the same pair of mirrors, equation (7.1) can be rewritten as

$$A = \alpha_l L + \text{constant} \tag{7.3}$$

which is a linear function dependent on fibre length only with two unknow parameters, i.e., the fibre loss α_l and the constant term. Thus, in principle, by making HCF-FP with two different lengths and measuring their length and loss per pass from FSR and finesse respectively, we can extract the fibre loss. Except coupling loss error, the measurement error of fibre loss also include finesse and FSR measurement error, so for each length, we recorded 30 times measurement of finesse and FSR. We measured two HCF samples and their measurement losses by FP method are compared with the losses measured by the cut-back method in Table 7.1. We show in Figure 7.1 how the measured loss per pass A changes with fibre length for the two fibre samples. Fibre 1 is a 6-tube NANF with the same structure as reported in[18] and fibre 2 is a double-nested antiresonant nodeless fibre (DNANF) which has the structure same as the one just reported in [21]. As we can see in Figure 7.1(a), the measured loss per pass versus length shows a very good linear trend. The fitting gives us an R^2 to be 0.99. The HCF losses measured by FP method agree well with that measured by cut-back method.

Table 7.1 Comparison of loss measurement results got by FP method and cut-back method

Fibre loss (dB/km)	FP method	Cut-back method
Fibre 1	0.659±0.024	0.65±0.08
Fibre 2	0.174±0.015	0.22±0.05

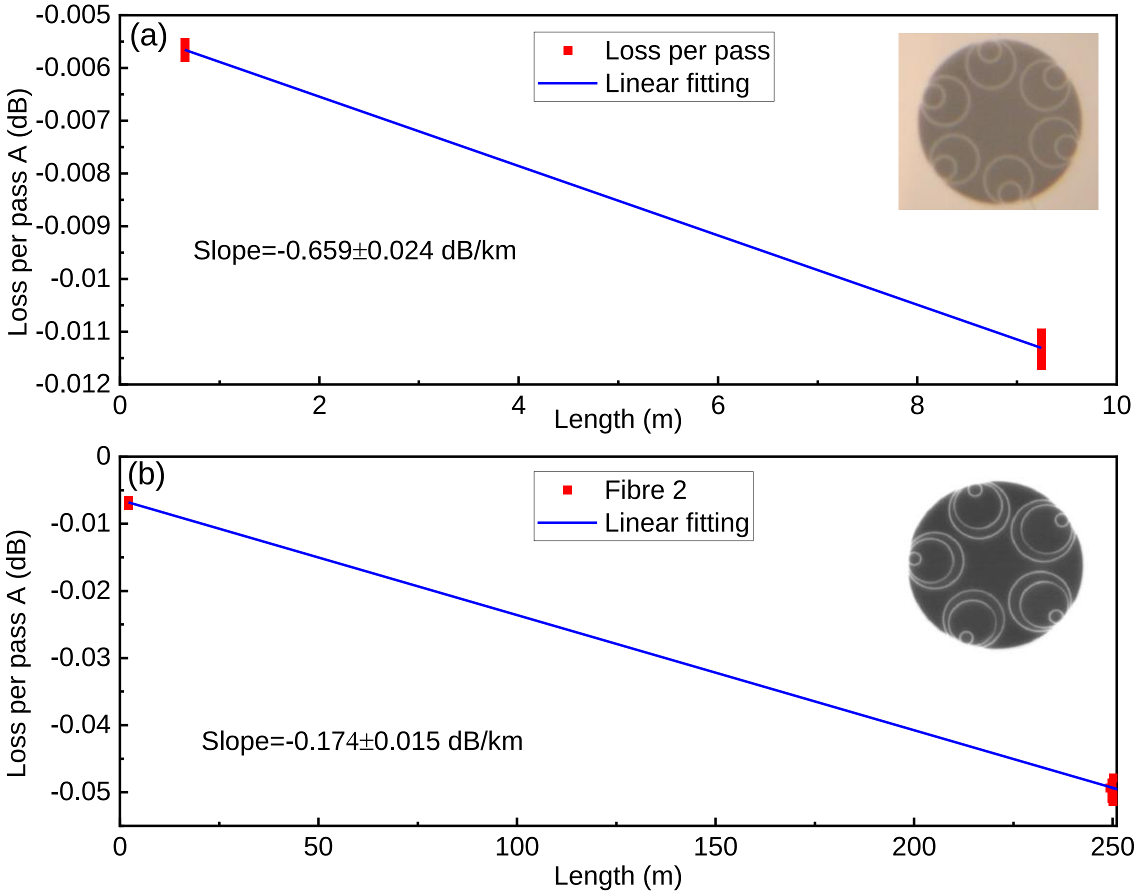

Figure 7.1 Two examples of calculated loss per pass A by the finesses of HCF-FP with different lengths. (a) NANF with the same structure as reported in [18]; (b) Double-nested antiresonant nodeless fibre (DNANF) with the same structure as reported in [21]. Cross-sectional images of the two HCFs are shown in the figure.

7.2 Microwave photonics filter

In section 6.2.3, we have shown that the HCF-FP has about 15 times better thermal stability than an SMF-FP. In this section, we show that how a microwave photonics filter (MPF)'s stability can be improved by using HCF-FP as opposed to SMF-FP.

7.2.1 Set-up of the MPF

The schematic of our MPF is shown in Figure 7.2. A signal from a continuous-wave fibre laser (Rock from NP Photonics) with an output power of 16 dBm and wavelength of 1555.5 nm passes through a 40-GHz bandwidth Mach-Zehnder modulator (MZM), which generates two sidebands at the frequency of the RF input signal. After passing through a polarization controller (PC), the signal is injected into the FP. To compare the property of an MPF made of SMF-FP and HCF-FP, we used the 5 m-long HCF-FP we show in the last chapter and the 3.6 m-long SMF-FP used in section 6.2.3. There is a length difference here because of the refractive index (n) difference (~1 for HCF and ~1.45 for SMF). The optical length (nL) of the two FP is nominally identical, allowing for a fair comparison. The laser central frequency is set (we explain later how we set this) to be resonant with the FP, i.e., to have minimum transmission loss. Both sidebands experience the same transmission loss – i.e., both are transmitted (when the RF signal frequency is a multiple of the FP spectral period) or both are equally attenuated. Thus, the FP output signal is amplitude-modulated with a modulation depth dependent on the RF signal frequency. The output signal from the FP is divided into two parts and then photo detected. One of them is the output RF signal and is received by a vector network analyser (VNA) to measure the amplitude and phase response of the MPF. The other one is used for the laser wavelength locking to a transmission peak of the FP via a feedback loop consisting of a lock-in amplifier, proportional-integral (PI) controller, and a piezo-stretcher that controls the wavelength of the Rock fibre laser.

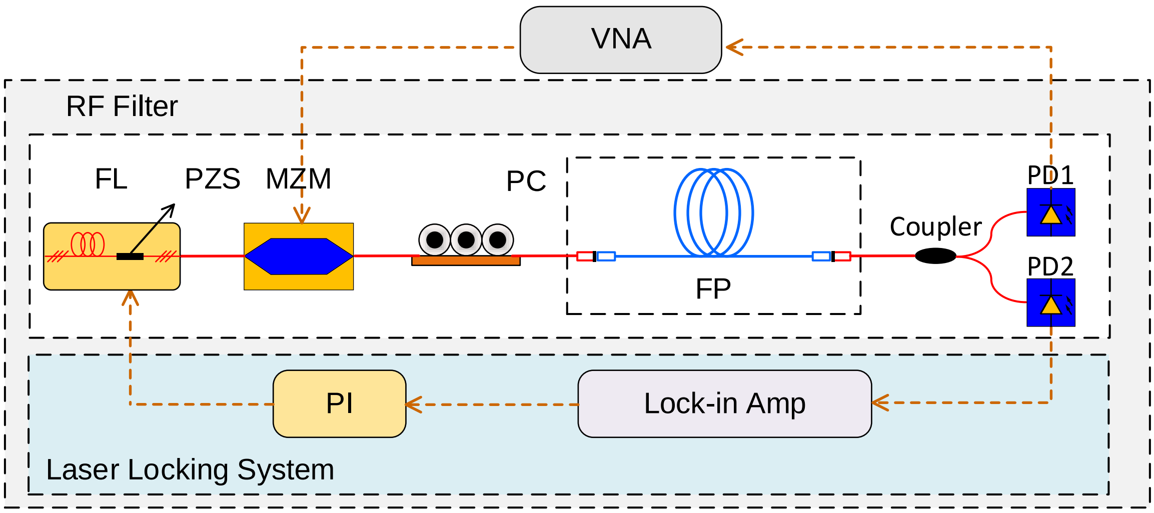

Figure 7.2 Experimental set-up. FL: fibre laser; PZS: piezo-stretcher; MZM: Mach-Zehnder modulator; PC: Polarization controller; PD: photodiode; VNA: Vector network analyzer; PI: proportional-integral controller.

7.2.2 Simulation of the MPF

We first simulate an HCF-FP based MPF. Based on [170], an FP based MPF's transmission function can be written as

$$P_{RF}=\frac{m^2\left(1-R\right)^4}{\left(1+R^4-2R^2\cos 2\omega_1\tau\right)}\cdot\left|2+\frac{R\mathrm{e}^{2j\omega_0\tau}}{1-R\mathrm{e}^{2j\omega_0\tau}}+\frac{R\mathrm{e}^{-2j\omega_0\tau}}{1-R\mathrm{e}^{-2j\omega_0\tau}}+\frac{R\mathrm{e}^{-2j(\omega_0+\omega_1)\tau}}{1-R\mathrm{e}^{-2j(\omega_0+\omega_1)\tau}}+\frac{R\mathrm{e}^{2j(\omega_0+\omega_1)\tau}}{1-R\mathrm{e}^{2j(\omega_0+\omega_1)\tau}}\right|^2 \tag{7.4}$$

without considering the laser source's limited temporal coherence. Here, m denotes the modulation depth, R, the reflectivity of the mirror (we suppose that the two mirrors of the FP are identical), ω_0 the optical carrier angular frequency, ω_1 the RF angular frequency, $\tau=\frac{L}{c}$ the single-path time delay in the FP. I simulated a 5 m HCF-FP based MPF, and I set the carrier angular frequency as resonant condition and non-resonant condition to see the carrier frequency's influence on MPF's transmission characteristics. The resonant condition of the optical carrier is set as

$$\frac{\omega_0\cdot\tau}{\pi}=m \tag{7.5}$$

where m is an integer. The non-resonant condition is set as

$$\frac{\omega_0\cdot\tau}{\pi}\neq m\,. \tag{7.6}$$

We set $\left(\omega_0\cdot\tau\right)/\pi$ =m+1/32, 1/16, 1/8, 1/4, 1/2 respectively. Figure 7.3 shows an example of a 5 m HCF-FP. Here, I set R=98%. As a comparison, I also show here the optical spectrum of the 5 m HCF-FP. The MPF have the same linewidth at peaks as the HCF-FP. The MPF transmission characteristics with different carrier condition are aslo shown in Figure 7.3 (b). As we can see here, it is critical that the carrier frequency is locked to the resonant peak of the HCF-FP. This work was done by laser lock system shown in Figure 7.2. Figure 7.4 shows the transmission signal and error signal before and after turning on the locking loop.

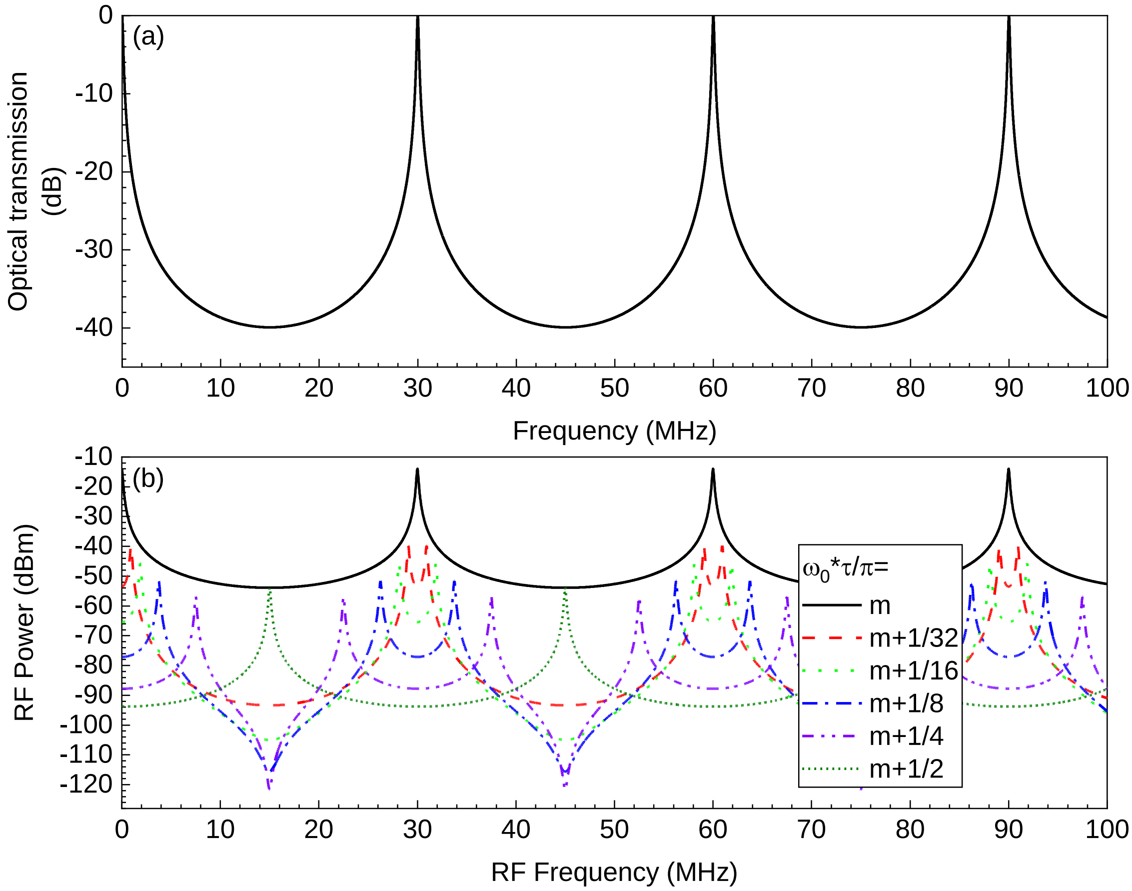

Figure 7.3 (a) The optical spectrum of a 5 m HCF-FP and (b) the RF spectrum of the MPF based on the 5 m HCF-FP at different carrier condition.

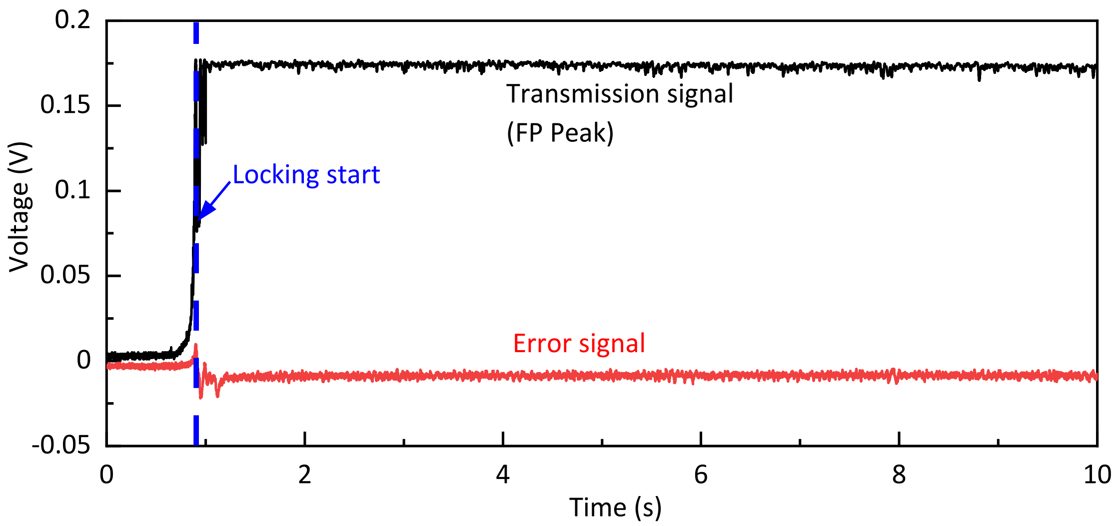

Figure 7.4 Transmission signal and error signal before and after the laser wavelength has been locked to a transmission peak of the FP.

7.2.3 Filter transmission characteristics

We show here only the filtering characteristics for the HCF-based filter, as the filter characteristics for SMF-based filter were very similar. The filter has a periodic transfer function with period of 28.1 MHz (given by the FP length of 5 m), shown in Figure 7.5 at RF frequencies close to 10 GHz, 20 GHz and 40 GHz.

Details of the amplitude S21 response together with the phase response are shown in Figure 7.6. The 3 dB passband width is 273 kHz, giving a finesse of 103, which is 50% lower than the value we measured in the last chapter. This may be because that we coiled the HCF-FP with smaller coiling diameter than in the last chapter. In the last chapter, the coiling diameter was 30 cm and it was 16 cm here. The phase response change within a frequency range of FSR is π as expected. I also calculated the group delay and group delay dispersion of the filter based on the measured phase response. To make it even clearer, I also plot them within 3 dB transmission band of the filter.

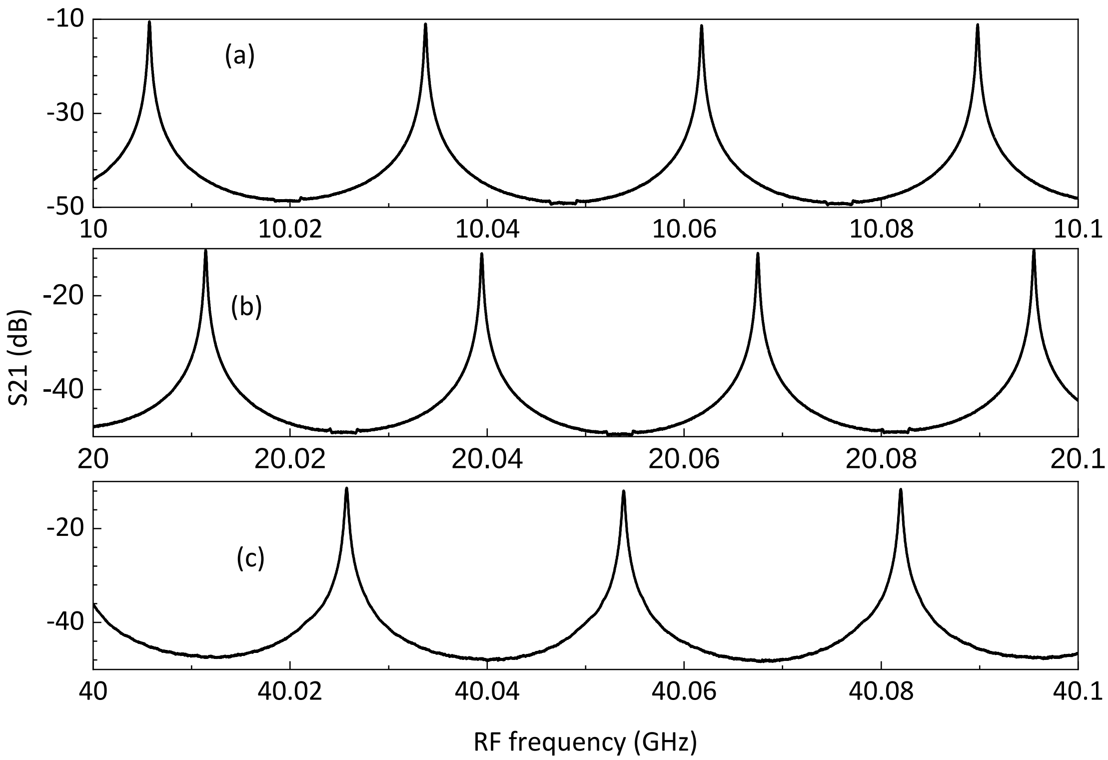

Figure 7.5 Amplitude transfer characteristics of the HCF-FP based MPF at 10 GHz (a), 20 GHz (b), and 40 GHz (c) over spans of 100 MHz.

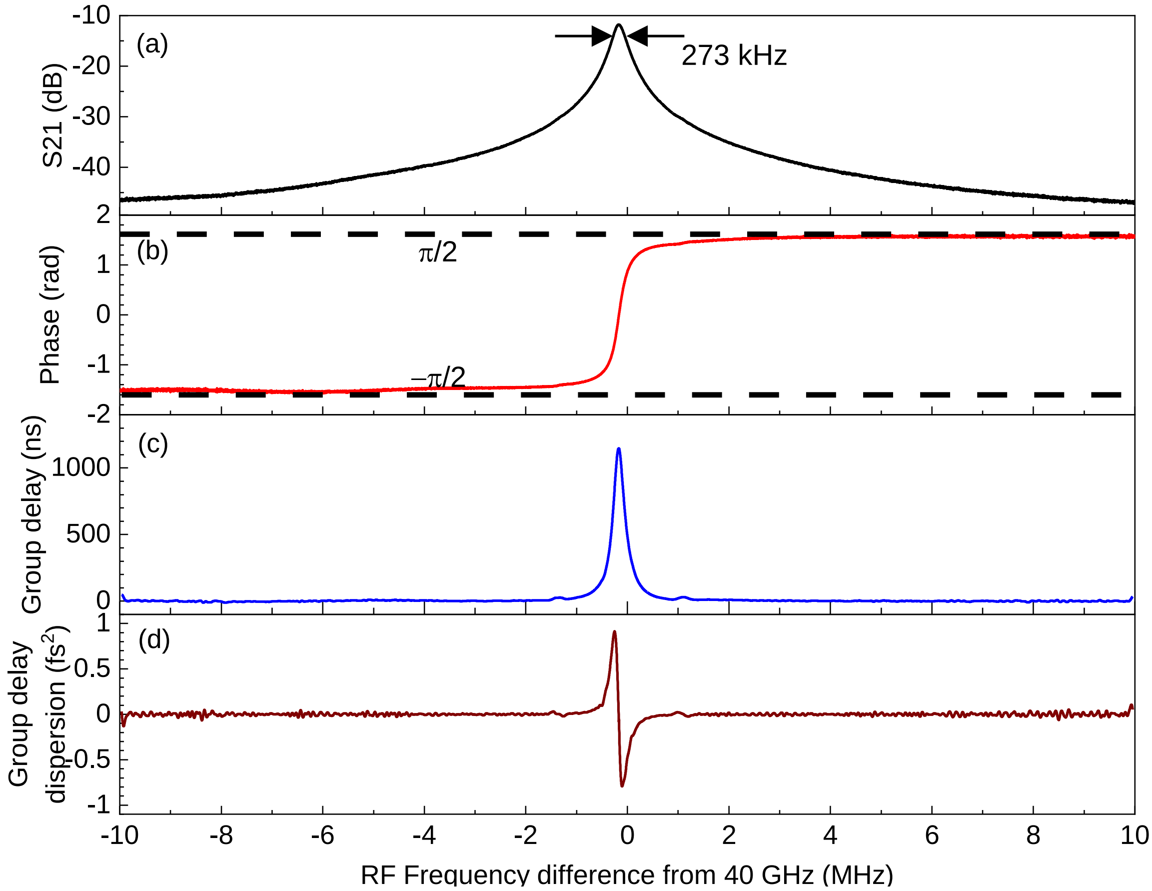

Figure 7.6 Detailed (a) amplitude, (b) phase response, (c) group delay and (d) group delay dispersion of the HCF-FP based MPF around 40 GHz RF frequency.

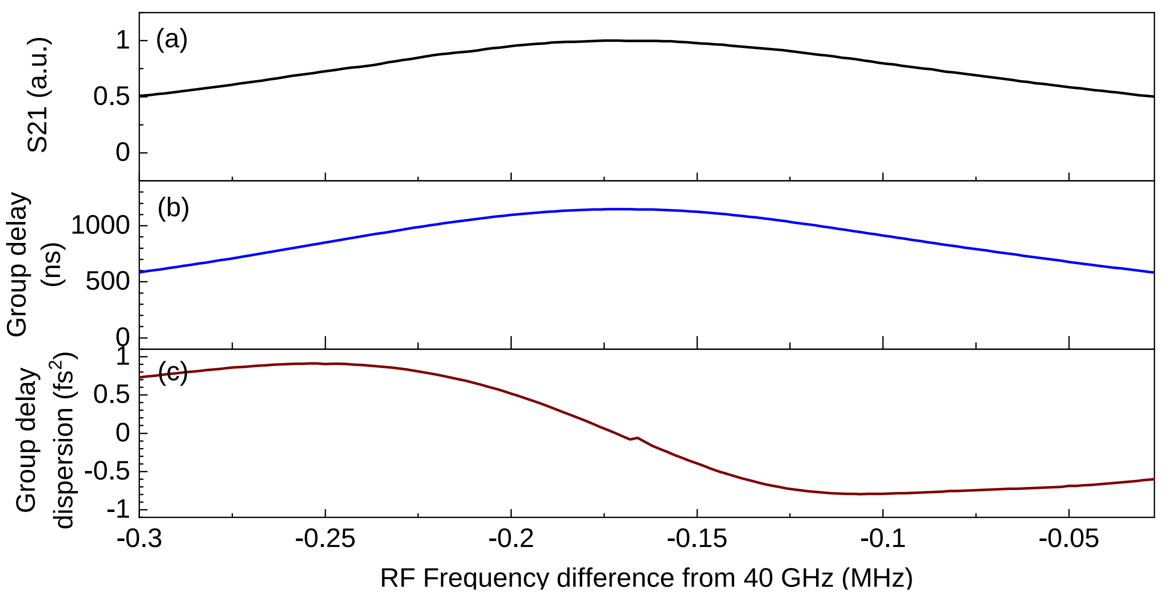

Figure 7.7 Detailed (a) amplitude, (b) group delay and (c) group delay dispersion of the HCF-FP based MPF within 3 dB transmission linewidth.

7.2.4 Filter temperature sensitivity

We placed the two FPs (based on HCF and SMF, respectively) into the same thermal chamber. Firstly, we stabilized the temperature and measured the filters' characteristics at frequencies of 10 GHz, 20 GHz and 40 GHz. Subsequently, we increased the temperature by 1 °C and repeated the measurement, as shown in Figure 7.8. The filter transmission peaks shifted in frequency. This shift was about 16 times larger for the SMF-FP based MPF than for HCF-FP based MPF. As expected, the shift also depends linearly on the central frequency: i.e., the shift at 40 GHz is 4 times larger than at 10 GHz).

To extract temperature sensitivity data with good accuracy and to confirm the shift in filter transmission characteristics is linear with temperature, we kept increasing the temperature in 1 K steps and measured the position of the transmission peaks. The filters transmission peak shifts (at 40 GHz, where the change is the largest) are shown in Figure 7.9. For SSMF-based filter, the transmission characteristics shift at a rate of 334 kHz/K while for the HCF-based filter the rate is only 21 kHz/K – a value almost 16 times lower as would be expected.

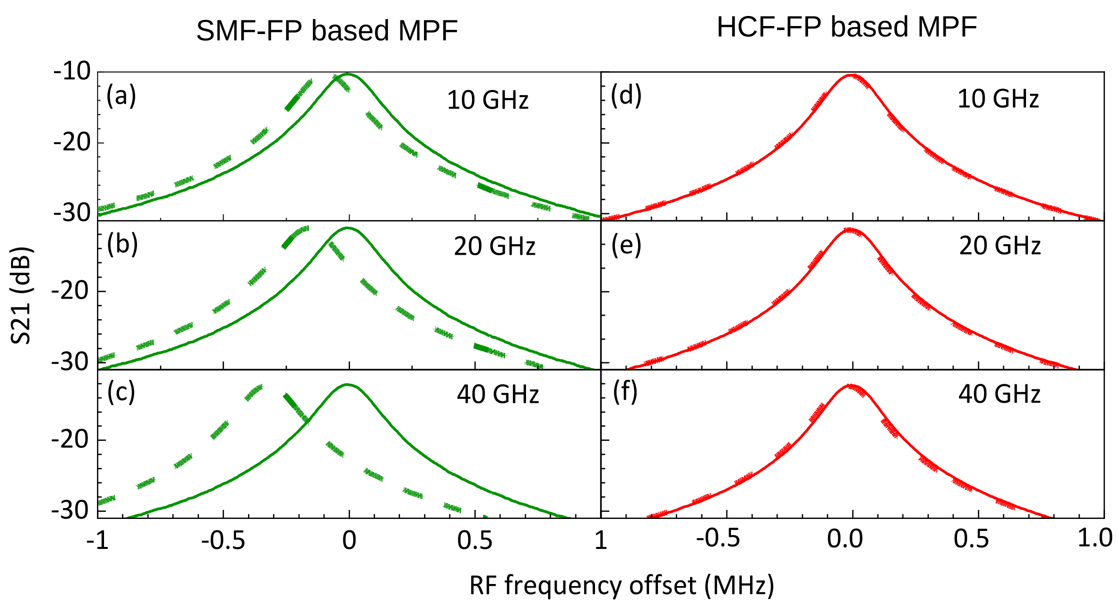

Figure 7.8 Transmission characteristics measured at 25 °C (solid) and 26 °C (dashed) for SMF-FP based MPF (a-c, red) and HCF-FP based MPF (d-f, green) measured at 10 GHz (a, d), 20 GHz (b, e), and 40 GHz (c,f).

We also measured the filters characteristics when subject to our air-conditioned lab environment (temperature variations of about 1 K due to the air-conditioning turning on and off). Within about an hour, the frequency variations for the SMF-FP based MPF were up to 480 kHz (at 40 GHz), while for the HCF-FP based MPF, they were less than 30 kHz, see Figure 7.10.

The results presented in Figure 7.10 show that the SMF-FP based bandpass filter operating at 40 GHz changes its central frequency (by up to 480 kHz) by more than is its bandwidth (3-dB bandwidth of 183 kHz), even in a temperature-controlled laboratory environment. On the other hand, an HCF-FP based MPF allows for accurate operation without any further environmental stabilization.

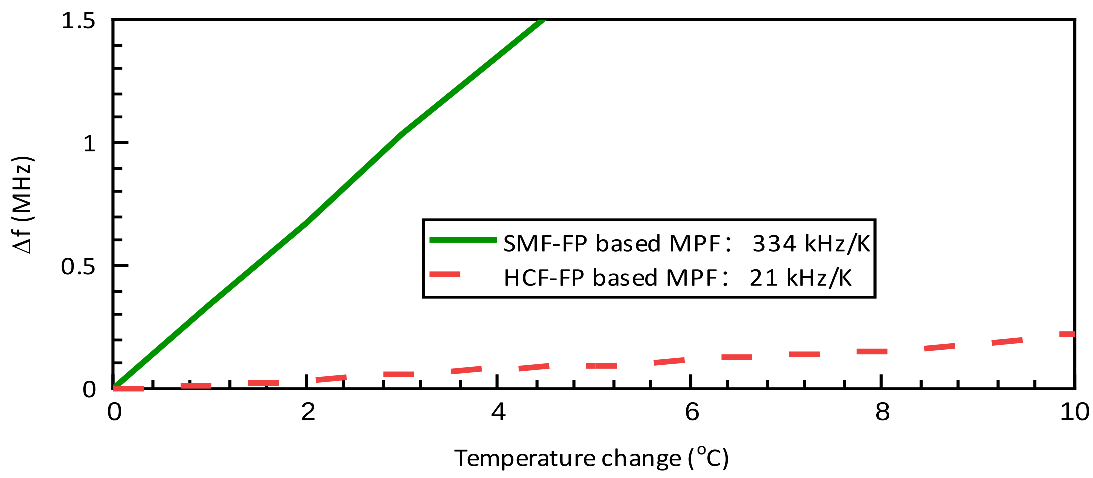

Figure 7.9 Filter characteristics frequency shift at 40 GHz over 10 K temperature change for HCF-FP based MPF (dashed, red) and SMF-FP based MPF (solid, green).

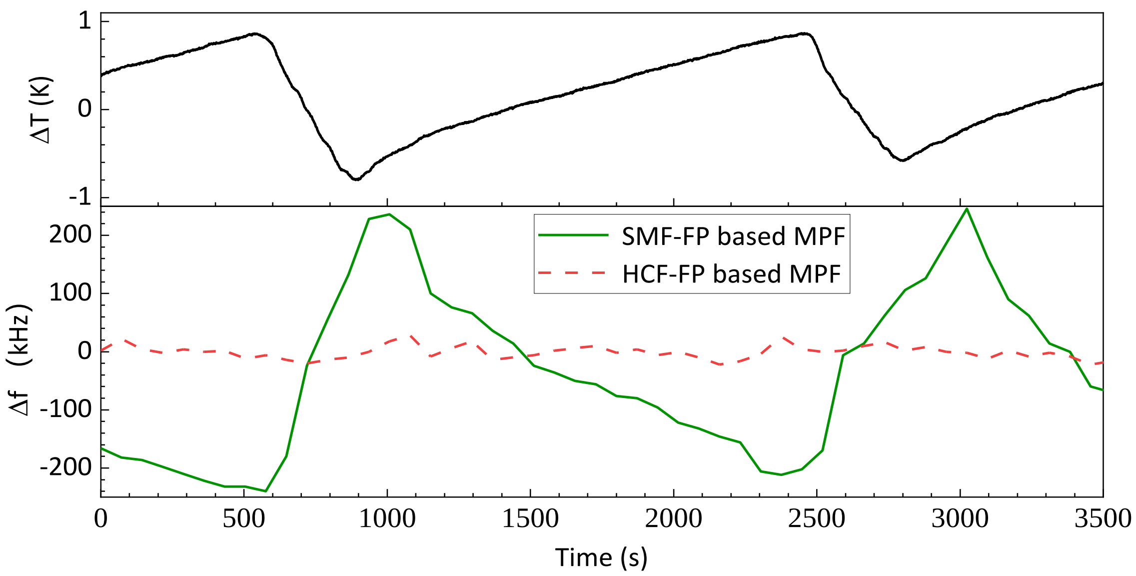

Figure 7.10 Temperature variations ΔT in the laboratory and measured transmission peak frequency variations Δf for HCF-FP (solid, green) and SMF-FP based (dashed, red) MPFs when subject to laboratory environment over 1 hour.

To ensure that the transmission peak frequency does not change by more than 10% of its 3-dB bandwidth, the SMF-FP based MPF (temperature shift of 334 kHz/K, Figure 7.9) requires temperature stabilization better than 0.05 °C, which is rather impractical. On the other hand, the

HCF-FP based MPF (21 kHz/K, Figure 7.9) requires temperature stabilization of just 0.9 °C, easily achievable with simple temperature control. These requirements could be relaxed if the filter is operated at a lower frequency (e.g., at 10 GHz, four times larger temperature variations are acceptable), or with a larger bandwidth. However, if a lower bandwidth is targeted (e.g., in our work in section 5.2.4, we presented a FP fibre etalon with 10 times narrower transmission peaks than presented here), the temperature stabilization needs to be improved, rendering an MPF made of SMF unstable and needing impractical mK-level temperature stabilization.

From the temperature-induced shifts given earlier (334 kHz/°C and 21 kHz/°C, Figure 7.9), the normalised time delay thermal sensitivity of the used fibres (NANF hollow core fibre and SMF) can be calculated by:

$$D_{\tau} = -\frac{df_{peak}/dT}{f_{peak}} \tag{7.7}$$

Here, f_{peak} indicates the measured transmission peak frequency of the filter. From our data and Equation (7.7) we calculated a thermal sensitivity of 8.4 ppm/°C (SMF) and 0.5 ppm/°C (NANF). Considering the thermal sensitivity is mostly due to fibres' thermal sensitivity, the measured values agree well as reported in [14].

7.3 Summary

In conclusion, we firstly developed a technique to measure hollow core fibre (HCF) loss very precisely. The technique enables us to measure HCF loss with a relatively short sample (metres to 100s of metres). This can be very useful especially for characterization of HCF loss. Long length HCF is coiled on a drum, leading to a micro bending loss. Thus, measuring loss of a fibre with a short piece can be helpful especially for development of HCFs. It can help us to measure HCF's loss at the start of pull (SOP) and the end of pull (EOP)[22].

To demonstrate the importance of the fibre thermal sensitivity in microwave photonics, we built two microwave photonics filters (MPFs) based on all-fibred Fabry-Perot interferometers. The first one was made of a single mode fibre (SMF), while the other one was made of low-thermally-sensitive HCF. Compared to the SMF- FP based MPF, the HCF-FP based MPF changes its transmission peak frequency almost 16 times less with temperature. As a result, the HCF-FP based MPF is stable under laboratory conditions, and in real world applications would require only simple temperature control, while a SMF-FP based MPF would require impractically accurate/tight temperature control levels of 0.05 °C.

This microwave photonics filter experiment here is just a proof of principle experiment to show HCF's advantages in microwave photonics. It still has some room to improve. For example, the HCF-FP based MPF shows a very small periodicity in transmission characteristics, but this may improve by using two HCF-FP with similar length (Vernier effect, see [171]) or making HCF-FPs with short length e.g., several cm, to increase the FSR of the transmission peaks in the future. Despite this, the experiments we have presented represent the first demonstration of the latest generation of HCF, i.e., NANF, in microwave photonics.

Part of this work was published in [172].

Chapter 8 Further improvement of Hollow core fibre based Fabry-Perot thermal stability

Although we have demonstrated in section 6.2.3 that HCF-FPs already have a thermal sensitivity about 16 times lower than SMF-FPs of the same optical length, it is desirable to reduce it even further. Several methods, e.g., making uncoated HCF working at -71 °C or operating an open HCF at 110 °C, as described in section 3.4.4, have been reported, but none of them operates at room temperature. However, for many applications, operation at or close to room temperature is desired. In this chapter, I will show a new method that can reduce HCF's thermal sensitivity at room temperature.

8.1 Principle of operation

As the thermal sensitivity of HCF is mostly given by the CTE of silica glass as described in section 3.4.4, reducing the thermal sensitivity of HCF-FP requires a reduction in the thermally-induced expansion of the HCF. Before talking about our method in detail, let us first analyse a situation in which a string is fixed to a temperature insensitive support at both ends, as shown in Figure 8.1.

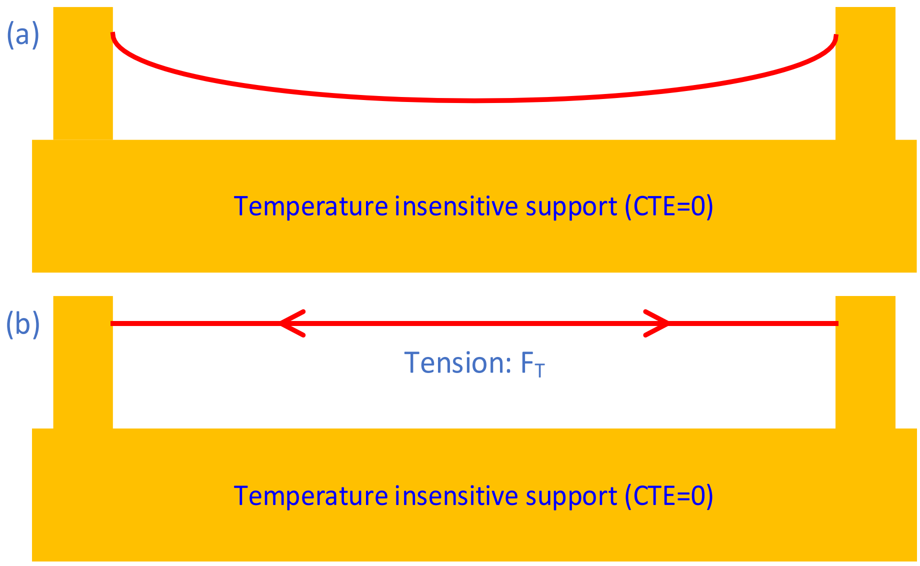

Figure 8.1 A string is fixed to a temperature insensitive support at both ends at (a) a loose state and (b) stretched with a tension.

As the temperature increases, the length of a loose string (Figure 8.1(a)) will expand freely; however, when the string is pre-stretched with a tension and then fixed to the support, the increasing temperature only reduces the tension (due to temperature-induced elongation of the string, which then requires less force to keep it in the original elongated state). In the meantime, the string maintains its length. This keeps the string straight (under tension) as long as the heat-induced string elongation is smaller than the initial pre-stretch.

Fixing HCF straight (Figure 8.1 (b)) to a temperature insensitive material is impractical, but the same effect can be achieved by coiling the HCF under tension on a spool that has a zero CTE, Figure 8.2. In our demonstration, we use Zerodur from Schott, but there are several other materials with similar properties, e.g., ULE glass from Corning, ZERØ from Nippon, or IC-ZX from Shinhokoku. With increasing temperature, the spool maintains its size, forcing the HCF to maintain its length as well. The heating would have elongated a freely coiled HCF, but as it is under a stretch, it only reduces the tensile force, meaning the length is fully-dictated by the spool size. In this way, the CTE of the HCF should be identical to the CTE of the spool. Silica glass from which HCF is made has CTE = 3×10^{-7}/°C [89], meaning that a 100 K temperature change would change its length by 0.003%. Fibres can be stretched significantly more (usually proof-tested at 0.5 or 1%), making our technique applicable over a very broad temperature range. Besides, the associated glass refractive index change through the stress-optic effect has negligible influence on the light guided through the HCF thanks to its propagation mostly through the air-filled core rather than the silica glass, which makes the CTE of the spool the only contributor to the thermal sensitivity of the HCF.

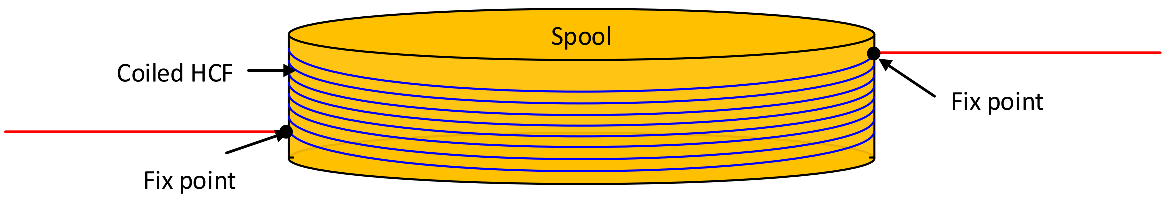

Figure 8.2 Schematic of the HCF coiled to a spool with zero CTE.

8.2 Simulations

In practice, there are several aspects that may reduce the effectiveness of this method. The most important is the coating that has very different mechanical and thermal properties to the glass and which will serve as a “cushion” between the spool and the glass fibre. To understand these effects, we performed the simulation with COMSOL Multiphysics.

We used a 2D axisymmetric model with the geometry shown in Figure 8.3. We neglect the mechanical properties of the HCF microstructure, approximating the HCF as a capillary. We consider it to be coated with a single acrylate coating. A contact boundary is applied between the HCF’s outer surface and the spool. A body load in the direction of the spool centre is applied to the HCF to simulate the effect of the stretching tension. For a spool radius R, the relationship between the body load F_L and the stretching tension F_T is:

$$F_L = -\frac{F_T}{R} \tag{8.1}$$

In our simulations, we consider the spool to be made of Zerodur (Young's modulus 90.3 GPa), HCF of inner/outer diameter of 70/186 μm, made of silica (Young's modulus of 73.1 GPa and CTE = 0.3 ppm/K [89]), and coating with a thickness of 10 μm (Young's modulus of 35 MPa and CTE = 180 ppm/K [173]).

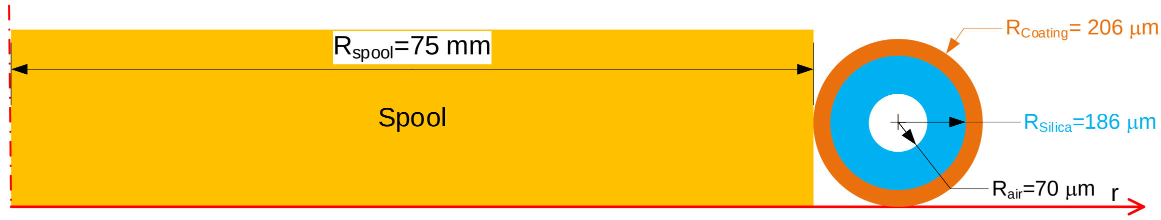

Figure 8.3 the 2D axisymmetric model in COMSOL Multiphysics (not to scale as the spool is significantly larger than the HCF).

Firstly, we studied the influence of the HCF coating thickness. We considered a spool with R=75 mm and coating thickness of either 0 μm (bare HCF), 10 μm (thinly-coated HCF presented in [89] and used in our experiments), and 50 μm (typical thickness used, e.g., in [88]). As shown in Figure 8.4, the uncoated and uncoiled HCF is expected to have a thermal sensitivity of 0.3 ppm/°C, corresponding to the silica glass CTE. When coiled on the CTE = 0 spool, its thermal sensitivity is almost eliminated, in line with our expectations. For the uncoiled thinly-coated HCF, the coating slightly increases the HCF thermal sensitivity due to the significantly larger CTE of the coating relative to the silica glass. Thanks to the relatively low coating material stiffness (low Young's modulus) and small thickness, its effect on the overall HCF thermal sensitivity is very small, increasing the HCF thermal sensitivity by 0.05 ppm/K only. When coiled on the CTE = 0 spool, the HCF thermal sensitivity is strongly reduced, but it does not reach zero like for the uncoated HCF. However, the seven-fold reduction predicted is still significant. For the standard-thickness coated HCF, the thermal sensitivity of the uncoiled HCF is relatively strongly influenced by the coating, increasing it ~1.5 times. When coiled on the CTE = 0 spool, the thermal sensitivity is reduced as in the previous two cases, but only by a factor of two.

Bare fibre is impractical (fragile) and standard-coated HCF (50 μm coating) does not show significant improvement when coiled on the CTE = 0 spool. Thus, with further simulations (and subsequent experimental demonstration) we focus on the thinly-coated HCFs.

Firstly, we analyse how the coiled HCF thermal sensitivity changes with the HCF pre-stretching. By varying the pre-stretch force between 0 and 2 N we found that the HCF thermal sensitivity is virtually insensitive to the pre-stretching. In the following simulations, we set this parameter to 0.5 N.

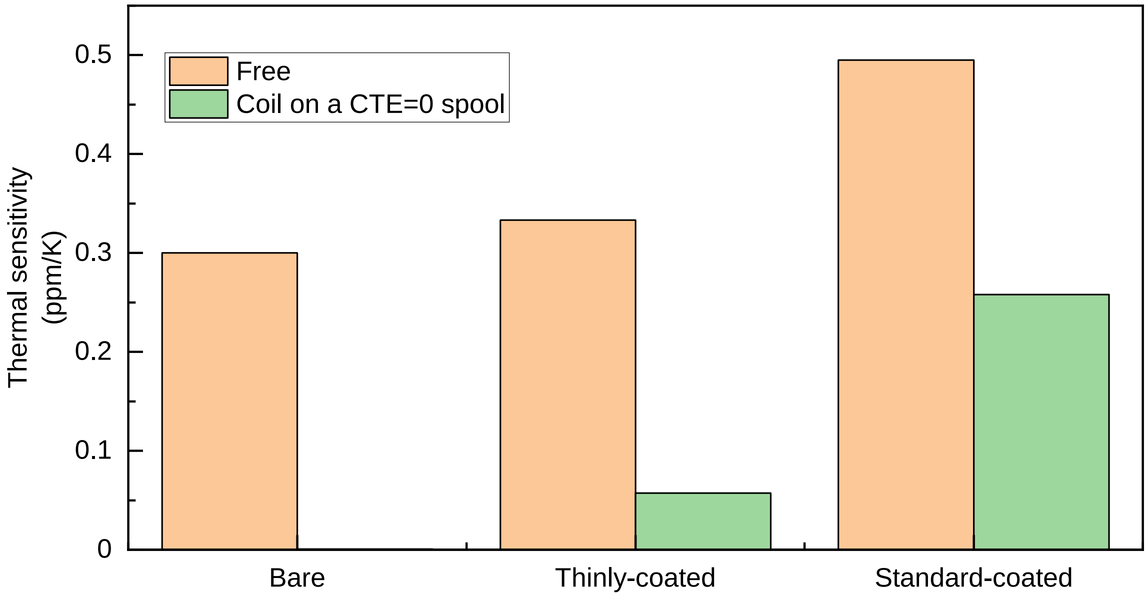

Figure 8.4 Thermal sensitivity calculated for free HCFs (yellow) and coiled HCFs (green) with different coating thickness (Bare, 0 mm; Thinly-coated, 10 μm; and Standard-coated, 50 μm).

Further simulations revealed rather non-intuitive behaviours. Firstly, the thermal sensitivity of the coiled HCF did not change significantly with the HCF silica thickness, while for an uncoiled HCF, thicker silica glass reduces the influence of the coating on the thermal sensitivity, Figure 8.5.

Further, we found that the Young's modulus of the coating had almost no influence on the thermal sensitivity of the coiled HCF, while its CTE did, Figure 8.6. This is very different to uncoiled HCFs, where the CTE × Young's modulus product influences the HCF thermal sensitivity as shown in Equation (3.20). This suggests that the CTE = 0 coiled HCF should have a coating with small CTE, irrespective of its Young's modulus. A candidate for such a coating is polyimide [173] used as fibre coating for high-temperature applications. In particular, Novastrat905 polyimide from NeXolve has a CTE close to 0 ppm/^{o}C.

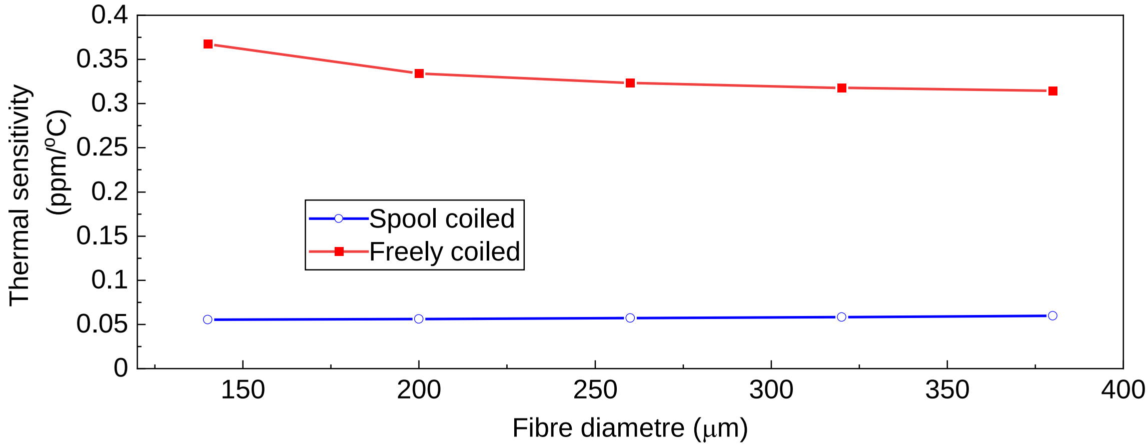

Figure 8.5 Thermal sensitivity of coiled HCF with respect to the fibre diameter and its comparison to free HCFs.

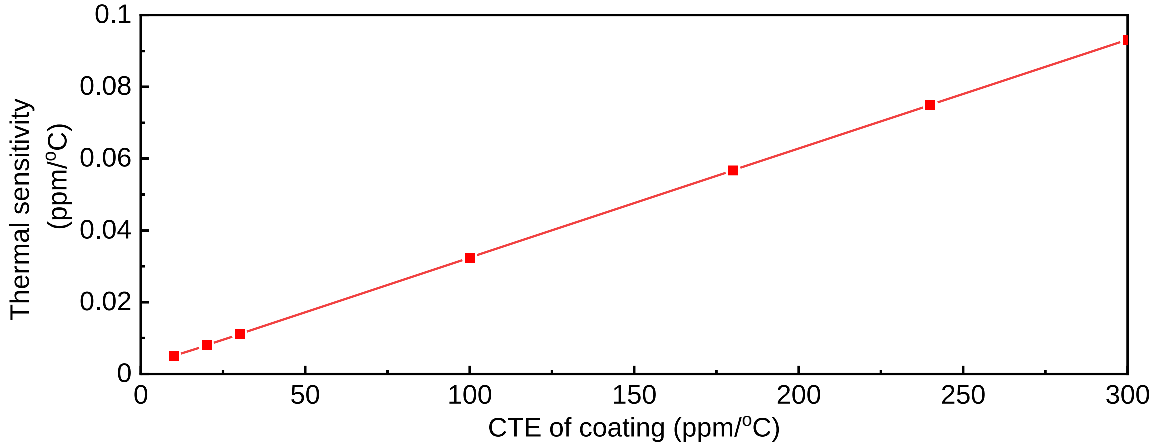

Figure 8.6 Thermal sensitivity of coiled HCF with respect to coating CTE.

Finally, we studied how the coiled HCF thermal sensitivity changes with the CTE of the spool material and the spool radius. Figure 8.7 shows results for a CTE between -0.1 and 0 ppm/°C, which is within the CTE range specified by Zerodur or ULE manufacturers (<± 0.1 ppm/°C [27,30]). As expected, lower spool material CTE means a lower thermal sensitivity of the coiled HCF. A smaller spool radius gives a larger thermal sensitivity, suggesting a design rule for thermally-insensitive coiled HCFs. Firstly, we should target spools with a CTE between -0.1 and -0.05 ppm/°C. Once the spool CTE is known, the spool diameter can be set to ensure zero-sensitivity coiled HCF (e.g., in Figure 8.7, R = 44 mm gives zero HCF thermal sensitivity for a spool with CTE = -0.1 ppm/°C, as does R = 82 mm for CTE = -0.05 ppm/°C). Further fine tuning can be achieved by drilling a hole in the centre of the spool, as this reduces its stiffness. This is shown in Figure 8.8, where a coiled HCF thermal sensitivity of -0.0025 ppm/°C for a homogenous Zerodur spool with CTE = -0.05 ppm/°C and R = 90 mm is tuned to zero sensitivity when a hole of 87 mm is drilled in the middle of the spool. However, this tuning is very small. By drilling a hole of a diameter of 88.5 mm which means the wall thickness is just 1.5 mm, the thermal sensitivity is just tuned to 0.0025 ppm/°C from -0.0025 ppm/°C (a change of 0.005 ppm/°C). This means that the coiled HCF thermal sensitivity is not very sensitive to hole size, which means that in the future we can drill a hole to the spool and make the system light.

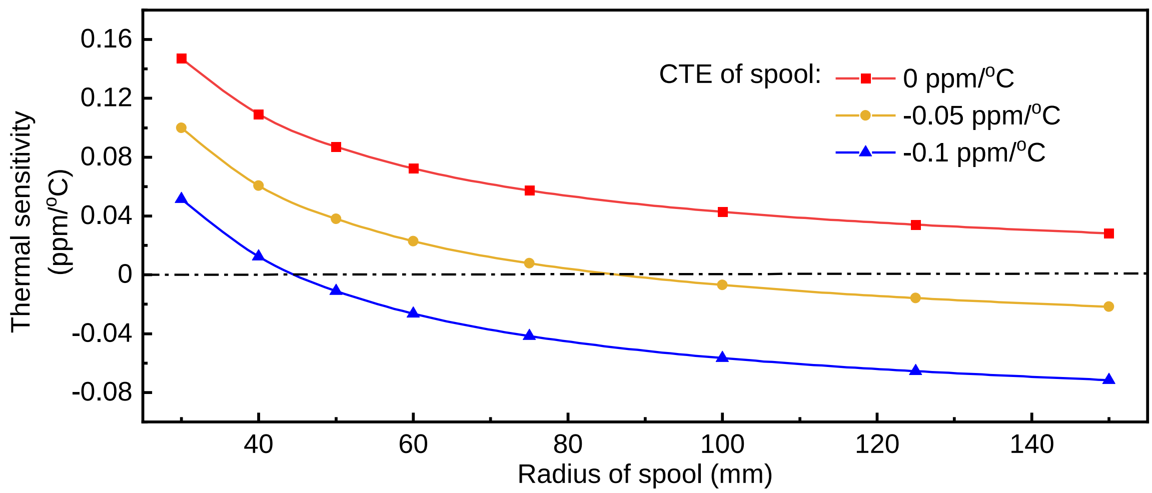

Figure 8.7 Thermal sensitivity of coiled HCF with respect to the radius at different spool CTE values.

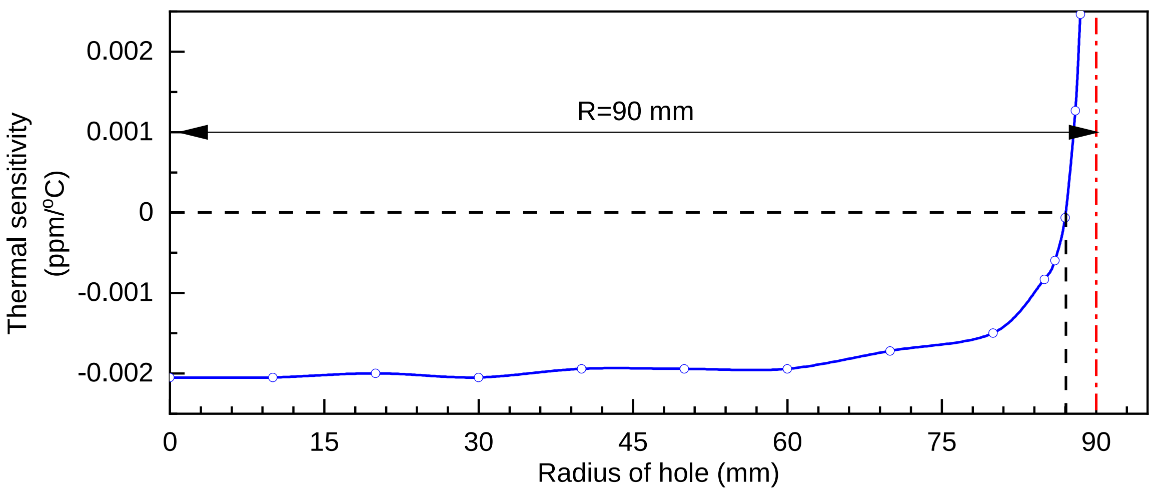

Figure 8.8 Thermal sensitivity of coiled HCF on spool with CTE of -0.05 ppm/°C with respect to the central hole radius for spool with R = 90 mm.

8.3 Experiments

To demonstrate our method experimentally, we used a Zerodur cylinder with R = 75 mm that was salvaged from an old mirror, and a thinly-coated HCF (10 µm coating thickness) with an outer diameter of 206 µm [89]. As a proof of principle experiment, we didn't use the high-finesse HCF-FP but preparing HCF-FP by splicing the thinly-coated HCF with SMFs at both ends with a piece of GRIN fibre as a mode adapter. At the HCF end-facets, there is 4% Fresnel reflection, as light travels from the solid glass core to the hollow core, forming the FP. Two HCF samples were prepared: one coiled on Zerodur (fixed on the Zerodur spool with Capton tape), and one freely-coiled. The HCF samples were each spliced with two mode-field adapters and SMF pigtails as described in [97]. The lengths of these two HCF-FPs were measured by measuring their FSR using the method described in 4.1. The RF spectra are shown in Figure 8.9. Their FSR were measured to be 30.69 MHz and 34.38 MHz, corresponding to lengths of 4.89 m and 4.36 m, respectively for Zerodur-coiled and freely-coiled HCF-FP.

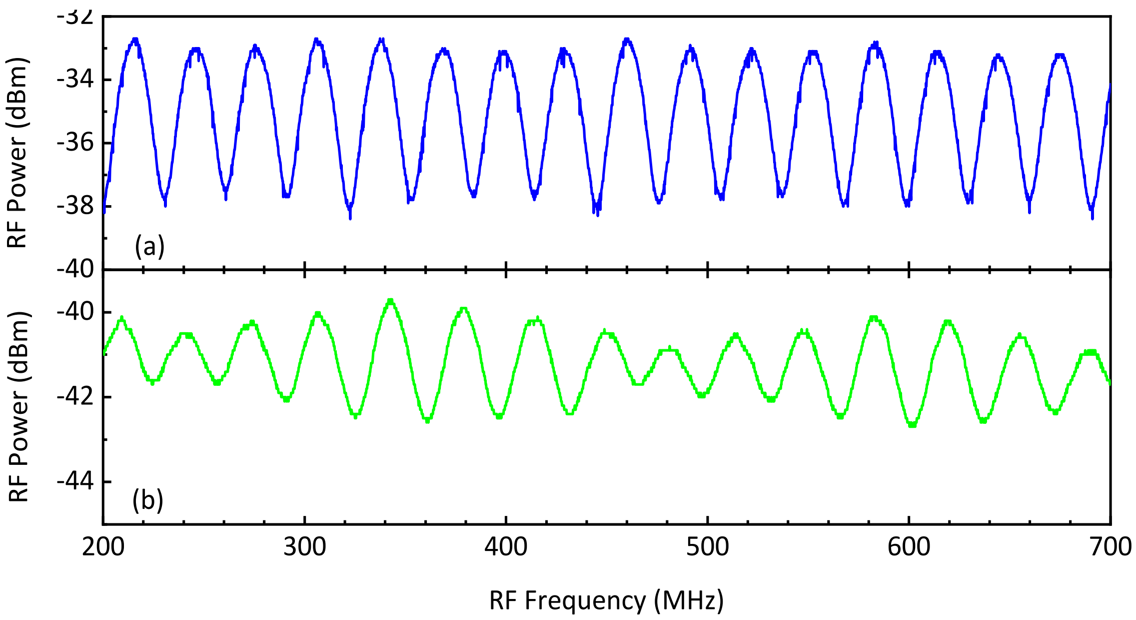

Figure 8.9 The RF spectra of the two HCF-FPs, (a) Zerodur-coiled and (b) freely-coiled.

The characterization set-up is shown in Figure 8.10. Both HCF samples were put into a thermal chamber. The signal was then split in two to enable probing of both interferometers at the same time. The HCF-FP signals were observed in reflection (retrieved via two circulators), which gives better interference contrast in a low-finesse FP than the transmitted signal.

The thermal chamber temperature was changed between 25 and 55°C. Figure 8.11 shows how the reflection changed as a function of temperature for both HCF-FPIs. Each extremum corresponds to a phase change of $\pi/2$ and the thermal phase change can then be calculated by counting these extrema (N extrema) observed

$$\Delta\Phi = N_{extreme} \cdot \frac{\pi}{2} . \tag{8.2}$$

The thermal sensitivity over a temperature change of ΔT can be calculated by

$$S_{\phi} = \frac{1}{\phi}\frac{\Delta\phi}{\Delta T} = \frac{N_{extreme} \cdot \lambda}{4 \cdot \Delta T \cdot L} \tag{8.3}$$

where L is the HCF length.

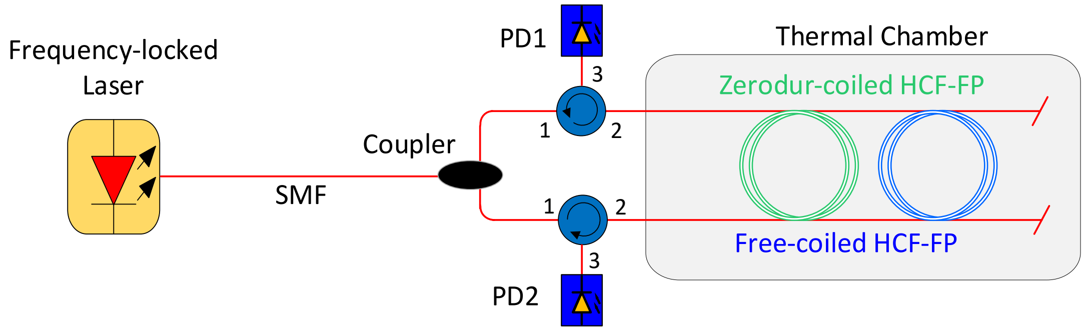

Figure 8.10 Thermal sensitivity measurement setup using the Zerodur-coiled and freely-coiled HCF-FPs.

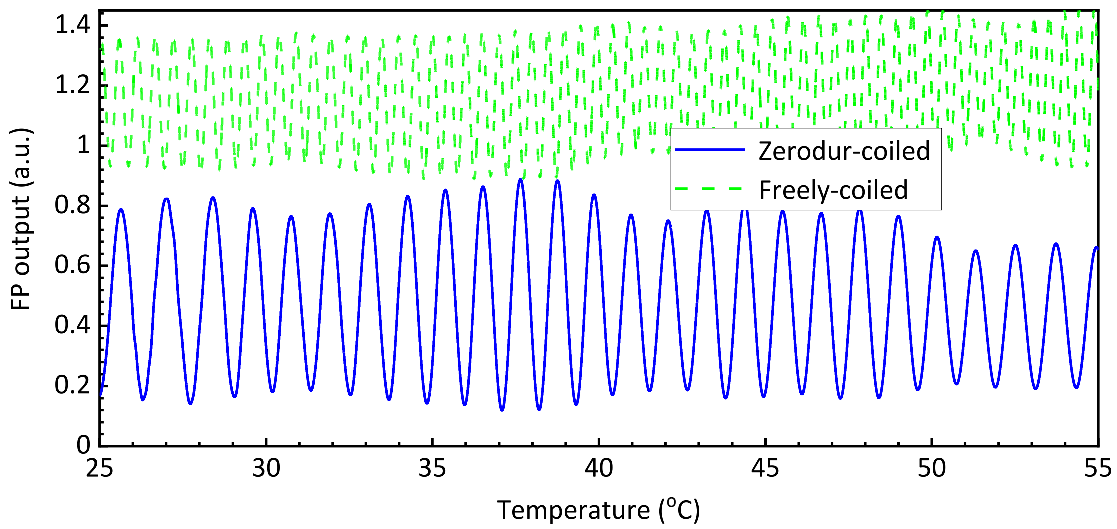

Figure 8.11 Example measurement of transmission through Zerodur-coiled HCF and free-coiled HCF when temperature is changed.

The resulting phase changes and thermal sensitivities are shown in Figure 8.12 and Figure 8.13. The result obtained for freely-coiled HCF-FP compares well to that simulated, also shown in Figure 8.13. For the Zerodur-coiled HCF-FP, we also get good agreement with simulations (also shown in Figure 8.13) when we assume a Zerodur CTE of 0.07 ppm/°C, which is within the manufacturer specification of <±0.1 ppm/°C [27].

Our experimental results show an improvement of the Zerodur-coiled HCF-FP compared to the freely-coiled embodiment by a factor of three. However, from simulations we expect improvements by up to 7 times when using a coil with CTE = 0 and fully-insensitive HCF-FP when selecting Zerodur with CTE = -0.06 ppm/°C, which is within its specifications. Zerodur with selected specific CTE can be purchased from the manufacturer. Thus, to better improve the performance a new Zerodur spool has to be purchased, ideally with a CTE of -0.06 ppm/°C.

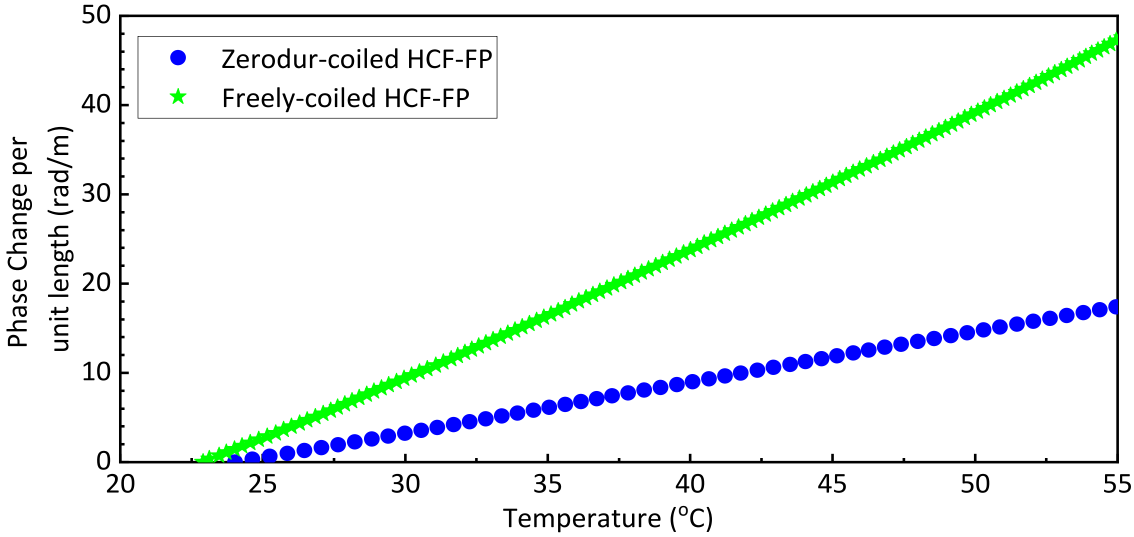

Figure 8.12 Phase change per unit length of Zerodur-coiled and freely-coiled HCF-FP.

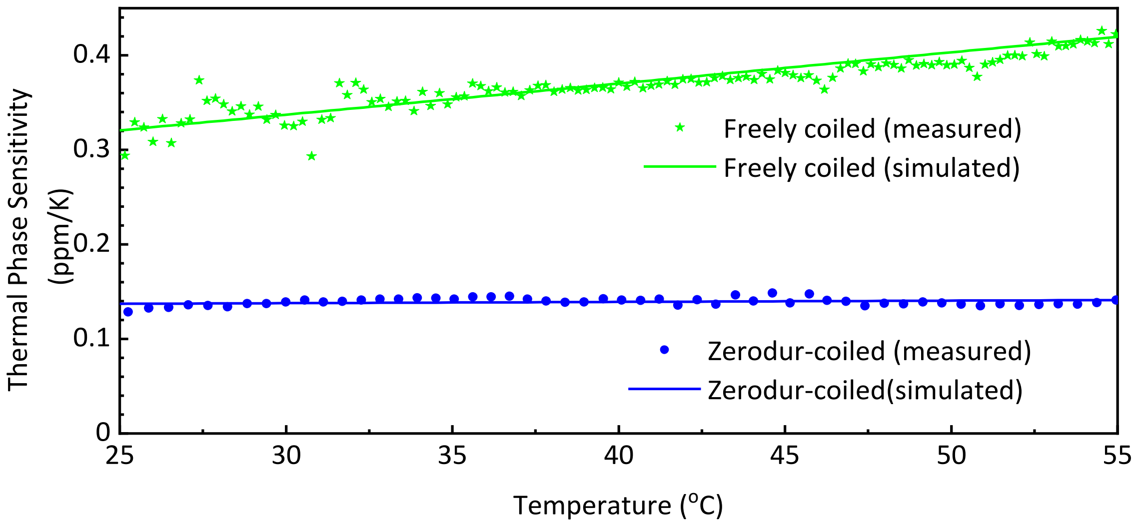

Figure 8.13 Measured and simulated thermal sensitivities of Zerodur-coiled and free-coiled HCF. Simulations considered Zerodur CTE of 0.07 ppm/K.

8.4 Summary

We analysed a new method of achieving HCF-FPs with low and potentially even zero sensitivity to temperature. Due to the HCF coating, zero thermal sensitivity requires a spool made of a material with negative CTE. Thinly-coated HCFs require a spool with only very small negative CTE (-0.1 to -0.05 ppm/°C), which is available commercially (e.g., selected Zerodur or ULE materials). The HCF-FP thermal sensitivity can be also slightly tuned by controlling the spool size and its central hole diameters, offering avenues to fine-tune the thermal sensitivity, potentially to zero sensitivity.

In our experimental demonstration we achieved a reduction of HCF-FP thermal sensitivity by a factor of three, most probably limited by the CTE of the available spool. Even though we plan to further reduce its thermal sensitivity by using optimized spools, the achieved thermal sensitivity of 0.13 ppm/^{o}C is three times lower than the lowest value so far achieved at room temperature for any fibre FP. Finally, we would like to mention that the proposed method can be used in any optical fibre interferometer configuration.

It is also noted although we did not test here, we expect that the coiled HCF's loss would increase as the fibre is coiled to a rigid body [73]. In the future, we may test this by coiling a high-finesse HCF-FP to the Zerodur spool and test how the finesse change by coiling. Further optimisation may require a proper design of coating [73].

This work was published in [174].

Chapter 9 Conclusions and future works

9.1 Conclusions

This thesis has focused on research into long-length and high-finesse hollow core fibre based Fabry-Perot interferometers (HCF-FPs). Several aspects necessary for realization of HCF-FPs have been covered, in particular, a new method to characterise long-length FPs, study of finesse limitation of HCF-FPs, realisation of sealed, alignment-free all-fibred HCF-FPs, and further improvement of thermal stability of HCF-FPs.

To monitor long-length HCF-FPs in real time during the fabrication process, we proposed and developed a technique to characterise a long-length FP by using an incoherent broadband source and an RF spectrum analyser. The basic idea of the method is that when filtered by an FP, a broadband optical source forms an incoherent comb which carries the information of the FP parameters. The beating signal of the incoherent comb was then analysed with an RF spectrum analyser, revealing the parameters, i.e., finesse and free spectral range of the FP. The method enables us to obtain fast feedback when aligning the mirrors of HCF-FPs, which is the key to aligning high-finesse HCF-FPs.

Finesse limitation of HCF-FPs was then analysed both theoretically and experimentally. The coupling loss between the HCF and the mirror set the ultimate limitation of the finesse of HCF-FPs. We analysed theoretically how mirror tilt, distance between the HCF and the mirror, HCF cleave angle, and attenuation of the state-of-the-art HCFs influence the coupling loss. Followed by construction of several HCF-FPs with lengths between 0.65 m and 9.25 m. Combining the experimental results and theoretical analysis, we concluded that the coupling loss between HCF and the mirror was better than 0.0028 dB (corresponding to 99.94% of the light being coupled back into the HCF). This coupling loss could enable a finesse over 5 000 of an HCF-FP. Experimentally, we achieved a finesse of 2 400 with the 65-cm sample, which was limited by the available mirrors used in the experiment. Nevertheless, being about 2 times smaller than that achievable, it is already almost 30 times higher than that achieved previously [10]. We published this work in [166]. The finesse we demonstrated here can be an important reference for future HCF-FPs based applications.

To make HCF-FPs that can be used in long-term applications without alignment (once fabricated), we also made two HCF-FPs interconnected with single mode fibre in collaboration of colleagues from Czech Technical University in Prague. This was enabled by combination of their standard single mode fibre to HCF interconnection technology [107] and the real-time HCF-FP characterisation method we developed. The two HCF-FPs made had lengths about 5 m and 23 m respectively. The HCF was connected to mirrored single mode fibre by gluing. The glue also sealed the HCF-FP cavity, making it immune to the air/dust pollution thus suitable for long-term application. Although we observed a finesse degeneration during the glue curing process, we achieved finesse >120 over the entire C band with the fully assembled permanent-connection based HCF-FPs, which represents the first demonstration of all-fibred long-length HCF-FPs with such a high finesse. We have tested the 23-m HCF-FP 2 years after it was fabricated, and confirmed its finesse did not degrade from the time it was made. To the best of our knowledge, this is the demonstration of HCF-FPs that can be used in long-term. We published this work in [169].

To demonstrate HCF-FPs' advantages over other FP embodiments, we measured the 5-m HCF-FP's thermal response with a 3.4-m single mode fibre based FP (SMF-FP) which has the same optical length as the 5-m HCF-FP. The results have shown that the thermal sensitivity of phase change in the measured HCF-FP was 0.57 ppm/^{o}C while in the SMF-FP, it was 8.3 ppm/^{o}C, showing that the thermal sensitivity of HCF-FPs was about 15 times lower than that of SMF-FPs.

The low thermal sensitivity of HCF-FPs makes them of interest in many temperature-sensitive applications. As an example, in this thesis, we used the 5-m HCF-FP to build a microwave photonics filter. The performance was compared to the 3.4-m SMF-FP based microwave photonics filter. Compared to the SMF-based filters, the HCF-based filter changed its central frequency almost 16 times less with temperature. As a result, the HCF-based filter is stable under laboratory conditions, and in real world applications would require only simple temperature control, while the SMF-based filter would require impractically accurate/tight temperature control. This represents the first time that hollow core fibre was used in microwave photonics filters. This part of work was published in [172] .

Although HCF-FPs have shown a 15-16 times lower thermal sensitivity than SMF-FPs, further improvement would be beneficial. To achieve this goal at room temperature, we suggested and demonstrated a new method in which we coiled an HCF-FP under tension to a temperature-insensitive spool (Zerodur from Schott). Compared to the freely-coiled HCF-FP, we improved the HCF-FP's thermal sensitivity by a factor of 3. In this proof-of-principle experiment, we achieved a thermal sensitivity of 0.14 ppm/^{o}C is already the lowest value of any fibre-based FP at room temperature. Our simulations showed that the current thermal sensitivity was limited by the used Zerodur whose coefficient of thermal expansion was estimated in our experiment to be 0.07 ppm/^{o}C. By using a material with slightly negative coefficient of thermal expansion, HCF-FP with thermal sensitivity reaching 0 ppm/^{o}C could be achieved according to our simulations. The simulations also show that the thermal sensitivity of the spool coiled HCF changes with the spool size, i.e., the spool diameter and thickness, which gives us avenues to fine-tune the thermal sensitivity close to zero. This part of work was published in [174].

9.2 Future works

We have carried out systematic research on HCF-FPs, e.g., we found finesse limitation due to HCF-mirror loss, we built the first all-fibred HCF-FP that has HCF sealed and thus can be used in long-term, and analysed a strategy how to eliminate the HCF-FP's thermal sensitivity. However, further work may be necessary to further improve their performance.

When making the all-fibred HCF-FP, we have observed its finesse had degraded while gluing the mirrors. Thus, gluing process may need to be further improved to reduce the degradation. We have used flat mirrors to make HCF-FPs, however, a concaved mirror might reduce HCF-mirror coupling loss and thus improve achievable finesse and reduce the insertion loss. By using a concave mirror as the cavity mirror, a gap can be kept between HCF and the mirror without degrading the finesse, making such an HCF-FP also suitable for applications in gas photonics.

Moving forward, more applications, for example, in gas photonics based on the developed HCF-FPs can be undertaken. An example is detection of gases such as carbon dioxide by cavity ring down spectroscopy. Although there was a report by using cavity ring down spectroscopy to detect gases in an HCF-FP, the sensitivity was just 1×10^{-5} cm^{-1} limited by the finesse of the used HCF-FP of four only [8]. We believe that by using our HCF-FP with high finesse, the measurement sensitivity can be improved by several orders of magnitude. Additionally, many other cavity enhanced sensors can benefit from the high finesse demonstrated in this thesis. For example, in cavity enhanced Raman spectroscopy, the power inside the cavity can be built up by several orders of magnitude, thus increasing the power of Raman signal by several orders. This will increase the measurement sensitivity of gas sensors. In cavity enhanced photothermal spectroscopy, a pump laser which is absorbed by the gas molecules forming optical phase modulation inside the cavity and then a probe laser is used to detect the phase modulation. By operating the pump and probe laser around the resonances of an HCF-FP, both phase modulation and detection are proportional to cavity finesse. A finesse around 3000 with a length around 40 cm would enable photothermal sensors achieve a measurement sensitivity down to part-per-quadrillion level [138], which is three orders of improvement of the current photothermal sensors.

Following the simulations in Chapter 8, the thermal sensitivity of HCF can be further reduced even to zero with a spool with slightly negative thermal expansion coefficient. This work will be further conducted by my colleagues. The HCF-FP we used in Chapter 8 is formed by splicing solid core fibres to a piece of HCF at its both ends. Further analysis on how the coiling influence the finesse of a high-finesse HCF-FP may be taken. Once a zero thermal sensitivity of HCF-FP at room temperature is achieved, a laser could be locked to the HCF-FP to make an ultra-stable laser.

Apart from the low thermal sensitivity, HCF-FP also have other advantages, e.g., low nonlinear effects. This property leads to HCF-FP's utilisation in nonlinear effects limited applications. For example, it has been shown that by locking a laser to a single mode fibre ring resonator, its relative intensity noise can be reduced. However, the injected laser power into the fibre ring resonator is limited due to the stimulated Brillion effect, which limits the performance of the locked laser. The all-fibred HCF-FP we presented in this thesis may be an ideal replacement to the single mode fibre ring resonators thanks to its weak nonlinear effects.

Appendix A Derivation of Equation (4.6)

An FP's transmission coefficient

$$t(v)=\frac{Te^{-j\frac{\pi v}{FSR}}}{1-Re^{-j\frac{2\pi v}{FSR}}} \tag{10.1}$$

Substituting this to Equation (4.6), we can get

$$\begin{aligned} e_n(f) &= \int t(v)t^*(f-v)dv \\ &= \int_{v_0-BW/2}^{v_0+BW/2} \frac{Te^{-i\frac{\pi v}{FSR}}}{1-Re^{-i\frac{2\pi v}{FSR}}}\cdot\frac{Te^{i\frac{\pi(f-v)}{FSR}}}{1-Re^{i\frac{2\pi(f-v)}{FSR}}}dv \end{aligned} \tag{10.2}$$

BW here is the bandwidth of the used PD. Since FP's transmission coefficient $t(v)$ is a periodic function, we can calculate the integral over one period, namely, FSR. Then the above integral

$$\begin{aligned} e_n(f) &= \int_{v_0}^{v_0+BW} \frac{Te^{-j\frac{\pi v}{FSR}}}{1-Re^{-j\frac{2\pi v}{FSR}}}\cdot\frac{Te^{j\frac{\pi(f-v)}{FSR}}}{1-Re^{j\frac{2\pi(f-v)}{FSR}}}dv \propto \int_0^{FSR} \frac{Te^{-j\frac{\pi v}{FSR}}}{1-Re^{-j\frac{2\pi v}{FSR}}}\cdot\frac{Te^{j\frac{\pi(f-v)}{FSR}}}{1-Re^{j\frac{2\pi(f-v)}{FSR}}}dv \\ &= \int_0^{FSR} \frac{T^2e^{j\frac{\pi(f-2v)}{FSR}}}{1-R\left(e^{-j\frac{2\pi v}{FSR}}+e^{j\frac{2\pi(f-v)}{FSR}}\right)+R^2e^{j\frac{2\pi(f-2v)}{FSR}}}dv \\ &= \int_0^{FSR} \frac{T^2}{e^{-j\frac{\pi(f-2v)}{FSR}}-R\left(e^{-j\frac{\pi f}{FSR}}+e^{j\frac{\pi f}{FSR}}\right)+R^2e^{j\frac{\pi(f-2v)}{FSR}}}dv \\ &= \int_0^{FSR} \frac{T^2}{e^{-j\frac{\pi(f-2v)}{FSR}}-2R\cos\left(\frac{\pi f}{FSR}\right)+R^2e^{j\frac{\pi(f-2v)}{FSR}}}dv \\ &== \int_0^{FSR} \frac{1}{\left(\frac{e^{-j\frac{\pi(f-2v)}{FSR}}-Re^{j\frac{\pi(f-2v)}{FSR}}}{1-R}\right)^2+\frac{4R}{(1-R)^2}\sin^2\left(\frac{\pi f}{2FSR}\right)}dv \\ &= \int_0^{FSR} \frac{1}{\left[\frac{e^{-j\frac{\pi f}{2FSR}}-Re^{j\frac{\pi f}{2FSR}}}{1-R}\right]^2+\frac{4R}{(1-R)^2}\sin^2\left[\frac{\pi(f-2v)}{2FSR}\right]}dv \end{aligned} \tag{10.3}$$

This expression has the same form as the integral

$$\int\frac{1}{a^2+b^2\sin^2(cx)}dx \tag{10.4}$$

which can be found in tables of integrals. Over one period, its result is

$$\frac{\pi}{ac\sqrt{a^2+b^2}} \tag{10.5}$$

Thus, we can get Equation (10.3) as

$$e_n(f) \propto \frac{(1-R)^2 FSR}{e^{-j\frac{\pi f}{FSR}} - R^2 e^{j\frac{\pi f}{FSR}}} \propto \frac{1}{e^{-j\frac{\pi f}{FSR}} - R^2 e^{j\frac{\pi f}{FSR}}} \tag{10.6}$$

Appendix B The RF spectrum of the 23-m all-fibred HCF-FP

I measured the 23-m all fibred HCF-FP almost three later since we made it. The measurement shows that within the three years the 23-m HCF-FP's finesse still keeps the same. Here we show the RF spectra and their fits around the peaks measured at 21st September 2019 and 2nd August 2022 respectively.

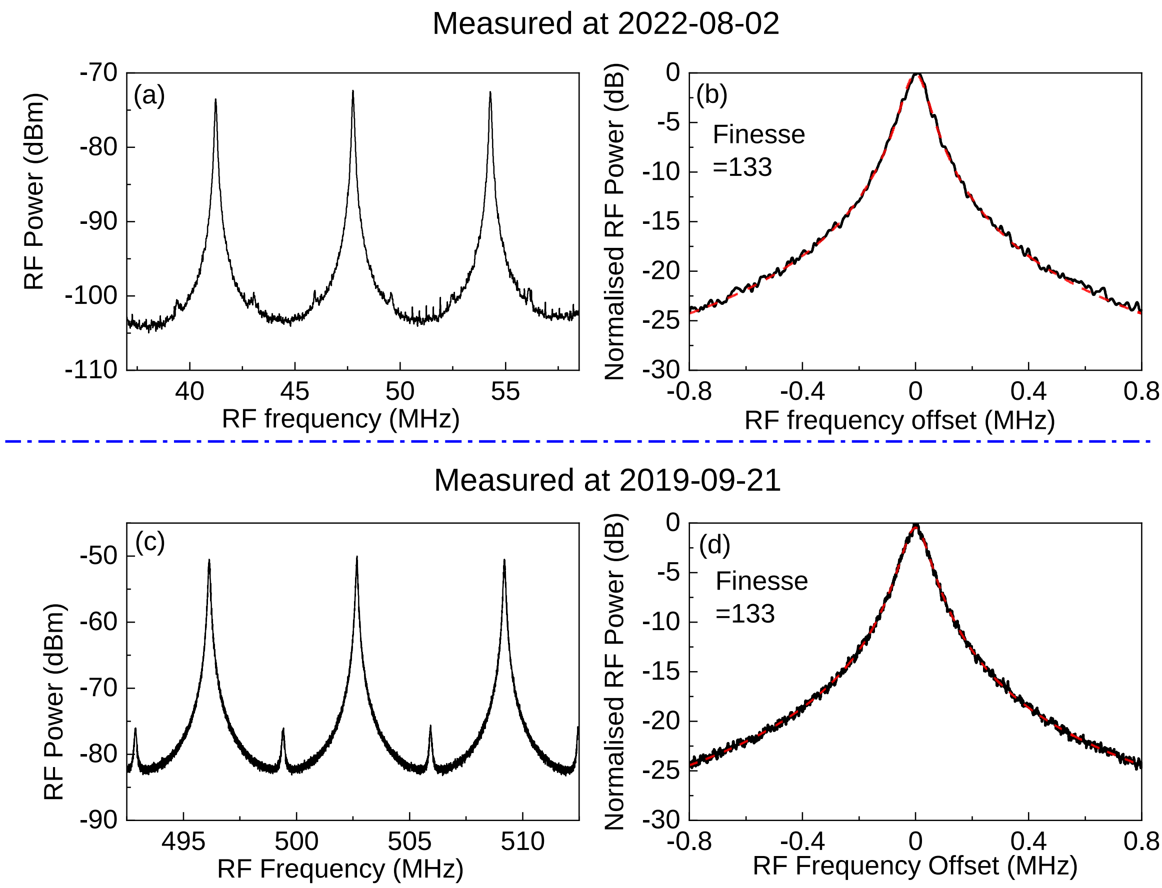

Figure A. 1 RF spectrum of the 23-m all-fibred HCF-FP measured at (a)(b) 2nd Aug 2022 and (c)(d) 21st Sep 2019.

List of References

1. J M VAUGHAN, *The Fabry-Perot Interferometer: History, Theory, Practice and Applications* (Taylor & Francis Group, 1989).

2. A. V. V. Nampoothiri, A. M. Jones, C. Fourcade-Dutin, C. Mao, N. Dadashzadeh, B. Baumgart, Y. Y. Wang, M. Alharbi, T. Bradley, N. Campbell, F. Benabid, B. R. Washburn, K. L. Corwin, and W. Rudolph, "Hollow-core Optical Fiber Gas Lasers (HOFGLAS): a review [Invited]," Opt Mater Express **2**(7), 948 (2012).

3. M. D. Wheeler, S. M. Newman, A. J. Orr-Ewing, and M. N. R. Ashfold, "Cavity ring-down spectroscopy," Journal of the Chemical Society, Faraday Transactions **94**(3), 337–351 (1998).

4. S. Häfner, S. Falke, C. Grebing, S. Vogt, T. Legero, M. Merimaa, C. Lisdat, and U. Sterr, "8 × 10^−17 fractional laser frequency instability with a long room-temperature cavity," Opt Lett **40**(9), 2112 (2015).

5. S. Halverson, S. Mahadevan, L. Ramsey, F. Hearty, J. Wilson, J. Holtzman, S. Redman, G. Nave, D. Nidever, M. Nelson, N. Venditti, D. Bizyaev, and S. Fleming, "Development of Fiber Fabry-Perot Interferometers as Stable Near-infrared Calibration Sources for High Resolution Spectrographs," Publications of the Astronomical Society of the Pacific **126**(939), 445–458 (2014).

6. G. Gagliardi, M. Salza, S. Avino, P. Ferraro, and P. de Natale, "Probing the Ultimate Limit of Fiber-Optic Strain Sensing," Science (1979) **330**(6007), 1081–1084 (2010).

7. N. Md. R. Hoque and L. Duan, "Ultrahigh-Resolution Fiber-Optic Sensing Based on High-Finesse, Meter-Long Fiber Fabry-Perot Resonators," IEEE Photonics J **12**(3), 1–9 (2020).

8. D. Munzke, M. Bohm, and O. Reich, "Gaseous Oxygen Detection Using Hollow-Core Fiber-Based Linear Cavity Ring-Down Spectroscopy," Journal of Lightwave Technology **33**(12), 2524–2529 (2015).

9. Y. Tan, W. Jin, F. Yang, Y. Jiang, and H. L. Ho, "Cavity-Enhanced Photothermal Gas Detection with a Hollow Fiber Fabry-Perot Absorption Cell," Journal of Lightwave Technology **37**(17), 4222–4228 (2019).

10. Y. Tan, W. Jin, F. Yang, Y. Qi, C. Zhang, Y. Lin, and H. L. Ho, "Hollow-Core Fiber-Based High Finesse Resonating Cavity for High Sensitivity Gas Detection," Journal of Lightwave Technology **35**(14), 2887–2893 (2017).

11. O. Volodarsky, Y. Hazan, and A. Rosenthal, "Ultrasound detection via low-noise pulse interferometry using a free-space Fabry-Pérot," Opt Express **26**(17), 22405 (2018).

12. J. Chen, Q. Liu, X. Fan, and Z. He, "Ultrahigh resolution optical fiber strain sensor using dual Pound–Drever–Hall feedback loops," Opt Lett **41**(5), 1066 (2016).

13. M. B. Gray, J. H. Chow, K. McKenzie, and D. E. McClelland, "Using a passive fiber ring cavity to generate shot-noise-limited laser light for low-power quantum optics applications," IEEE Photonics Technology Letters **19**(14), 1063–1065 (2007).

14. R. Slavík, G. Marra, E. N. Fokoua, N. Baddela, N. v. Wheeler, M. Petrovich, F. Poletti, and D. J. Richardson, "Ultralow thermal sensitivity of phase and propagation delay in hollow core optical fibres," Sci Rep **5**, (2015).

15. S. Meiselman and G. A. Cranch, "Optical phase response to temperature in a hollow-core photonic crystal fiber," Opt Express **25**(22), 27581 (2017).

16. F. Yang, F. Gyger, and L. Thévenaz, "Intense Brillouin amplification in gas using hollow-core waveguides," Nat Photonics **14**(11), 700–708 (2020).

17. T. D. Bradley, J. R. Hayes, Y. Chen, G. T. Jasion, S. R. Sandoghchi, R. Slavik, E. N. Fokoua, S. Bawn, H. Sakr, I. A. Davidson, A. Taranta, J. P. Thomas, M. N. Petrovich, D. J. Richardson, and F. Poletti, "Record Low-Loss 1.3dB/km Data Transmitting Antiresonant Hollow Core Fibre," European Conference on Optical Communication, ECOC **2018-September**, (2018).

18. T. D. Bradley, G. T. Jasion, J. R. Hayes, Yong Chen, L. Hooper, H. Sakr, M. Alonso, A. Taranta, A. Saljoghei, H. C. Mulvad, M. Fake, I. A. K. Davidson, N. V. Wheeler, E. N. Fokoua, Wei Wang, S. R. Sandoghchi, D. J. Richardson, and F. Poletti, "Antiresonant Hollow Core Fibre with 0.65 dB/km Attenuation across the C and L Telecommunication Bands," in *45th European Conference on Optical Communication (ECOC 2019)* (Institution of Engineering and Technology, 2019), **2019**(CP765), pp. 294 (4 pp.)-294 (4 pp.).

19. G. T. Jasion, T. D. Bradley, K. Harrington, H. Sakr, Y. Chen, E. N. Fokoua, I. A. Davidson, A. Taranta, J. R. Hayes, D. J. Richardson, and F. Poletti, "Hollow Core NANF with 0.28 dB/km Attenuation in the C and L Bands," Optical Fiber Communication Conference Postdeadline Papers 2020 (2020), paper Th4B.4 Th4B.4 (2020).

20. H. Sakr, T. D. Bradley, G. T. Jasion, E. N. Fokoua, S. R. Sandoghchi, I. A. Davidson, A. Taranta, G. Guerra, W. Shere, Y. Chen, J. R. Hayes, D. J. Richardson, and F. Poletti, "Hollow Core NANFs

with Five Nested Tubes and Record Low Loss at 850, 1060, 1300 and 1625nm," in *Optical Fiber Communication Conference (OFC) 2021* (OSA, 2021), p. F3A.4.

21. Jasion Gregory, Sakr Hesham, Hayes John, Sandoghchi Seyed, Hooper Lucy, Fokoua Eric Rodrigue Numkam, Saljoghei Arsalan, Mulvad Hans Christian, Alonso Marcelo, Taranta Austin, Bradley Thomas, Davidson Ian, Chen Yong, Richardson David, and Poletti Francesco, "0.174 dB/km Hollow Core Double Nested Antiresonant Nodeless Fiber (DNANF)," in *Optical Networking and Communication Conference (OFC)* (2022), p. Th4C.7.

22. H. Sakr, Y. Chen, G. T. Jasion, T. D. Bradley, J. R. Hayes, H. C. H. Mulvad, I. A. Davidson, E. Numkam Fokoua, and F. Poletti, "Hollow core optical fibres with comparable attenuation to silica fibres between 600 and 1100 nm," Nat Commun **11**(1), (2020).

23. F. Poletti, "Nested antiresonant nodeless hollow core fiber," Opt Express **22**(20), 23807 (2014).

24. J. Flannery, R. al Maruf, T. Yoon, and M. Bajcsy, "Fabry-Pérot Cavity Formed with Dielectric Metasurfaces in a Hollow-Core Fiber," ACS Photonics **5**(2), 337–341 (2018).

25. S. Rikimi, Y. Chen, T. Bradley, M. A. Gouveia, R. J. Horley, A. T. Harker, S. Bawn, F. Poletti, M. Petrovich, D. Richardson, and N. Wheeler, "Long-term behaviour of water vapour absorption in hollow core fibres," in *Sixth International Workshop on Specialty Optical Fibers and Their Applications (WSOF 2019)* (2019).

26. A.Yariv and P.Yeh, *Photonics. Optical Electronics in Modern Communications*, 6th ed. (Oxford University, 2007).

27. Scott, "Thermal expansion of Zerodur," https://www.schott.com/en-gb/products/zerodur-p1000269.

28. W. Zhang, L. Stern, D. Carlson, D. Bopp, Z. Newman, S. Kang, J. Kitching, and S. B. Papp, "Ultranarrow Linewidth Photonic-Atomic Laser," Laser Photon Rev **14**(4), (2020).

29. LIGO Caltech, "LIGO’s Interferometer," https://www.ligo.caltech.edu/page/ligos-ifo.

30. Corning, "ULE Corning Code 7972 Ultra Low Expansion Glass," (2016).

31. John Stone and L.W. Stulz, "Pigtailed high-finesse tunable fibre Fabry-Perot interferometers with large, medium and small free spectral ranges," Electron Lett **23**(15), 781–783 (1987).

32. J. Stone and D. Marcuse, "Ultrahigh finesse fiber Fabry-Perot interferometers," Journal of Lightwave Technology **4**(4), 382–385 (1986).

33. John Stone, "Optical-fibre Fabry-Perot interferometer with finesse of 300," Electronic letters **21**(11), 504–505 (1985).

34. Luna, "FFPI Fibre Fabry-Perot Interferometer," .

35. D. Wang, M. Ding, H.-Y. Pi, X. Li, F. Yang, Q. Ye, H.-W. Cai, and F. Wei, "Influence of intra-cavity loss on transmission characteristics of fiber Bragg grating Fabry–Perot cavity," Chinese Physics B **27**(2), 024207 (2018).

36. J. Gallego, S. Ghosh, S. K. Alavi, W. Alt, M. Martinez-Dorantes, D. Meschede, and L. Ratschbacher, "High-finesse fiber Fabry–Perot cavities: stabilization and mode matching analysis," Appl Phys B **122**(3), (2016).

37. Y. Yeh and S. H. Park, "Fiber-optic tunable filter with a concave mirror," Opt Lett **37**(4), 626 (2012).

38. A. Muller, E. B. Flagg, J. R. Lawall, and G. S. Solomon, "Ultrahigh-finesse, low-mode-volume Fabry–Perot microcavity," Opt Lett **35**(13), 2293 (2010).

39. T. Steinmetz, Y. Colombe, D. Hunger, T. W. Hänsch, A. Balocchi, R. J. Warburton, and J. Reichel, "Stable fiber-based Fabry-Pérot cavity," Appl Phys Lett **89**(11), (2006).

40. G. K. Gulati, H. Takahashi, N. Podoliak, P. Horak, and M. Keller, "Fiber cavities with integrated mode matching optics," Sci Rep **7**(1), 5556 (2017).

41. B. Brandstätter, A. McClung, K. Schüppert, B. Casabone, K. Friebe, A. Stute, P. O. Schmidt, C. Deutsch, J. Reichel, R. Blatt, and T. E. Northup, "Integrated fiber-mirror ion trap for strong ion-cavity coupling," in *Review of Scientific Instruments* (2013), **84**(12).

42. H. Takahashi, J. Morphew, F. Oručević, A. Noguchi, E. Kassa, and M. Keller, "Novel laser machining of optical fibers for long cavities with low birefringence," Opt Express **22**(25), 31317 (2014).

43. H. Bao, W. Jin, Y. Hong, H. L. Ho, S. Gao, and Y. Wang, "Phase-Modulation-Amplifying Hollow-Core Fiber Photothermal Interferometry for Ultrasensitive Gas Sensing," Journal of Lightwave Technology **40**(1), 313–322 (2022).

44. B. C. Young, F. C. Cruz, W. M. Itano, and J. C. Bergquist, "Visible Lasers with Subhertz Linewidths," Phys Rev Lett **82**(19), 3799–3802 (1999).

45. T. Kessler, C. Hagemann, C. Grebing, T. Legero, U. Sterr, F. Riehle, M. J. Martin, L. Chen, and J. Ye, "A sub-40-mHz-linewidth laser based on a silicon single-crystal optical cavity," Nat Photonics **6**(10), 687–692 (2012).

46. Painford solutions, "IP Ratings & Standards Explained," https://rainfordsolutions.com/products/ingress-protection-ip-rated-enclosures/ip-enclosure-ratings-standards-explained/#:~:text=The%20IP%20rating%20or%20IP,voltage%20not%20exceeding%2072.5%20kV.&text=This%20standard%20defines%20levels%20of,tools%2C%20dirt%20and%20liquid%20water.

47. U. S. Mutugala, J. Kim, T. D. Bradley, N. v. Wheeler, S. R. Sandoghchi, J. R. Hayes, E. Numkam Fokoua, F. Poletti, M. N. Petrovich, D. J. Richardson, and R. Slavík, "Optoelectronic oscillator incorporating hollow-core photonic bandgap fiber," Opt Lett **42**(13), 2647 (2017).

48. I. Ozdur, M. Akbulut, N. Hoghooghi, D. Mandridis, M. U. Piracha, and P. J. Delfyett, "Optoelectronic loop design with 1000 finesse Fabry-Perot etalon," Opt Lett **35**(6), 799 (2010).

49. J. Mildner, K. Meiners-Hagen, and F. Pollinger, "Dual-frequency comb generation with differing GHz repetition rates by parallel Fabry-Perot cavity filtering of a single broadband frequency comb source," Meas Sci Technol **27**(7), (2016).

50. K. C. Kao and G. A. Hockham, "Dielectric-fibre surface waveguides for optical frequencies," Proceedings of the Institution of Electrical Engineers **113**(7), (1966).

51. F. P. Kapron, D. B. Keck, and R. D. Maurer, "Radiation losses in glass optical waveguides," Appl Phys Lett **17**(10), 423–425 (1970).

52. H. Sakuma, K. Sohma, K. Morita, K. Shimada, M. Suzuki, T. Fujii, T. Hasegawa, Y. Tamura, Y. Yamamoto, and Y. Honma, "The First 0.14-dB/km Loss Optical Fiber and its Impact on Submarine Transmission," Journal of Lightwave Technology, Vol. 36, Issue 1, pp. 44-49 **36**(1), 44–49 (2018).

53. V. Michaud-Belleau, E. Numkam Fokoua, T. D. Bradley, J. R. Hayes, Y. Chen, F. Poletti, D. J. Richardson, J. Genest, and R. Slavík, "Backscattering in antiresonant hollow-core fibers: over 40 dB lower than in standard optical fibers," Optica **8**(2), 216 (2021).

54. Jeff Hecht, "Is Nothing Better Than Something?," https://www.optica-opn.org/home/articles/volume_32/march_2021/features/is_nothing_better_than_something/.

55. D. M. Atkin, J. C. Knight, P. St. J. Russell, and T. A. Birks, "All-silica single-mode optical fiber with photonic crystal cladding," Optics Letters, Vol. 21, Issue 19, pp. 1547-1549 **21**(19), 1547–1549 (1996).

56. R. F. Cregan, B. J. Mangan, J. C. Knight, T. A. Birks, P. St. J. Russell, P. J. Roberts, and D. C. Allan, "Single-Mode Photonic Band Gap Guidance of Light in Air," Science (1979) **285**(5433), 1537–1539 (1999).

57. N. Venkataraman, M.T. Gallagher, C.M. Smith, D. Muller, J.A. West, K.W. Koch, and J.C. Fajardo, "Low Loss (13 dB/km) Air Core Photonic Band-Gap Fibre," in *2002 28TH European Conference on Optical Communication* (2002), p. pdp1.1.

58. A. Langford, B. J. Mangan, D. P. Williams, F. Couny, H. Sabert, J. C. Knight, L. Farr, M. Lawman, M. Mason, P. J. Roberts, P. St. J. Russell, R. Flea, S. Coupland, and T. A. Birks, "Low loss (1.7 dB/km) hollow core photonic bandgap fiber," Optical Fiber Communication Conference (2004), paper PD24 PD24 (2004).

59. P. J. Roberts, F. Couny, H. Sabert, B. J. Mangan, D. P. Williams, L. Farr, M. W. Mason, A. Tomlinson, T. A. Birks, J. C. Knight, and P. st. J. Russell, "Ultimate low loss of hollow-core photonic crystal fibres," Opt Express **13**(1), 236 (2005).

60. F. Poletti, N. G. R. Broderick, D. J. Richardson, and T. M. Monro, "The effect of core asymmetries on the polarization properties of hollow core photonic bandgap fibers," Opt Express **13**(22), 9115 (2005).

61. F. Poletti, N. v. Wheeler, M. N. Petrovich, N. Baddela, E. Numkam Fokoua, J. R. Hayes, D. R. Gray, Z. Li, R. Slavík, and D. J. Richardson, "Towards high-capacity fibre-optic communications at the speed of light in vacuum," Nat Photonics **7**(4), 279–284 (2013).

62. J. L. Archambault, R. J. Black, S. Lacroix, and J. Bures, "Loss Calculations for Antiresonant Waveguides," Journal of Lightwave Technology **11**(3), 416–423 (1993).

63. Y. Y. Wang, N. v. Wheeler, F. Couny, P. J. Roberts, and F. Benabid, "Low loss broadband transmission in hypocycloid-core Kagome hollow-core photonic crystal fiber," Opt Lett **36**(5), 669 (2011).

64. F. Couny, F. Benabid, P. J. Roberts, P. S. Light, and M. G. Raymer, "Generation and photonic guidance of multi-octave optical-frequency combs," Science (1979) **318**(5853), 1118–1121 (2007).

65. J. C. Knight and W. Belardi, "Effect of core boundary curvature on the confinement losses of hollow antiresonant fibers," Optics Express, Vol. 21, Issue 19, pp. 21912-21917 **21**(19), 21912–21917 (2013).

66. J. C. Knight and W. Belardi, "Hollow antiresonant fibers with reduced attenuation," Optics Letters, Vol. 39, Issue 7, pp. 1853-1856 **39**(7), 1853–1856 (2014).

67. B. Debord, A. Amsanpally, M. Chafer, A. Baz, M. Maurel, J. M. Blondy, E. Hugonnot, F. Scol, L. Vincetti, F. Gérôme, and F. Benabid, "Ultralow transmission loss in inhibited-coupling guiding hollow fibers," Optica **4**(2), 209 (2017).

68. S. fei Gao, Y. ying Wang, W. Ding, D. liang Jiang, S. Gu, X. Zhang, and P. Wang, "Hollow-core conjoined-tube negative-curvature fibre with ultralow loss," Nat Commun **9**(1), (2018).

69. A. F. Kosolapov, G. K. Alagashev, A. N. Kolyadin, A. D. Pryamikov, A. S. Biryukov, I. A. Bufetov, and E. M. Dianov, "Hollow-core revolver fibre with a double-capillary reflective cladding," Quantum Elec (Woodbury) **46**(3), 267–270 (2016).

70. F. Poletti, M. N. Petrovich, D. J. Richardson, and M. J. Li, "Hollow-core photonic bandgap fibers: Technology and applications," Nanophotonics **2**(5–6), 315–340 (2013).

71. W. Zheng, Y. Qin, O. Xu, M. Xiang, D. Peng, S. Fu, and J. Li, "Wideband low confinement loss anti-resonant hollow core fiber with nested U-shape tube," Opt Express **29**(15), 24182 (2021).

72. P. J. Roberts, F. Couny, H. Sabert, B. J. Mangan, D. P. Williams, L. Farr, M. W. Mason, A. Tomlinson, T. A. Birks, J. C. Knight, and P. st. J. Russell, "Ultimate low loss of hollow-core photonic crystal fibres," Opt Express **13**(1), 236 (2005).

73. W. Wang, E. N. Fokoua, Y. Chen, and F. Poletti, "Optimizing Single Coated Hollow-core Fibers for Microbending Loss Reduction," OSA Advanced Photonics Congress (AP) 2020 (IPR, NP, NOMA, Networks, PVLED, PSC, SPPCom, SOF) (2020), paper SoW1H.2 **Part F190-SOF 2020**, SoW1H.2 (2020).

74. D. Wu, F. Yu, and M. Liao, "Understanding the material loss of anti-resonant hollow-core fibers," Opt Express **28**(8), 11840 (2020).

75. J. G. Hayashi, S. M. A. Mousavi, A. Ventura, and F. Poletti, "Numerical modeling of a hybrid hollow-core fiber for enhanced mid-infrared guidance," Opt Express **29**(11), 17042 (2021).

76. Allan W. Snyder and John D. Love, "Optical Waveguide Theory," in (1983), pp. 218–219.

77. T. G. Mcrae, S. Ngo, D. A. Shaddock, M. T. L. Hsu, and M. B. Gray, *Frequency Stabilization for Space-Based Missions Using Optical Fiber Interferometry* (2013).

78. F. Kéfélian, H. Jiang, P. Lemonde, and G. Santarelli, *Ultralow-Frequency-Noise Stabilization of a Laser by Locking to an Optical Fiber-Delay Line* (2009).

79. S. Blin, H. K. Kim, M. J. F. Digonnet, and G. S. Kino, "Reduced thermal sensitivity of a fiber-optic gyroscope using an air-core photonic-bandgap fiber," Journal of Lightwave Technology **25**(3), 861–865 (2007).

80. V. Dangui, H. K. Kim, M. J. F. Digonnet, G. S. Kino, Y. Zhao, J. Liu, C. Zhang, and H. Liu, *Phase Sensitivity to Temperature of the Fundamental Mode in Air-Guiding Photonic-Bandgap Fibers* (2005).

81. W. Zhu, M. Ding, M. Zhao, D. J. Richardson, and R. Slaví, *The Thermal Sensitivity of Optical Path Length in Standard Single Mode Fibers down to Cryogenic Temperatures* (2019).

82. R. Slavík, E. R. Numkam Fokoua, M. Bukshtab, Y. Chen, T. D. Bradley, S. R. Sandoghchi, M. N. Petrovich, F. Poletti, and D. J. Richardson, "Demonstration of opposing thermal sensitivities in hollow-core fibers with open and sealed ends," Opt Lett **44**(17), 4367 (2019).

83. W. Zhu, E. R. Numkam Fokoua, Y. Chen, T. Bradley, M. N. Petrovich, F. Poletti, M. Zhao, D. J. Richardson, and R. Slavík, "Temperature insensitive fiber interferometry," Opt Lett **44**(11), 2768 (2019).

84. C. Liu, J. Lin, R. Wu, S. Yu, and T. Jiang, "Stable radio frequency transfer over fiber based on microwave photonic phase shifter," Optics Express, Vol. 27, Issue 26, pp. 38109-38115 **27**(26), 38109–38115 (2019).

85. E. N. Fokoua, M. N. Petrovich, T. Bradley, F. Poletti, D. J. Richardson, and R. Slavík, "How to make the propagation time through an optical fiber fully insensitive to temperature variations," Optica **4**(6), 659 (2017).

86. A. H. Hartog, A. J. Conduit, and D. N. Payne, *Variation of Pulse Delay with Stress and Temperature in Jacketed and Unjacketed Optical Fibres* (1979), **11**.

87. R. Slavik, E. N. Fokoua, M. N. Petrovich, N. v. Wheeler, T. Bradley, F. Poletti, and D. J. Richardson, "Ultralow Thermal Sensitivity of Phase and Propagation Delay in Hollow-Core Fibres," in *2017 European Conference on Optical Communication (ECOC)* (IEEE, 2017), pp. 1–3.

88. W. Zhu, E. R. Numkam Fokoua, A. A. Taranta, Y. Chen, T. Bradley, M. N. Petrovich, F. Poletti, M. Zhao, D. J. Richardson, and R. Slavik, "The Thermal Phase Sensitivity of Both Coated and Uncoated Standard and Hollow Core Fibers down to Cryogenic Temperatures," Journal of Lightwave Technology **38**(8), 2477–2484 (2020).

89. B. Shi, H. Sakr, J. Hayes, X. Wei, E. Numkam Fokoua, M. Ding, Z. Feng, G. Marra, F. Poletti, D. J. Richardson, and R. Slavík, "Thinly coated hollow core fiber for improved thermal phase-stability performance," Opt Lett **46**(20), 5177 (2021).

90. S. Zahedpour, J. K. Wahlstrand, and H. M. Milchberg, "Measurement of the nonlinear refractive index of air constituents at mid-infrared wavelengths," Opt Lett **40**(24), 5794 (2015).

91. S. Wu, B. Siwicki, R. M. Carter, F. Biancalana, J. D. Shephard, and D. P. Hand, "Impact of nonlinear effects on transmission losses of hollow-core antiresonant negative curvature optical fiber," Appl Opt **59**(16), 4988 (2020).

92. A. Iyer, W. Xu, J. E. Antonio-Lopez, R. A. Correa, and W. H. Renninger, "Ultra-low Brillouin scattering in anti-resonant hollow-core fibers," APL Photonics **5**(9), (2020).

93. L. Xiao, W. Jin, M. S. Demokan, H. L. Ho, Y. L. Hoo, and C. Zhao, "Fabrication of selective injection microstructured optical fibers with a conventional fusion splicer," Opt Express **13**(22), 9014 (2005).

94. L. Xiao, M. S. Demokan, W. Jin, Y. Wang, and C. L. Zhao, "Fusion splicing photonic crystal fibers and conventional single-mode fibers: Microhole collapse effect," Journal of Lightwave Technology **25**(11), 3563–3574 (2007).

95. F. Benabid, F. Couny, J. C. Knight, T. A. Birks, and P. S. J. Russell, "Compact, stable and efficient all-fibre gas cells using hollow-core photonic crystal fibres," Nature **434**(7032), 488–491 (2005).

96. R. Thapa, K. Knabe, K. L. Corwin, and B. R. Washburn, "Arc fusion splicing of hollow-core photonic bandgap fibers for gas-filled fiber cells," Opt Express **14**(21), 9576 (2006).

97. D. Suslov, M. Komanec, E. R. Numkam Fokoua, D. Dousek, A. Zhong, S. Zvánovec, T. D. Bradley, F. Poletti, D. J. Richardson, and R. Slavík, "Low loss and high performance interconnection between standard single-mode fiber and antiresonant hollow-core fiber," Sci Rep **11**(1), (2021).

98. K. Z. Aghaie, M. J. F. Digonnet, and S. Fan, "Optimization of the splice loss between photonic-bandgap fibers and conventional single-mode fibers," Opt Lett **35**(12), 1938 (2010).

99. C. Wang, R. Yu, B. Debord, F. Gérôme, F. Benabid, K. S. Chiang, and L. Xiao, "Ultralow-loss fusion splicing between negative curvature hollow-core fibers and conventional SMFs with a reverse-tapering method," Opt Express **29**(14), 22470 (2021).

100. C. Goel, H. Li, M. R. Abu Hassan, W. Chang, and S. Yoo, "Anti-resonant hollow-core fiber fusion spliced to laser gain fiber for high-power beam delivery," Opt Lett **46**(17), 4374 (2021).

101. F. Couny, F. Benabid, and P. S. Light, "Reduction of Fresnel back-reflection at splice interface between hollow core PCF and single-mode fiber," IEEE Photonics Technology Letters **19**(13), 1020–1022 (2007).

102. G. A. Miller and G. A. Cranch, "Reduction of Intensity Noise in Hollow Core Optical Fiber Using Angle-Cleaved Splices," IEEE Photonics Technology Letters **28**(4), 414–417 (2016).

103. Xuefeng Li, J. Pawlat, Jinxing Liang, and Toshitsugu Ueda, "A novel low-loss splice for photonic bandgap fiber gas sensor," in *2008 IEEE Sensors* (IEEE, 2008), pp. 1289–1292.

104. R. Dhawan, Mohd. M. Khan, N. Panwar, U. Tiwari, R. Bhatnagar, and S. C. Jain, "A low loss mechanical splice for gas sensing using Hollow-Core Photonic Crystal Fibre," Optik - International Journal for Light and Electron Optics **124**(18), 3671–3673 (2013).

105. C. Wang, T. D. Bradley, Y. Y. Wang, K. L. Corwin, F. Gerome, and F. Benabid, "Angle splice of large-core kagome hollow-core photonic crystal fiber for gas-filled microcells," in *2013 Conference on Lasers and Electro-Optics, CLEO 2013* (IEEE Computer Society, 2013).

106. J. W. Nicholson, B. Mangan, L. Meng, A. DeSantolo, P. Vannasouk, E. Warych, and T. Taunay, "Low-loss, low return-loss coupling between SMF and single-mode, hollow-core fibers using connectors," in *CLEO: 2014* (OSA, 2014), p. JTu4A.71.

107. M. Komanec, D. Suslov, S. Zvánovec, Y. Chen, T. Bradley, S. R. Sandoghchi, E. R. N. Fokoua, G. T. Jasion, M. N. Petrovich, F. Poletti, D. J. Richardson, and R. Slavík, "Low-Loss and Low-Back-Reflection Hollow-Core to Standard Fiber Interconnection," IEEE Photonics Technology Letters **31**(10), 723–726 (2019).

108. D. Dousek, M. Komanec, A. Zhong, D. Suslov, S. Zvánovec, P. Vesely, Y. Chen, T. D. Bradley, E. R. Numkam Fokoua, F. Poletti, D. J. Richardson, and R. Slavík, "Long-term stability of hollow core to standard optical fiber interconnection," in *Micro-Structured and Specialty Optical Fibres VII*, P. Peterka, K. Kalli, and A. Mendez, eds. (SPIE, 2021), p. 40.

109. H. Kim, Y. Jung, Y. Chen, S. Rikimi, F. Poletti, and D. J. Richardson, "Free Space based Hollow Core Fiber Interconnection and Associated In-Line Components," in *Optical Fiber Communication Conference (OFC) 2019* (OSA, 2019), p. Th3E.3.

110. Yongmin Jung, T. D. Bradley, J. R. Hayes, G. Jasion, I. A. Davidson, H. Sakr, Yong Chen, F. Poletti, and D. J. Richardson, "Multiport micro-optic devices for hollow core fibre applications," in *45th European Conference on Optical Communication (ECOC 2019)* (Institution of Engineering and Technology, 2019), pp. 117 (3 pp.)-117 (3 pp.).

111. Y. Jung, H. Kim, Y. Chen, T. D. Bradley, I. A. Davidson, J. R. Hayes, G. Jasion, H. Sakr, S. Rikimi, F. Poletti, and D. J. Richardson, "Compact micro-optic based components for hollow core fibers," Opt Express **28**(2), 1518 (2020).

112. J. T. Kristensen, A. Houmann, X. Liu, and D. Turchinovich, "Low-loss polarization-maintaining fusion splicing of single-mode fibers and hollow-core photonic crystal fibers, relevant for monolithic fiber laser pulse compression," Opt Express **16**(13), 9986 (2008).

113. Y. Min, A. Filipkowski, G. Stepniewski, D. Dobrakowski, J. Zhou, B. Lou, M. Klimczak, L. Zhao, and R. Buczynski, "Fusion Splicing of Silica Hollow Core Anti-Resonant Fibers With Polarization Maintaining Fibers," Journal of Lightwave Technology **39**(10), 3251–3259 (2021).

114. J. P. Wooler, D. Gray, F. Poletti, M. N. Petrovich, N. v Wheeler, F. Parmigiani, and D. J. Richardson, "Robust Low Loss Splicing of Hollow Core Photonic Bandgap Fiber to Itself," in *Optical Fiber Communication Conference/National Fiber Optic Engineers Conference 2013* (OSA, 2013), p. OM3I.5.

115. O/E Land Inc., "Long-path Gas Cell," .

116. B. Debord, F. Amrani, L. Vincetti, F. Gérôme, and F. Benabid, "Hollow-Core Fiber Technology: The Rising of “Gas Photonics,”" Fibers **7**(2), 16 (2019).

117. F. Benabid, J. C. Knight, G. Antonopoulos, and P. St. J. Russell, "Stimulated Raman Scattering in Hydrogen-Filled Hollow-Core Photonic Crystal Fiber," Science (1979) **298**(5592), 399–402 (2002).

118. F. Belli, A. Abdolvand, W. Chang, J. C. Travers, and P. St. J. Russell, "Vacuum-ultraviolet to infrared supercontinuum in hydrogen-filled photonic crystal fiber," Optica **2**(4), 292 (2015).

119. S. Ghosh, J. E. Sharping, D. G. Ouzounov, and A. L. Gaeta, "Resonant Optical Interactions with Molecules Confined in Photonic Band-Gap Fibers," Phys Rev Lett **94**(9), 093902 (2005).

120. A. v. Gladyshev, A. F. Kosolapov, M. M. Khudyakov, Y. P. Yatsenko, A. N. Kolyadin, A. A. Krylov, A. D. Pryamikov, A. S. Biriukov, M. E. Likhachev, I. A. Bufetov, and E. M. Dianov, "2.9, 3.3, and 3.5 μm Raman Lasers Based on Revolver Hollow-Core Silica Fiber Filled by 1H2/D2 Gas Mixture," IEEE Journal of Selected Topics in Quantum Electronics **24**(3), (2018).

121. S. D. Jackson and R. K. Jain, "Fiber-based sources of coherent MIR radiation: key advances and future prospects (invited)," Opt Express **28**(21), 30964 (2020).

122. Y. Cui, W. Huang, Z. Wang, M. Wang, Z. Zhou, Z. Li, S. Gao, Y. Wang, and P. Wang, "4.3 μm fiber laser in CO2 -filled hollow-core silica fibers," Optica **6**(8), 951 (2019).

123. J. E. McCord, A. A. Ionin, S. P. Phipps, P. G. Crowell, A. I. Lampson, J. K. McIver, A. J. W. Brown, and G. D. Hager, "Frequency-tunable optically pumped carbon monoxide laser," IEEE J Quantum Electron **36**(9), 1041–1052 (2000).

124. C. S. Kletecka, N. Campbell, C. R. Jones, J. W. Nicholson, and W. Rudolph, "Cascade lasing of molecular HBr in the four micron region pumped by a Nd:YAG laser," IEEE J Quantum Electron **40**(10), 1471–1477 (2004).

125. B. Wellegehausen, "Optically pumped CW dimer lasers," IEEE J Quantum Electron **15**(10), 1108–1130 (1979).

126. J. B. Koffend and R. W. Field, "CW optically pumped molecular iodine laser," J Appl Phys **48**(11), 4468–4472 (1977).

127. R. L. Byer, R. L. Herbst, H. Kildal, and M. D. Levenson, "Optically Pumped Molecular Iodine Vapor-Phase Laser," Appl Phys Lett **20**(11), 463–466 (1972).

128. J. C. Travers, W. Chang, J. Nold, N. Y. Joly, and P. st. J. Russell, "Ultrafast nonlinear optics in gas-filled hollow-core photonic crystal fibers [Invited]," Journal of the Optical Society of America B **28**(12), A11 (2011).

129. M. Nikodem, G. Gomółka, M. Klimczak, D. Pysz, and R. Buczyński, "Laser absorption spectroscopy at 2 μm inside revolver-type anti-resonant hollow core fiber," Opt Express **27**(10), 14998 (2019).

130. C. Yao, S. Gao, Y. Wang, P. Wang, W. Jin, and W. Ren, "Silica Hollow-Core Negative Curvature Fibers Enable Ultrasensitive Mid-Infrared Absorption Spectroscopy," Journal of Lightwave Technology **38**(7), 2067–2072 (2020).

131. W. Jin, Y. Cao, F. Yang, and H. L. Ho, "Ultra-sensitive all-fibre photothermal spectroscopy with large dynamic range," Nat Commun **6**, (2015).

132. P. Zhao, Y. Zhao, H. Bao, H. L. Ho, W. Jin, S. Fan, S. Gao, Y. Wang, and P. Wang, "Mode-phase-difference photothermal spectroscopy for gas detection with an anti-resonant hollow-core optical fiber," Nat Commun **11**(1), (2020).

133. T. Billotte, M. Chafer, M. Maurel, F. Amrani, F. Gerome, B. Debord, and F. Benabid, "Contaminant-free end-capped and single-mode acetylene photonic microcell for sub-Doppler spectroscopy," Opt Lett **46**(3), 456 (2021).

134. J. A. Nwaboh, J. Hald, J. K. Lyngsø, J. C. Petersen, and O. Werhahn, "Measurements of CO2 in a multipass cell and in a hollow-core photonic bandgap fiber at 2 µm," Applied Physics B **110**(2), 187–194 (2013).

135. A. M. Cubillas, M. Silva-Lopez, J. M. Lazaro, O. M. Conde, M. N. Petrovich, and J. M. Lopez-Higuera, "Methane detection at 1670-nm band using a hollow-core photonic bandgap fiber and a multiline algorithm," Opt Express **15**(26), 17570 (2007).

136. Y. L. Hoo, S. Liu, H. L. Ho, and W. Jin, "Fast response microstructured optical fiber methane sensor with multiple side-openings," IEEE Photonics Technology Letters **22**(5), 296–298 (2010).

137. P. Kozioł, P. Jaworski, K. Krzempek, V. Hoppe, G. Dudzik, F. Yu, D. Wu, M. Liao, J. Knight, and K. Abramski, "Fabrication of microchannels in a nodeless antiresonant hollow-core fiber using femtosecond laser pulses," Sensors **21**(22), (2021).

138. H. Bao, W. Jin, Y. Hong, H. L. Ho, S. Gao, and Y. Wang, "Phase-modulation-amplifying hollow-core fiber photothermal interferometry for ultrasensitive gas sensing," Journal of Lightwave Technology 1–1 (2021).

139. E. A. Curtis, N. C. G. Black, G. P. Barwood, and P. Gill, "Gas-filled Kagome hollow-core fiber cell for compact laser frequency stabilization systems," in *Conference on Lasers and Electro-Optics* (OSA, 2021), p. AW4M.6.

140. E. A. Curtis, T. Bradley, G. P. Barwood, C. S. Edwards, N. v. Wheeler, R. Phelan, D. J. Richardson, M. N. Petrovich, and P. Gill, " Laser frequency stabilization and spectroscopy at

2051 nm using a compact CO 2 -filled Kagome hollow core fiber gas-cell system ," Opt Express **26**(22), 28621 (2018).

141. T. W. Kelly, P. Horak, I. A. Davidson, M. Partridge, G. T. Jasion, S. Rikimi, A. Taranta, D. J. Richardson, F. Poletti, and N. v. Wheeler, "Gas-induced differential refractive index enhanced guidance in hollow-core optical fibers," Optica **8**(6), 916 (2021).

142. Y. J. Rao, M. Deng, T. Zhu, and H. Li, "In-line Fabry-Perot etalons based on hollow-corephotonic bandgap fibers for high-temperature applications," Journal of Lightwave Technology **27**(19), 4360–4365 (2009).

143. Q. Shi, F. Lv, Z. Wang, L. Jin, J. J. Hu, Z. Liu, G. Kai, and X. Dong, "Environmentally Stable Fabry-Perot-Type Strain Sensor Based On Hollow-Core Photonic Bandgap Fiber," IEEE Photonics Technology Letters **20**(4), 237–239 (2008).

144. H. Yu, Z. Luo, Y. Zheng, J. Ma, Z. Li, and X. Jiang, "Temperature-Insensitive Vibration Sensor with Kagomé Hollow-Core Fiber Based Fabry-Perot Interferometer," Journal of Lightwave Technology **37**(10), 2261–2269 (2019).

145. D. Liu, W. Li, Q. Wu, F. Ling, K. Tian, C. Shen, F. Wei, G. Farrell, Y. Semenova, and P. Wang, "Strain-, curvature- and twist-independent temperature sensor based on a small air core hollow core fiber structure," Opt Express **29**(17), 26353 (2021).

146. L. Jin, B. O. Guan, and H. Wei, "Sensitivity characteristics of fabry-perot pressure sensors based on hollow-core microstructured fibers," Journal of Lightwave Technology **31**(15), 2526–2532 (2013).

147. M. Pang and W. Jin, "Detection of acoustic pressure with hollow-core photonic bandgap fiber," Opt Express **17**(13), 11088 (2009).

148. Z. Zhang, J. He, B. Du, F. Zhang, K. Guo, and Y. Wang, "Measurement of high pressure and high temperature using a dual-cavity Fabry–Perot interferometer created in cascade hollow-core fibers," Opt Lett **43**(24), 6009 (2018).

149. Y. Yu, X. Chen, Q. Huang, C. Du, S. Ruan, and H. Wei, "Enhancing the pressure sensitivity of a Fabry–Perot interferometer using a simplified hollow-core photonic crystal fiber with a microchannel," Appl Phys B **120**(3), 461–467 (2015).

150. P. Roldán-Varona, R. A. Pérez-Herrera, L. Rodríguez-Cobo, L. Reyes-González, M. López-Amo, and J. M. López-Higuera, "Liquid level sensor based on dynamic Fabry–Perot interferometers in processed capillary fiber," Sci Rep **11**(1), 3039 (2021).

151. Y. Wang, D. N. Wang, C. R. Liao, T. Hu, J. Guo, and H. Wei, "Temperature-insensitive refractive index sensing by use of micro Fabry–Pérot cavity based on simplified hollow-core photonic crystal fiber," Opt Lett **38**(3), 269 (2013).

152. X. Zhang and W. Peng, "Temperature-independent fiber salinity sensor based on Fabry-Perot interference," Opt Express **23**(8), 10353 (2015).

153. Y. Zhang, Y. Li, T. Wei, X. Lan, Y. Huang, G. Chen, and H. Xiao, "Fringe visibility enhanced extrinsic Fabry-Perot interferometer using a graded index fiber collimator," IEEE Photonics J **2**(3), 469–481 (2010).

154. G. A. Sanders, A. A. Taranta, C. Narayanan, E. Numkam Fokoua, S. Abokhamis Mousavi, L. K. Strandjord, M. Smiciklas, T. D. Bradley, J. Hayes, G. T. Jasion, T. Qiu, W. Williams, F. Poletti, and D. N. Payne, "Hollow-core resonator fiber optic gyroscope using nodeless anti-resonant fiber," Opt Lett **46**(1), 46 (2021).

155. X. Zhao, J. Louveau, J. Chamoun, and M. J. F. Digonnet, "Thermal sensitivity of the birefringence of air-core fibers and implications for the RFOG," Journal of Lightwave Technology **32**(14), 2577–2581 (2014).

156. S. Blin, H. K. Kim, M. J. F. Digonnet, and G. S. Kino, "Reduced thermal sensitivity of a fiber-optic gyroscope using an air-core photonic-bandgap fiber," Journal of Lightwave Technology **25**(3), 861–865 (2007).

157. R.-Y. Liu, C.-A. Chiou, and T.-S. Peng, "An accelerated gamma irradiation test of low dose rate for a single mode fiber," in *International Conference on Space Optics — ICSO 2016*, N. Karafolas, B. Cugny, and Z. Sodnik, eds. (SPIE, 2017), p. 194.

158. L. Olanterä, C. Sigaud, J. Troska, F. Vasey, M. N. Petrovich, F. Poletti, N. v Wheeler, J. P. Wooler, and D. J. Richardson, "Gamma irradiation of minimal latency Hollow-Core Photonic Bandgap Fibres," Journal of Instrumentation **8**(12), C12010–C12010 (2013).

159. S. Wang, W. Chen, J.-F. Guo, Z.-Q. Yin, H.-W. Li, Z. Zhou, G.-C. Guo, and Z.-F. Han, "2 GHz clock quantum key distribution over 260 km of standard telecom fiber," Opt Lett **37**(6), 1008 (2012).

160. L. Gavrilovska, V. Rakovic, and V. Atanasovski, "Visions Towards 5G: Technical Requirements and Potential Enablers," Wirel Pers Commun **87**(3), 731–757 (2016).

161. M. Burla, C. G. H. Roeloffzen, L. Zhuang, D. Marpaung, M. R. Khan, P. Maat, K. Dijkstra, A. Leinse, M. Hoekman, and R. Heideman, "System integration and radiation pattern

measurements of a phased array antenna employing an integrated photonic beamformer for radio astronomy applications," Appl Opt **51**(7), 789 (2012).

162. D. Kwon and J. Kim, "All-fiber interferometer-based repetition-rate stabilization of mode-locked lasers to 10^−14-level frequency instability and 1-fs-level jitter over 1 s," Opt Lett **42**(24), 5186 (2017).

163. J. J. Liu, X. P. Ma, G. X. Pei, N. Gan, and J. sen Yang, "Phase-stabilized RF transmission system based on LLRF controller and optical delay line," Nuclear Science and Techniques **30**(12), (2019).

164. M. Bousonville, M. K. Bock, M. Felber, T. Ladwig, T. Lamb, H. Schlarb, S. Schulz, C. Sydlo, S. Hunziker, P. Kownacki, and S. Jablonski, "NEW PHASE STABLE OPTICAL FIBER," in *Proc. Beam Instrum. Workshop* (2012), pp. 101–103.

165. U. S. Mutugala, E. R. Numkam Fokoua, Y. Chen, T. Bradley, S. R. Sandoghchi, G. T. Jasion, R. Curtis, M. N. Petrovich, F. Poletti, D. J. Richardson, and R. Slavík, "Hollow-core fibres for temperature-insensitive fibre optics and its demonstration in an Optoelectronic oscillator," Sci Rep **8**(1), (2018).

166. M. Ding, E. R. N. Fokoua, T. D. Bradley, F. Poletti, D. J. Richardson, and R. Slavik, "Finesse Limits in Hollow Core Fiber based Fabry-Perot interferometers," Journal of Lightwave Technology **39**(13), 4489–4495 (2021).

167. C. Rohrer, J. H. Osorio, F. Beirow, M. Maurel, B. Debord, T. Graf, F. Gerome, F. Benabid, and M. A. Ahmed, "Phase Shift Induced Degradation of Polarization Caused by Bends in Inhibited-Coupling Guiding Hollow-Core Fibers," IEEE Photonics Technology Letters **31**(16), 1362–1365 (2019).

168. A. Taranta, E. Numkam Fokoua, S. Abokhamis Mousavi, J. R. Hayes, T. D. Bradley, G. T. Jasion, and F. Poletti, "Exceptional polarization purity in antiresonant hollow-core optical fibres," Nat Photonics **14**(8), 504–510 (2020).

169. M. Ding, M. Komanec, D. Suslov, D. Dousek, S. Zvanovec, E. R. N. Fokoua, T. D. Bradley, F. Poletti, D. J. Richardson, and R. Slavik, "Long-Length and Thermally Stable High-Finesse Fabry-Perot Interferometers Made of Hollow Core Optical Fiber," Journal of Lightwave Technology **38**(8), 2423–2427 (2020).

170. C.-L. Chen, "Optical fiber Fabry-Perot cavities and recirculating delay lines as tunable microwave filters," IEEE Trans Microw Theory Tech **38**(5), 647–653 (1990).

171. H. Gao, J. Wang, J. Shen, S. Zhang, D. Xu, Y. Zhang, and C. Li, "Study of the Vernier Effect Based on the Fabry–Perot Interferometer: Methodology and Application," Photonics **8**(8), 304 (2021).

172. M. Ding, Z. Feng, D. Marpaung, X. Zhang, M. Komanec, D. Suslov, D. Dousek, S. Zvanovec, E. R. N. Fokoua, T. D. Bradley, F. Poletti, D. J. Richardson, and R. Slavik, "Optical Fiber Delay Lines in Microwave Photonics: Sensitivity to Temperature and Means to Reduce it," Journal of Lightwave Technology **39**(8), 2311–2318 (2021).

173. C. Li, W. Yang, M. Wang, X. Yu, J. Fan, Y. Xiong, Y. Yang, and L. Li, "A Review of Coating Materials Used to Improve the Performance of Optical Fiber Sensors," Sensors **20**(15), 4215 (2020).

174. M. Ding, E. N. Fokoua, J. R. Hayes, H. Sakr, P. Horak, F. Poletti, D. J. Richardson, and R. Slavík, "Hollow-core fiber Fabry–Perot interferometers with reduced sensitivity to temperature," Opt Lett **47**(10), 2510 (2022).

List of Publications

Journal Papers

1. M. Ding, E. N. Fokoua, J. Hayes, H. Sakr, P. Horak, F. Poletti, D. Richardson and R. Slavík, “Hollow core fibre Fabry-Perot interferometers with reduced sensitivity to temperature,” Optics Letters, vol. 47, no. 10, pp. 2510–2513, 2022.
2. M. Ding, E. N. Fokoua, T. D. Bradley, F. Poletti, D. Richardson and R. Slavík, “Finesse Limits in Hollow Core Fibre based Fabry-Perot interferometers,” Journal of Lightwave Technology, vol. 39, no. 13, pp. 4489–4495, 2021.
3. M. Ding, Z. Feng, D. Marpuang, X. Zhang, M. Komanec, D. Suslov, D. Dousek, S. Zvanovec, E.N. Fokoua, T.D. Bradley, F. Poletti, D. Richardson and R. Slavík, “Optical Fibre Delay Lines in Microwave Photonics: Sensitivity to Temperature and Means to Reduce it,” Journal of Lightwave Technology, vol. 39, no. 8, pp. 2311–2318, 2021.
4. M. Ding, M. Komanec, D. Suslov, D. Dousek, S. Zvanovec, E. N. Fokoua, T.D. Bradley, F. Poletti, D. Richardson and R. Slavík, “Long-Length and Thermally Stable High-Finesse Fabry-Perot Interferometers Made of Hollow Core Optical Fibre,” Journal of Lightwave Technology, vol. 38, no. 8, pp. 2423–2427, 2020.
5. E.N. Fokoua, W. Zhu, M. Ding, Z. Feng, Y. Chen, T. D. Bradley, G. Jasion, D. Richardson, F. Poletti and R. Slavík, “Polarization Effects on Thermally Stable Latency in Hollow-Core Photonic Bandgap Fibres,” Journal of Lightwave Technology, vol. 39, no. 7, pp. 2142 - 2150, 2021.
6. U. S. Mutugala, I. P. Giles, M. Ding, D. J. Richardson, and R. Slavík, “All-fibre passive alignment free depolarizers capable of depolarizing narrow linewidth signals,” Journal of Lightwave Technology, vol. 37, no. 3, pp. 704–714, 2018.
7. O. Green, X. Zhang, E. N. Fokoua, M. Ding, Z. Feng, Y. Chen, A. Taranta, F. Poletti, D. Richardson and R. Slavík, “In-line polarization controller for hollow core photonic bandgap fibre,” Optics Communications, vol. 481, p.126552, 2021.
8. B. Shi, H. Sakr, J. Hayes, X. Wei, E. N. Fokoua, M. Ding, Z. Feng, G. Marra, F. Poletti, D.J. Richardson and R. Slavík,” Thinly-coated hollow core fibre for improved thermal phase-stability performance,” Optics Letters, vol. 46, no. 20, pp. 5177-5180, 2021.
9. W. Zhu, E. N. Fokoua, Y. Chen, T. D. Bradley, S. R. Sandoghchi, M. Ding, G. T. Jasion, M. N. Petrovich, F. Poletti, M. Zhao, D. J. Richardson and R. Slavík, “Toward High Accuracy Positioning in 5G via Passive Synchronization of Base Stations Using Thermally-Insensitive Optical Fibres,” IEEE Access, vol. 7, pp. 113197-113205, 2019.

Conference Proceedings

1. M. Ding, E. N. Fokoua, T. D. Bradley, H. Sakr, P. Horak, F. Poletti, D. Richardson and R. Slavík, "Hollow core fibre temperature sensitivity reduction via winding on a thermally-insensitive coil," in Conference on Lasers and Electro-Optics 2021 (CLEO 2021), in San Jose, California United States, 9–14 May 2021, pp. STu1Q.7.
2. M. Ding, E. N. Fokoua, T. D. Bradley, H. Sakr, P. Horak, F. Poletti, D. Richardson and R. Slavík, "Hollow core fibre Fabry-Perot interferometers with finesse over 3000," in Conference on Lasers and Electro-Optics 2020 (CLEO 2020), in San Jose, California United States, 10–15 May 2020, pp. SF2P.2.
3. M. Ding, D.J. Richardson and R. Slavík, "Long Length Fibre Fabry-Perot Interferometers and their Applications in Fibre Characterization and Temperature Sensing," in Conference on Lasers and Electro-Optics Europe & European Quantum Electronics Conference 2019 (CLEO/Europe-EQEC 2019), in Munich, Germany, 23-27 June 2019.
4. M. Ding, E. N. Fokoua, Y. Chen, T. D. Bradley, S. R. Sandoghchi, G. Jasion, M. N. Petrovich, F. Poletti, D. J. Richardson and R. Slavík, "Fabrication and characterization of a hollow-core fibre based high finesse Fabry-Perot etalon," in Asia Communications and Photonics Conference 2019 (ACP 2019), in Hangzhou, China, 26-29 October 2018.
5. W. Zhu, M. Ding, M. Zhao, D. J. Richardson and R. Slavík, "The thermal sensitivity of optical path length in standard single mode fibres down to cryogenic temperatures," in Conference on Lasers and Electro-Optics 2019 (CLEO 2019), in San Jose, California United States, 5–10 May 2019, pp. SM2L.6.
6. R. Slavík, J. Vojtech, M. Ding and D. J. Richardson, "Compact and low-power comb-locked transmitter based on ITLA tuneable lasers", in 45th European Conference on Optical Communication (ECOC 2019), in Dublin, Ireland, 22-26 September 2019.
7. R. Slavík, E. N. Fokoua, M. Ding, Y. Chen, M. N. Petrovich, T. D. Bradley, F. Poletti and D. J. Richardson, "Compact and low-power comb-locked transmitter based on ITLA tuneable lasers," in 45th European Conference on Optical Communication (ECOC 2019), in Dublin, Ireland, 22-26 September 2019.
8. R. Slavík, E. N. Fokoua, M. Ding, Z. Feng, F. Poletti and D. J. Richardson, "Unusual properties of hollow-core fibres," in Micro-structured and Specialty Optical Fibres VII, in 18 April 2021, 117730D.
9. E. N. Fokoua, W. Zhu, Y. Chen, M. Ding, F. Poletti and D. J. Richardson, and R. Slavík, "Thermally insensitive optical fibres and their applications," in Asia Communications and Photonics Conference 2019 (ACP 2019), in Chengdu, China, 2-5 November 2019.